Development of All-Sky Imager quality control methods and their evaluation in Eye2Sky nowcasting

Master thesis

Author:
Arne Goerlitz

A thesis presented for the degree of
Master of Science (M.Sc.)

School V - School of mathematics and sciences
Institute for Chemistry and Biology of the Marine Environment
Environmental Modelling

Carl von Ossietzky University of Oldenburg
Carl-von-Ossietzky-Straße 9-11
P. O. Box 5634
D-26046 Oldenburg
4th August 2025

Development of All-Sky Imager quality control methods and their evaluation in Eye2Sky nowcasting

Author: Arne Goerlitz[1,3]

4th August 2025

Supervisors: Prof. Dr. Carsten Agert[2,3]
M.Sc. Jonas Stührenberg[3]

Institute of Networked Energy Systems

[1]Carl von Ossietzky University of Oldenburg (UOL) - School V - Institute for Chemistry and Biology of the Marine Environment (ICBM)
[2]Carl von Ossietzky University of Oldenburg (UOL) - School V - Institute of Physics
[3]German Aerospace Center (DLR) - Institute of Networked Energy Systems (VE)

Copyright

Oldenburg (Oldb), 4th August 2025 .....

Abstract

Accurate prediction of the energy production of photovoltaic systems requires precise weather forecasts of solar irradiance. Numerical weather prediction models and satellite-based forecast methods provide solar irradiance forecasts only with limited temporal and spatial resolution. All-sky imager systems can provide solar irradiance forecasts with high resolutions in the order of metres and minutes. The focus of this work is on the all-sky imager network Eye2Sky, a camera network located in the north-west of Germany, whose topology is unique due to its size and camera density.

This work addresses the question of how errors of all-sky imagers, e.g. soiling or interfering objects, do affect the interim and final results of the solar irradiance forecast. The physics-based forecast algorithm WobaS was the focus of this analysis. More precisely, the effect of errors on the cloud masking process, on the cloud base height estimation, as well as on the resulting irradiance maps of WobaS were analysed. Based on the findings of this analysis, methods for the detection and prevention of errors have been developed and validated. Finally, recommendations are given for the operation of all-sky imager networks with regard to quality control.
Key words: all-sky imager, quality control, solar irradiance, photovoltaic

Zusammenfassung

Für die korrekte Vorhersage der Energieproduktion von Photovoltaikanlagen sind präzise Wettervorhersagen der solaren Einstrahlung essenziell. Nummerische Wettervorhersagen oder satelliten-gestützte Solarleistungsprognosen liefern Ergebnisse nur in begrenzter räumlicher und zeitlicher Auflösung. Wolkenkamerasysteme können Vorhersagen der solaren Einstrahlung mit einer Auflösung in der Größenordnung von Metern und Minuten bereitstellen. Im Fokus dieser Arbeit steht das Wolkenkameranetzwerk Eye2Sky im Nordwesten von Deutschland, das aufgrund seiner Größe und Dichte an Kameras eine in dieser Form einzigartige Topologie besitzt.

In dieser Arbeit wurde die Frage adressiert, wie sich Fehler von Wolkenkameras, wie beispielsweise Verschmutzung der Linsen oder Störobjekte, auf die Zwischen- und Endergebnisse der Solarstrahlungsvorhersage auswirken können. Analysiert wurden die Ergebnisse des physikbasierten Vorhersagealgorithmus WobaS. Genauer wird der Einfluss der Fehler auf die Ergebnisse der Wolkenmaskierung, auf die Wolkenhöhenbestimmung sowie auf die resultierenden Strahlungskarten untersucht. Basierend auf den Ergebnissen dieser Analyse werden Methoden entwickelt und validiert, die der automatisierten Erkennung und Verhinderung dieser Fehler dienen. Abschließend werden Empfehlungen zur Qualitätskontrolle von Wolkenkameranetzwerken gegeben.
Schlüsselwörter: Wolkenkameras, Qualitätskontrolle, Solare Einstrahlung, Photovoltaik

Acknowledgement

I would like to express my sincere gratitude to my first examiner, Prof. Dr. Agert, for giving me the opportunity to write this thesis at German Aerospace Center (DLR) - Institute of Networked Energy Systems (VE).

Furthermore, I especially would like to thank my second examiner and supervisor, Jonas Stührenberg, for his time and continuous support and encouragement during this thesis, as well as for our constructive and fruitful discussions.

I am also grateful to my team leader, Dr. Marion Schroedter-Homscheidt, for her great support and helpful feedback, and I also thank my department leader, Dr. Thomas Vogt, for the warm welcoming and the good working atmosphere at our site. My thanks also go to all the members of the Energy Meteorology group, especially to my Eye2Sky co-workers, Dr. Thomas Schmidt, André Scheper and Dr. Annette Hammer, for all their efforts and support in answering my numerous questions.

Finally, I would like to express my gratitude to my girlfriend, my friends, and my family for their constant emotional support.

Contents

List of Figures

List of Tables

Acronyms

AI attenuation index.

ASI all-sky imager.

BNI beam (direct) normal irradiance.

CBH cloud base height.

CMV cloud motion vector.

CNN convolutional neural network.

CV computer vision.

DHI diffuse horizontal irradiance.

DLR German Aerospace Center.

FOV field of view.

FTP file transfer protocol.

GHI global horizontal irradiance.

ICBM Institute for Chemistry and Biology of the Marine Environment.

MAE mean absolute error.

MBE mean bias error.

ML machine learning.

MTG Meteosat Third Generation.

NWP numerical weather prediction.

POV point of view.

PV photovoltaic.

QC quality control.

RGB red-green-blue additive colour model.

RMSE root mean square error.

rRMSE relative root mean square error.

RSI rotating shadowband irradiometer.

SF Institute of Solar Research.

UOL Carl von Ossietzky University of Oldenburg.

VE Institute of Networked Energy Systems.

VHS ventilation-heating-system.

List of Symbols

Symbol	Description	Unit
AI	attenuation index	[-]
BNI	beam (direct) normal irradiance	$\mathrm{W\,m^{-2}}$
CBH	cloud base height	m
$\hat{CBH}$	cloud base height observations	m
$\vec{CMV}$	cloud motion vector	$[\mathrm{m\,s^{-1}}]_{2\times1}$
DHI	diffuse horizontal irradiance	$\mathrm{W\,m^{-2}}$
GHI	global horizontal irradiance	$\mathrm{W\,m^{-2}}$
$IRRAD$	irradiance component	$\mathrm{W\,m^{-2}}$
$IRRAD_{obs}$	irradiance component observations	$\mathrm{W\,m^{-2}}$
lat	latitude dimension	°
lon	longitude dimension	°
lt	lead time dimension	min
MAE_{CBH}	mean absolute error of cloud base height (CBH)	m
MAE_{IRRAD}	mean absolute error of irradiance component	$\mathrm{W\,m^{-2}}$
MBE_{CBH}	mean bias error of cloud base height (CBH)	m
MBE_{IRRAD}	mean bias error of irradiance component	$\mathrm{W\,m^{-2}}$
N	number of images	[-]
n	number of cloud base height data points	[-]
n_c	number of valid segmentation classes	[-]
n_p	number of data points in map	[-]
n_{pix}	number of pixels in image	[-]
n_t	number of data points in time series	[-]
p	point in geo-referenced map (lat,lon)	[°,°]
$RMSE_{CBH}$	root mean square error of cloud base height (CBH)	m
$RMSE_{IRRAD}$	root mean square error of irradiance component	$\mathrm{W\,m^{-2}}$
$rRMSE_{CBH}$	relative root mean square error of cloud base height (CBH)	[-]
SV	soiling value	[-]
t	time dimension	UTC
ts	time stamp in time series	UTC

Symbol	Description	Unit
u	number of classified pixels	[-]
v	pixel grey value	[-]
α	azimut angle	rad
ϵ	elevation angle	rad
θ	zenith angle	rad
μ	mean pixel grey value	[-]
σ	standard deviation of pixel grey value	[-]

Glossary

BirdDB Tool for automatic creation of database for interfering objects in the Eye2Sky network.

Eye2Sky Network of all-sky imagers (ASIs) and meteorological stations in the north-west of Germany operated by German Aerospace Center (DLR) - Institute of Networked Energy Systems (VE).

NetCDF (Network Common Data Form) Collection of software libraries and data formates for scientific array-oriented data [33].

OpenCV Non-profit open source programming library for computer vision (CV) [3].

WobaS Algorithm for short-term irradiance forecast from all-sky imager (ASI) and meteorological data developed by German Aerospace Center (DLR) - Institute of Solar Research (SF).

1 Introduction

Combating human-made climate change and its consequences is one of the greatest challenges of our time. By signing the Paris Climate Agreement [18] and with the passing of the European Green Deal [8] and the Federal Climate Protection Act [5], Germany aims to become climate-neutral by 2045. This goal has also been confirmed in the coalition agreement of the new federal government [6].

According to the latest federal climate report [4], the energy industry is the dominant sector in terms of greenhouse gas emissions in Germany. Therefore, the decarbonisation of the energy grid is an inevitable step towards reaching climate neutrality. However, the introduction of additional renewable energy plants poses challenges to the stability and resilience of the energy grid [31] and to the dynamics of the energy markets [34]. The production and distribution of electricity are increasingly dependent on the current weather situation, which is why reliable weather forecasts are becoming more important. These forecasts can help not only to predict energy production or heating and cooling demands but also to prevent energy shortages or bottleneck situations, as well as to optimise energy storages. Better predictions can help minimise potential balancing costs, thereby lowering energy prices.

For the prediction of the expected solar energy, a spatial forecast of solar irradiance is required for the locations of the photovoltaic (PV)-systems. Today, mainly numerical weather prediction (NWP) models and, to a lesser extent, satellite-based weather forecast methods are used to provide solar irradiance predictions, especially for long forecast horizons. However, both methods are limited in their temporal and spatial resolution. ASI-based forecast methods can refine this forecast space down to the magnitude of metres and minutes while still reaching lead-times of more than 30 min in the majority of situations [30].

Eye2Sky is an ASI-network in the north-west of Germany, operated by the German Aerospace Center (DLR) - Institute of Networked Energy Systems (VE) with about 30 cameras in operation. It is described in more detail in subsection 1.1. An ASI-network like Eye2Sky has special maintenance requirements. Maintenance can include cleaning, recalibration, testing, or replacing sensors, as well as fixing software-related problems. For any given station, an extended maintenance session can last about 1.5 h. Due to the size of Eye2Sky, the travel time to each station can vary. The mean distance from the operational office of Eye2Sky in the city centre of Oldenburg to an Eye2Sky station is about 32 km. Assuming an average travel speed of $60\,\mathrm{km\,h^{-1}}$, this leads to a total maintenance time of around 2.5 h per station. For 29 stations, this adds up to a maintenance time of about 72.5 h for the whole network. This high time requirement means high operational costs.

Consequently, it is in the operator's interest to minimise maintenance visits. For the installed meteorological sensors, intervals for recalibration and replacement follow fixed schedules. However, until now there have existed no fixed rules for the cleaning intervals of ASIs in Eye2Sky. The importance of regular cleaning of the camera lenses for Oldenburg is unclear. In Sengupta et al. [32] best practices for the collection and use of solar resource data have been summarised by leading solar research institutions, which also include the acquisition and use of ASI image data. However, no standardised methods for the quality control (QC) of ASI images have yet been included. Clean cameras are expected to provide the best image data, but the severity of the impact of soiled lenses on the forecast results of ASI-networks such as Eye2Sky has not been analysed before. Also, the influence of other disturbing factors on the image data quality, like e.g. interfering objects or exposure time variations, has not been investigated before for the Eye2Sky network. For the commercial operation of an ASI network in general, these questions need to be answered to make reliable predictions of the operational costs of a network and to improve the decision-making process of choosing a suitable network topology.

The purpose of this thesis is to first analyse the influence of poor-quality input data on the data processing chain of the nowcasting of Eye2Sky and its interim products by choosing and developing fitting analysis methods for each type of result. The findings of this analysis are then used to develop and validate different methods for the detection of errors in historical data, such as the published dataset of Schmidt et al. [29], as well as for the prevention of errors during real-time operation. Finally, recommendations for the operation of ASI-networks are given based on the findings of this work.

1.1 ASI-network (Eye2Sky)

Eye2Sky is an ASI network of 29 cameras and additional meteorological stations in the north-west of Lower Saxony which provide an extension of about 110 km x 100 km [27]. It has been in operation since 2018 and is designed to provide very short-term solar irradiance forecasts with high spatial- and temporal resolution. Unlike other ASI networks, Eye2Sky covers a large area with a high density of stations. It consists of widely distributed ASIs in the rural area and a subset of close cameras in the urban area of Oldenburg with intersecting fields of view (FOVs). The stations are categorised according to their equipment. Some stations only consist of a single ASI while others have additional meteorological sensors. An overview of the stations of Eye2Sky and their equipped measurement systems is given in Figure 1. An image of a typical Eye2Sky station with additional meteorological sensors (MET-station) can be found in Figure 2.

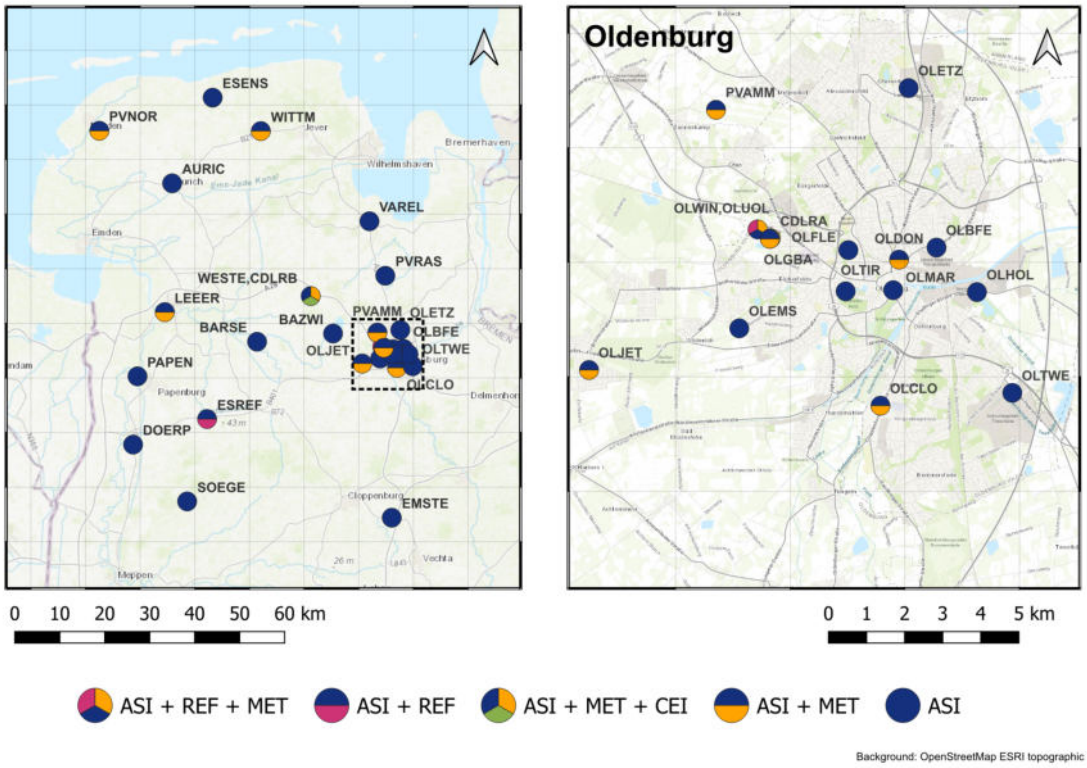

Figure 1: Active operational Eye2Sky all-sky imagers (ASIs) in summer 2025. Reference stations (REF) are equipped with high quality solar trackers and additional instruments. Meteorological stations (MET) are equipped with rotating shadowband irradiometers and further meteorological sensors. Ceilometer stations (CEI) provide cloud height measurements, maps based on [28, edited].

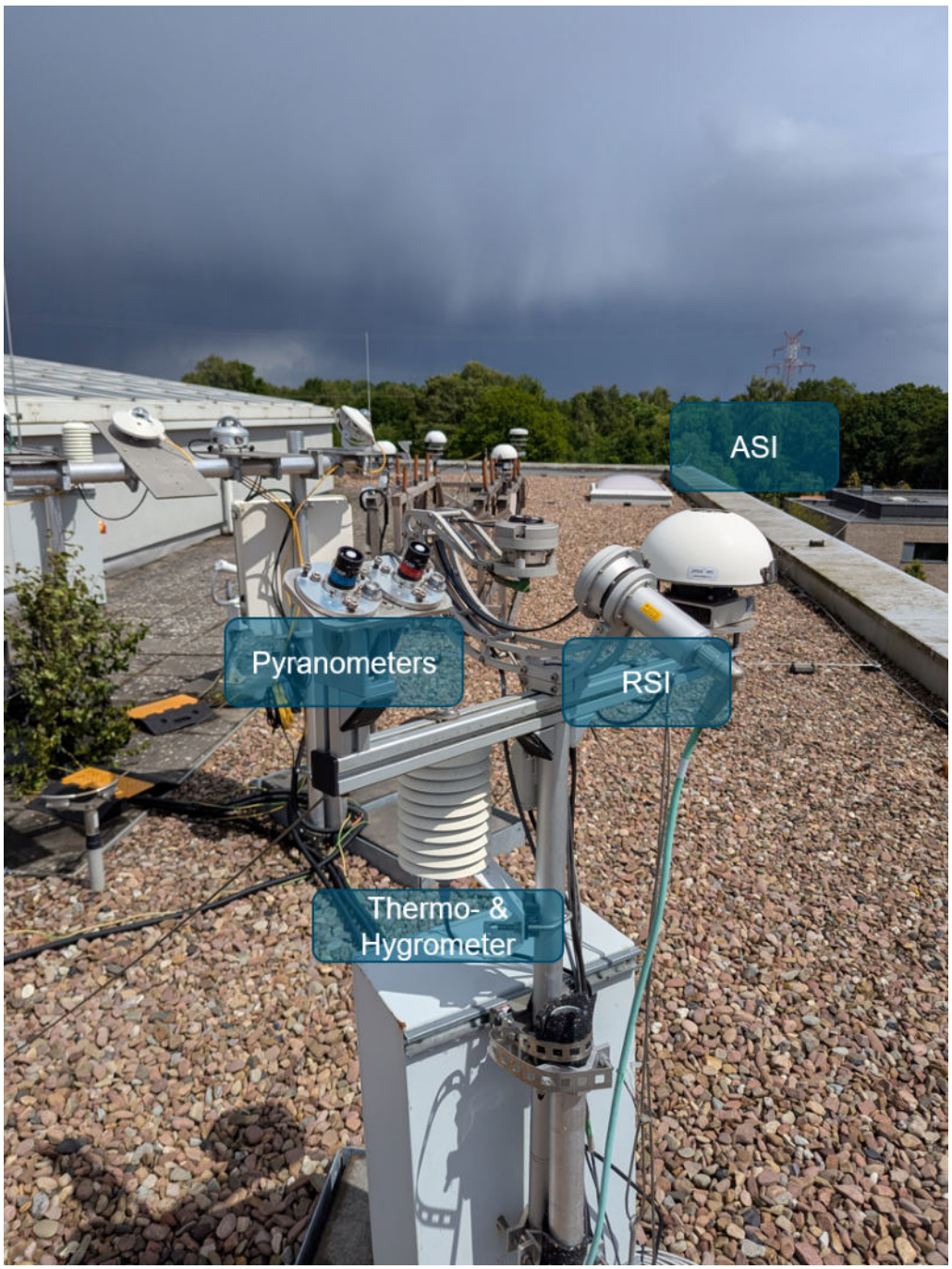

Figure 2: Typical setup of Eye2Sky station (station OLUOL) with all-sky imager (ASI), rotating shadowband irradiometer (RSI) and additional meteorological sensors.

1.2 Definition of ASI error-classes

Different errors can occur during the operation of an ASIs network. In Eye2Sky, cameras with fisheye lenses are used. The advantage of these cameras is, that they are more cost-efficient than cameras with different configurations, like ASIs with hemispheric mirrors. However, the small fisheye lenses make the cameras more susceptible to interfering objects or soiling events. Small objects, e.g. insects, can block a large part of the FOV of the cameras and therefore could potentially have huge influence on the model behaviour. The same is true for soiled parts of the lenses. In Table 1 the main sources of errors have been summarised based on the experiences gained from the operation of Eye2Sky.

Table 1: Overview of main errors in the image data of Eye2Sky

Error type	**Description**	**Typical effects**
Continuous soiling	Continuous soiling over time (e.g. from dust, grease or deposits)	Blurring and scattering, long term
Localised soiling	Sudden, spatially limited soiling of the lens	Dark persistent spots, long term
Interfering objects	Sudden events of blocking the cameras field of view (e.g. by birds, insects etc.)	Covering of parts of the lens, very short term
Deviation of exposure times	Different cameras sensors can have slight deviations of the exposure times	Brighter or darker images, long term
Missing images	Missing images due to e.g. failure, maintenance or corrupted files	No valid image, any time span
Wrong internal/external calibration	Missing or wrong transformation matrices	Wrong rotated and undistorted images, long term
...		

The absence of images can be equated with a reduction of cameras available for the forecasting. The work of Scheper [25] has shown that less dense camera networks can still provide accurate irradiance forecast. For this reason, the error of missing images has not been considered more in-depth in this thesis. The impact of camera calibration errors has been neglected. The internal calibration of all stations, the correction of lens distortions, has been done in advance and is considered to be stable over time. The external calibration corrects any deviation in the orientation of the cameras. If cameras are moved or turned, the external calibrations need to be updated. All stations do automatic regular updates of their external calibration by tracking the course of the moon during nights with a clear-sky moon illuminance of

at least 90% of the full moon value [2]. Although this method only works in case of sufficient visibility during these full moon nights, it is considered accurate for this work because movements of the cameras are assumed to occur rarely. Furthermore, the errors can be calculated in the deviation of pixels of the moon in an image and are shown to be of a lesser extent (see Blum et al. [1]).

In the work of Fabel et al. [13, submitted], a convolutional neural network (CNN) based model for the detection of anomalies is described. This model is designed to detect six common anomalies in ASI images: arthropods, birds, covered lenses, people, soiling and water droplets. To get an overview of the anomalies that occur the most in Eye2Sky, an early version of this model was applied to the image data between 1 April 2022 and 18 April 2022 of the entire operational network. The model was trained on images from Almería, Spain, and has not been adapted for the location of Oldenburg. For this reason, the results should be treated with caution. Samples have also shown that misclassification can occur by directly transferring the model to the location of the Eye2Sky network. However, it is assumed that the result can give a qualitative overview of which anomalies are the most abundant in the Eye2Sky network.

In Figure 3, a bar plot of the results of the anomaly detection model is given for the time period mentioned above. One can observe that covered lenses and soiling are the most common anomalies within the image data of Eye2Sky according to the detection model. The high amount of 'covered lens' detections may correspond to a misclassification of dark images captured at morning or evening. In comparison to soiling, interfering objects, e.g. birds or insects, are not as common in the data. However, this does not necessarily mean that anomalies like soiling also have a higher impact on the forecast results, but it shows that it is worth taking a closer look at these phenomena.

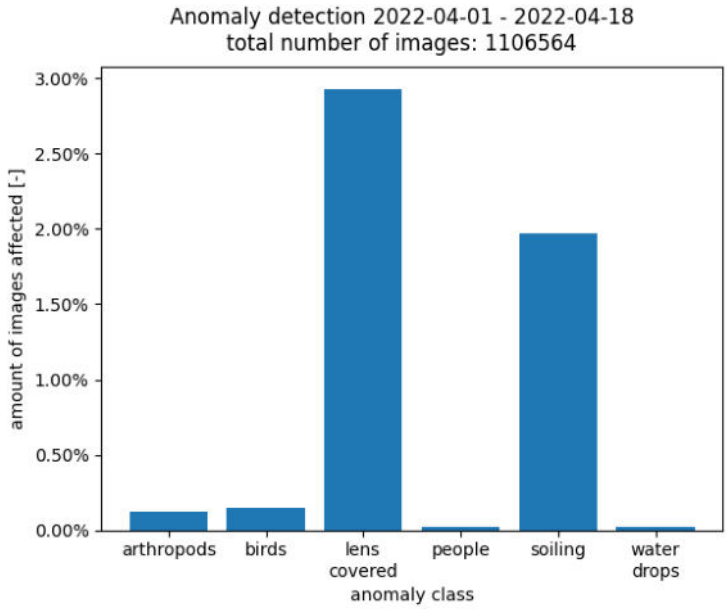

Figure 3: Number of anomalies detected by early version of anomaly detection model of Fabel et al. [13, submitted], directly applied on historical Eye2Sky data for a test period of 18 days.

For the reasons mentioned above, the main focus in this work is on the analysis of continuous soiling, localised soiling, and interfering objects. To illustrate the main error types in more detail, examples are given in Figure 4. Continuous soiling refers to a homogeneous soiling of the entire lens caused by residues that accumulate over time. In Figure 4a one can observe that this type of soiling can lead to blurring of the picture, especially for parts of the image close to the visible sun. In contrast to continuous soiling, localised soiling refers to soiling of only parts of the lens by a sudden trigger event. This can lead to a covering of parts of the cameras FOV (see Figure 4b). The category of interfering objects includes all kinds of interference during the image-capturing process caused by, e.g., insects, birds, or people. These interference events are usually only temporary, but they can also lead to a covering of parts of the image and therefore to missing cloud information. In Figure 4c an example of an interference caused by an insect is given. In addition to these three main error types, analyses of exposure-time deviations are also performed. Different cameras can have small deviations from the target exposure times. This can lead to a slight darkening or brightening of the image. Figure 4d shows two images captured by two different ASIs at the same location with slight differences in their exposure and the resulting differences in the brightness of the image.

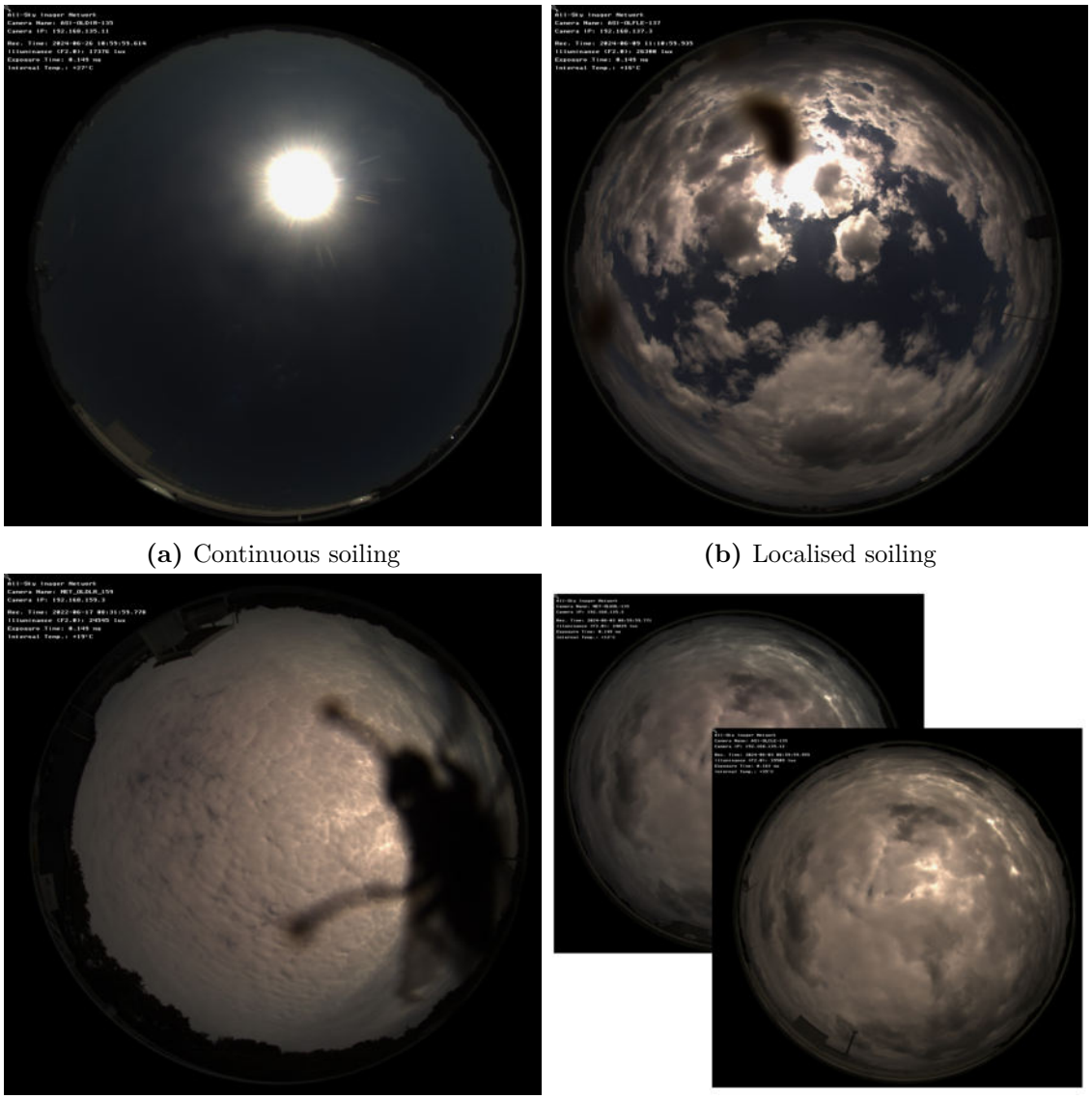

(a) Continuous soiling

(b) Localised soiling

(c) Interfering object

(d) Exposure time deviations

Figure 4: Examples of frequent image errors in Eye2Sky, (a) continuous soiling (blurring of parts of the image close to the sun), (b) localised soiling (big dirt stain at the top, small dirt stain on the left side), (c) interfering objects (insect covering parts of the lens) and (d) exposure time deviations (differences in brightness of images of two all-sky imagers at the same location)

2 Physics-based ASI Nowcasting

In meteorology, the term 'nowcasting' usually refers to short-term weather forecasts with a forecast horizon up to 6 h [26]. There are various weather forecasting methods that differ in their characteristics, such as temporal and spatial resolution, spatial coverage, forecast step size, maximum forecast horizon, and update cycles. For Germany, the NWP model ICON-D2 can provide weather forecasts with a spatial resolution of 2.2 km and a temporal resolution of 15 min with lead times up to 48 h, but its update interval is only 3 h [10]. For satellite-based forecasting methods, the Meteosat Third Generation (MTG) satellite mission, launched in December 2022, will provide images for selected regions every 2.5 min but with a spatial resolution of only 500 m [11]. ASI-based forecasting systems are able to deliver forecasts with very high resolution in space and time and a rapid update cycle. However, they only have a limited forecast horizon and spatial coverage due to their ground-based position and their optical abilities. The approximate temporal and spatial domains of these forecasting methods are visualised in Figure 5.

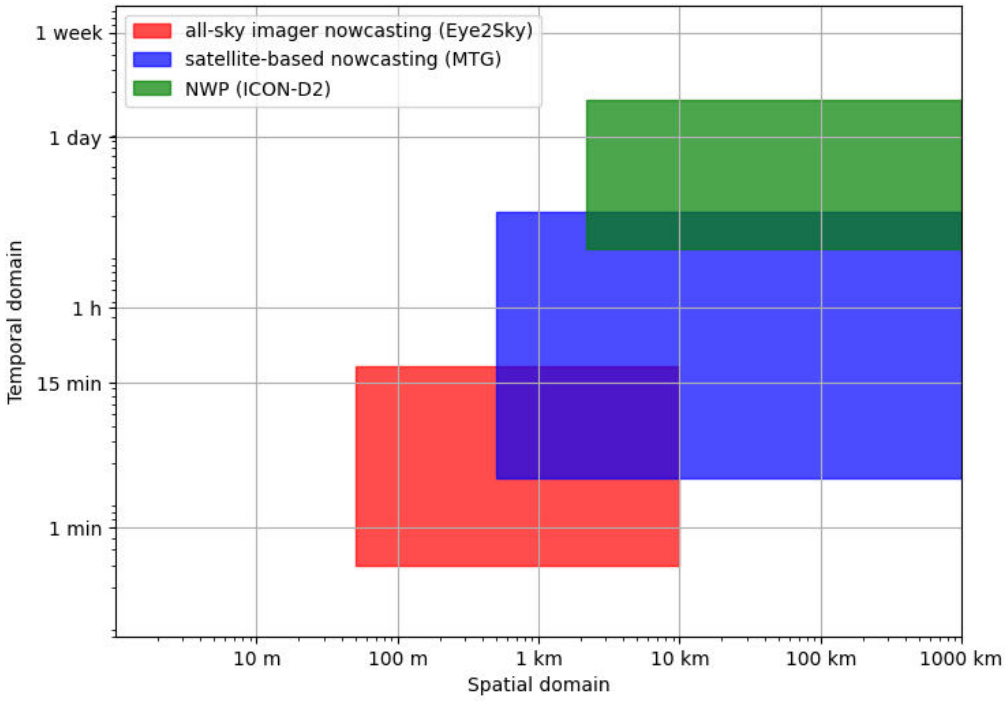

Figure 5: Comparison of the approximate temporal and spatial operating domains of state of the art weather forecasting methods of numerical weather prediction (NWP), satellite-based nowcasting and all-sky imager nowcasting, created on the base of [25]

Due to the high temporal and spatial resolution of ASI-based forecasting methods, small-scale phenomena, and weather situations with high spatial and temporal variability can be predicted with higher precision. Thus, they are particularly well suited to forecasting rapid changing weather conditions (ramps), for example in the event of a thunderstorm. According to Sengupta et al. [32], there are two main

approaches for ASI-based irradiance forecasts. First, physics-based (indirect) approaches, and second, machine learning (ML)-based (direct) approaches. Physics-based approaches in general contain several modules which calculate physical interim results, e.g. cloud mask, cloud base height (CBH), cloud motion vector (CMV) etc., before deriving irradiance forecasts from those results. In general, these interim results correspond to real physical properties and can be validated with measurements. Some of the modules may also consist of ML approaches, meaning that hybrid forms also exist. In contrast to these indirect approaches, fully ML (direct) approaches are designed to provide irradiance forecasts directly from the raw image input.

The data processing chain of Eye2Sky is built on the physics-based (indirect) algorithm WobaS developed by Nouri et al. [21] at DLR - Institute of Solar Research (SF). Eye2Sky uses a further development of WobaS for ASI-networks by Blum [2]. WobaS was built to create solar irradiance forecast maps based on ASI images and other meteorological input data. It consists of several submodules to calculate meteorological interim results such as cloud masks, CBH, CMVs, as well as BNI and diffuse horizontal irradiance (DHI). A simplified overview of the data chain of WobaS is given in Figure 6. These processing steps are considered best practice for indirect approaches according to Sengupta et al. [32]. A complete description of all modules of WobaS is beyond the scope of this thesis. In the following, the main modules of WobaS, which were considered in the quality control (QC)-analysis of this thesis, are described and explained.

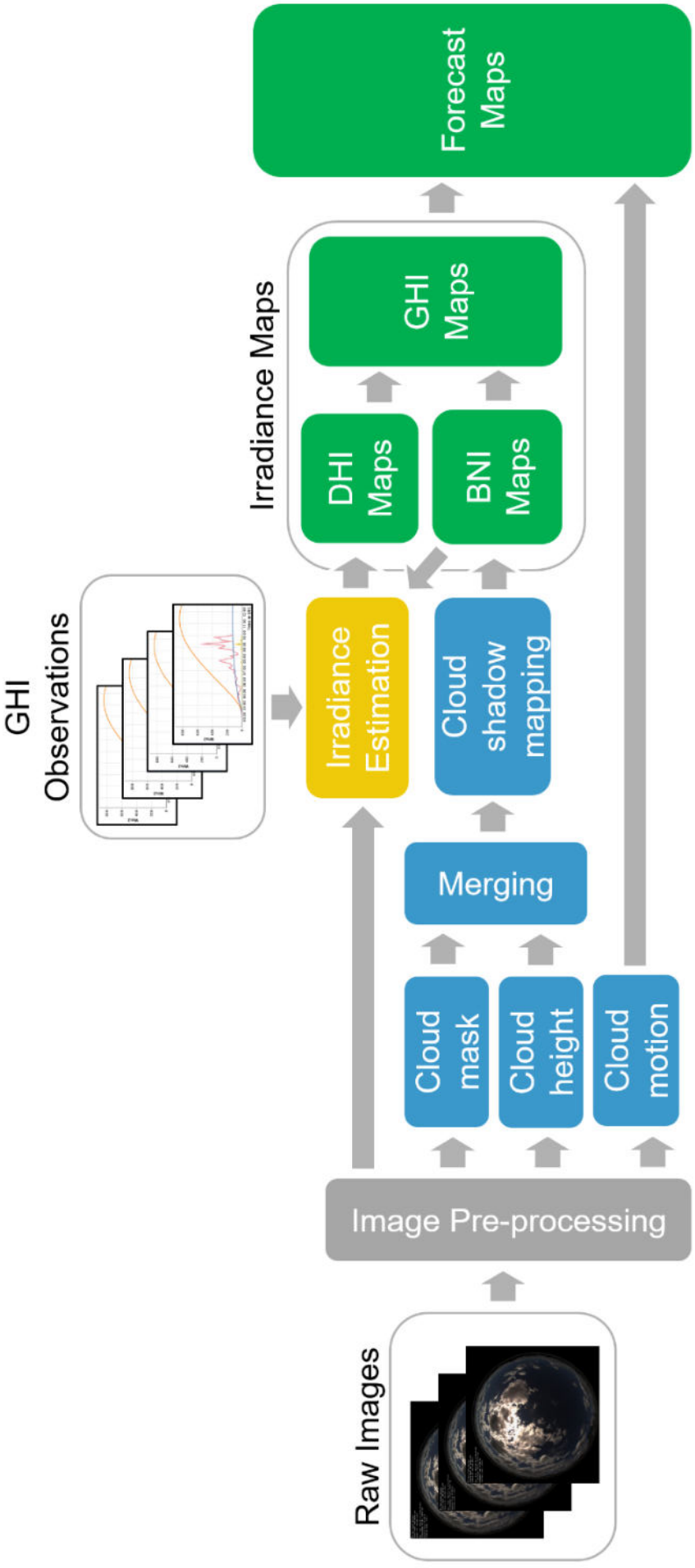

Figure 6: Overview flowchart of the main steps in the WobaS processing chain

2.1 Cloud masking

One of the first steps in the data processing chain of WobaS is the detection of clouds and the creation of cloud masks. This means that the clouds seen in the image are classified into different types of clouds by a semantic segmentation algorithm. In contrast to normal image classification, in which images are classified as a whole, semantic segmentation is the pixel-wise classification of each individual image. Simple models only distinguish between cloud and clear sky; more sophisticated ones can also distinguish different cloud types. WobaS uses a CNN image segmentation algorithm, developed by Fabel et al. [14] at DLR-SF. The CNN approach is based on the U-Net architecture (see [24]). This model is pre-trained on a dataset of 300 000 ASI-images and fine-tuned on a labelled ASI-image dataset with 770 images recorded in Almería, Spain. For simplification, the ten cloud genera, defined in the International Cloud Atlas [7], are summarised into three classes plus one class for the clear sky condition, so the model can distinguish between four valid classes (see Figure 7).

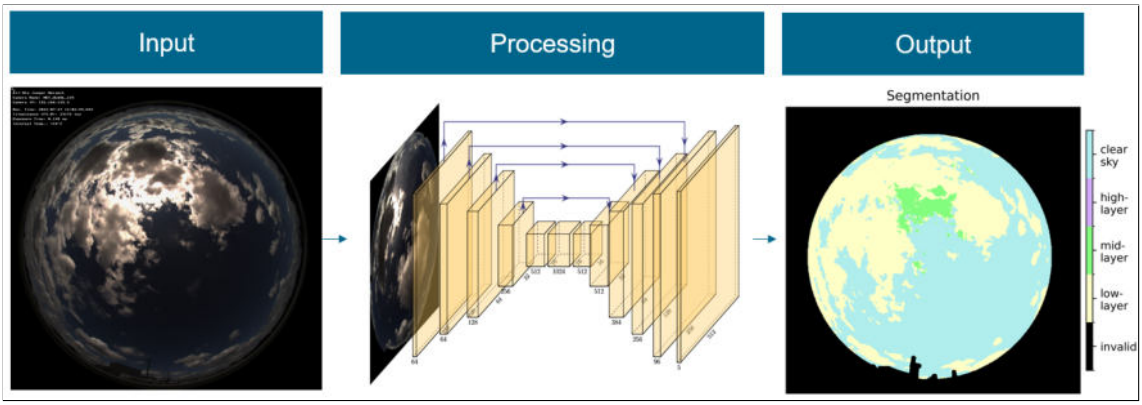

Figure 7: Simplified data flow chart of the CNN algorithm for semantic segmentation of Fabel [12], figure based on [12], edited.

The different cloud classes are named after their typical cloud height ranges. These ranges are summarised in Table 2. The assumption is that the atmospheric conditions in the different cloud layers lead to different optical properties, which can be detected by the model. These classes are based on optical properties, they do not serve as height measurements in the later processing steps. The CBH-estimation of WobaS is done separately from the segmentation by a stereoscopic approach described in subsection 2.2. Further details about the whole semantic segmentation process can be found in the Master's thesis of Fabel [12].

Every cloud class has a corresponding attenuation index (AI), which is a parameter for the attenuation of the BNI of the different cloud types [2]. A high AI corresponds to a low transmittance of the cloud. These AIs are used during the merging and mapping process to determine transmittance of the whole cloud field and the resulting BNI on the ground.

Table 2: Cloud classes for semantic segmentation in WobaS, their typical height ranges and their attenuation index (AI) according to [12].

Cloud class	Height	AI
Clear-sky	-	0
High-layer	>6 km	0.2
Mid-layer	1.8 km to 8 km	0.7
Low-layer	0 km to 2.4 km	1

2.2 Cloud base height (CBH) estimation

Fish-eye images of ASIs provide the pixel information in an azimuth-elevation reference frame. This means that the cloud position above ground cannot be derived directly from single images. In WobaS, this problem is solved by estimating the CBH network-wide using a stereoscopic approach developed by Nouri et al. [19], which is a multi-ASI network implementation of the work of Kuhn et al. [15]. This approach uses the different points of view (POVs) for every predetermined ASI pair with overlapping FOV in the network and merges this information to a global network CBH. The global CBH of the ASI-network serves as an anchor point for a projection plane to translate all the cloud information from an azimuth-elevation reference frame (α, ϵ) to a geo-reference frame (lat,lon).

This stereoscopic approach takes advantage of the different positions of the ASIs inside the network. All distances between the cameras are pre-defined and do not change over time. If the same clouds appear in the FOVs of two different ASIs, their height above ground can be triangulated by using the azimuth-elevation reference frame of each camera. As described in Blum [2], the CBH estimations of all pairs considered inside the network are then used to determine a global CBH by applying a likelihood function on the results of single camera pairs. Short distance pairs provide better CBH estimations for low-layer clouds, whereas ASI-pairs with a large distance are better suited for the CBH estimation of high-layer clouds. For this reason, only pairs with suitable distances are increasingly incorporated into the final decision of the global network CBH algorithm.

When the final network CBH is determined, this information is used for the merge process of WobaS. The stereoscopic network approach can deliver only one single CBH for the whole network. This means that multilayer scenarios, where clouds are observed on different heights above the ground, cannot be mapped. Moreover, gradients of the CBH within the cloud field cannot be considered because only one CBH is chosen for the entire network. As stated in Scheper [25], small errors in the CBH can lead to high errors in the irradiance forecasts. Especially for large zenith angles, a wrong cloud height leads to high projection errors during the shadow-mapping process. Consequently, a high precision of the CBH estimation is required

for valid irradiance forecast results.

2.3 Irradiance maps and Forecasts

The global horizontal irradiance (GHI) is the total amount of radiant power received per area on a horizontal plane. It can be decomposed into two components, the diffuse and the direct component. The direct component corresponds to the part of the irradiance which comes directly from the irradiance of the Sun. The diffuse part combines all the indirect irradiance caused by e.g. cloud reflection, scattering, and albedo (i.e. ground reflection). The diffuse horizontal irradiance (DHI) corresponds to the power of diffuse radiation received on a horizontal plane. The beam (direct) normal irradiance (BNI) is the irradiance directly coming from the direction of the Sun. It can be translated into the same horizontal reference frame by multiplying it with the cosine of the zenith angle θ of the Sun for the given position. The relation of all the irradiance components is summarised in Equation 1.

$$GHI = DHI + BNI \cdot \cos(\theta) \tag{1}$$

Following the calculation of the cloud masks and the CBH calculation, the information is merged into a single two-dimensional attenuation map. During the merging process, the results of every single ASI are ranked with an uncertainty function depending on their position. Every camera has the highest certainty for the centre point of the image and the lowest certainty for large zenith angles. Due to the distortion of the fisheye lenses, the information density within the image is the highest in the centre. Cameras, which are directly positioned under a point in the cloud field, have a higher influence on the results of that location than cameras, in which the cloud information of the target ground position is on the edge of images. After creating the attenuation maps, they are used as input for the shadow mapping process. In this process, the BNI on the ground is calculated by mapping the shadow of the cloud field due to the position of the Sun and the estimated CBH. This results in a map of the BNI on ground with a spatial resolution of 50 m. Together with the predicted DHI of WobaS, the global horizontal irradiance (GHI) maps are calculated. These BNI and GHI maps are then used as a basis for the creation of irradiance forecasts by moving the calculated field according to the estimated CMVs. This leads to forecast results with a lead time step size of 1 min and a forecast horizon of up to 1 h. The end product of WobaS is a georeferenced four-dimensional irradiance data frame with dimensions latitude, longitude, time, and lead time. Examples of gridded irradiance results can be seen in Figure 8.

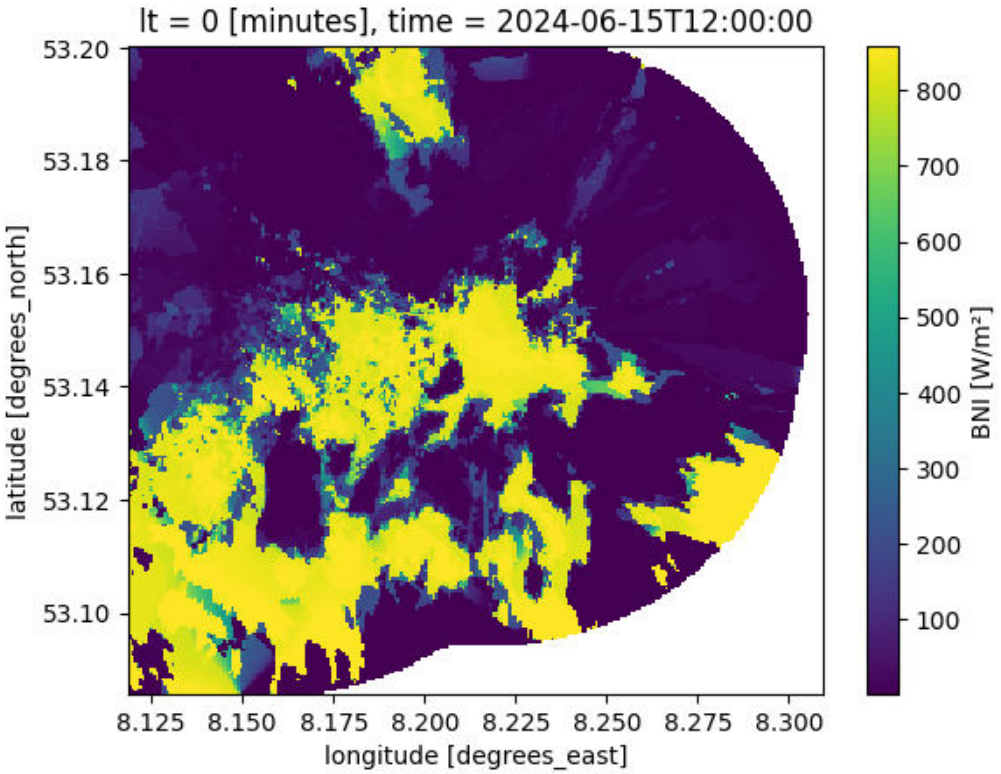

(a) beam (direct) normal irradiance (BNI)

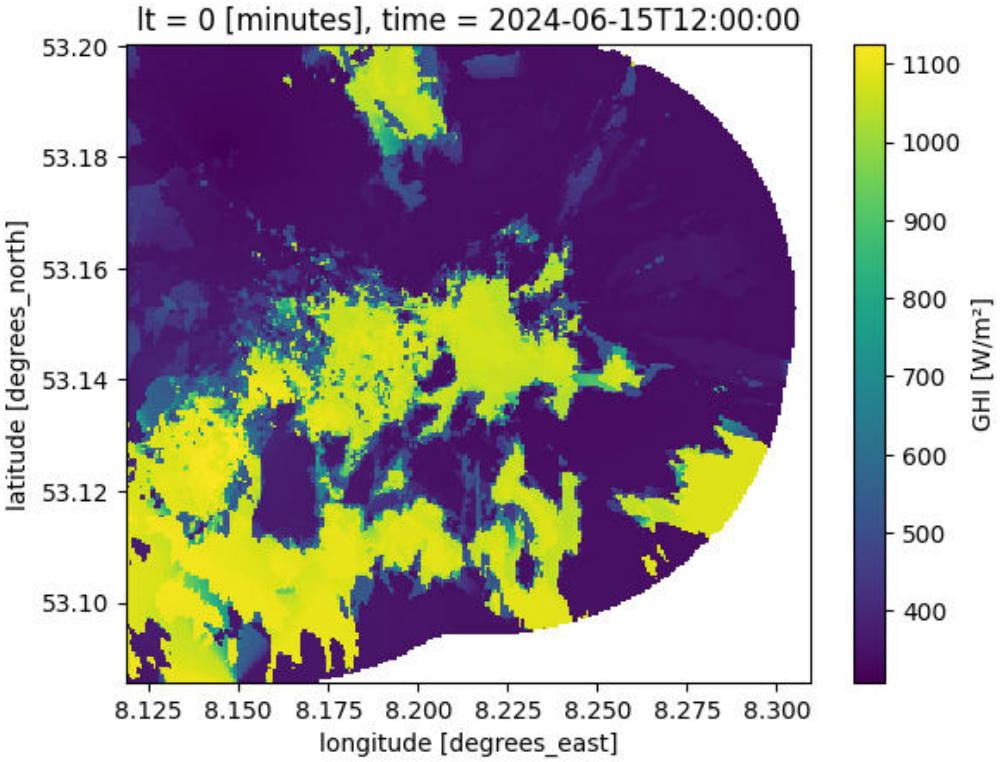

(b) global horizontal irradiance (GHI)

Figure 8: Examples for beam (direct) normal irradiance (BNI) map (a), and global horizontal irradiance (GHI) map (b) for lead time (lt) = 0 min, 15 June 2024 12:00:00 UTC.

3 Study setup

In order to form the basis for the development of new QC methods, the impact of errors on the currently operational processing chain of Eye2Sky has been evaluated in this thesis with the goal of better understanding the severity of different errors before focussing on their detection or prevention. The objective of this work is to systematically test how the main modules of the forecast algorithm WobaS react to poor-quality input data. The primary focus is on the main error sources defined in subsection 1.2. In this section, first general information on the experimental setup of the study is given. Due to the fact that the interim results of the software differ in many ways, different analysis methods are chosen for each module. These are described later.

3.1 Eye2Sky subnetwork configuration

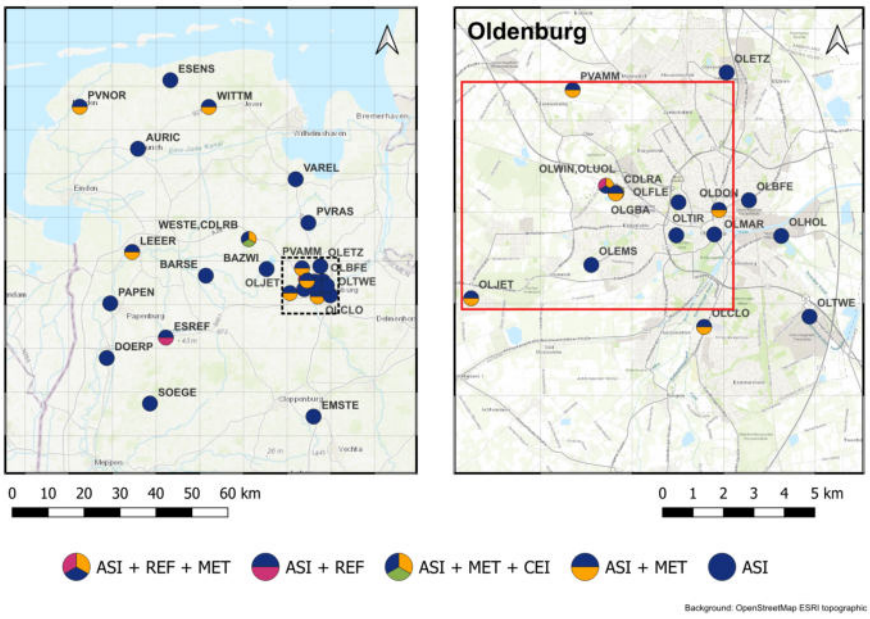

Figure 9: Eye2Sky subnetwork of Eye2Sky used in the study (red box), map based on [28, edited].

The Eye2Sky network is a scientific research network for the forecasting of solar irradiance. Its topology is based on a variety of reasons, such as work safety and accessibility of roof tops among many. However, it is not optimised for commercial or public use cases. The work of Scheper [25] has shown that smaller network configurations of Eye2Sky still lead to good forecast results. These smaller and therefore more cost-efficient configurations are also considered to be more realistic for future applications than the scientific full-density network approach. Due to the high redundancy of cameras in the whole Eye2Sky network, it is expected that the influence of errors may be too small to be visible in the analysis. For these reasons, in this thesis only a subset of the entire Eye2Sky network has been taken into account.

This reduction in complexity not only makes the resulting network topology more realistic, but a smaller network configuration also helps to reduce computation times. This subnetwork has been built virtually around the reference station OLWIN and the experimental setup described in subsection 3.2. The stations were selected or omitted on the software side. No ASIs needed to be dismantled or replaced for this work. The topology of the chosen subnetwork can be seen in Figure 9. An overview of the available measurement equipment can be found in Table 3.

Table 3: Overview of available sensors in subnet of Eye2Sky, stations in alphabetical order including model names of all-sky imagers (ASIs), rotating shadowband irradiometers (RSIs) and further meteorological sensors. * marks all sensors that are not used by the forecasting algorithm. Sensors in brackets have not been used in this evaluation but are part of the measurement system.

Station	Sensors	Models
CDLRA	ceilometer*	LUFFT 15k CHM180102
OLCLE	ASI	Mobotix Q26B-6D
OLMED	ASI	Mobotix Q26B-6D
OLDIR	ASI	Mobotix Q25
OLDON	ASI	Mobotix Q25
	RSI	CSP-Services (2 x LI-COR LI-200)
	(pyranometer)*	LI-COR LI-200R
	(pyranometer)*	LI-COR LI-190R
	(thermo-hygrometer)*	Campbell Scientific 215
OLEMS	ASI	Mobotix Q25
OLFLE	ASI	Mobotix Q25
OLGBA	ASI	Mobotix Q25
	(pyrgeometer)*	Kipp&Zonen CGR4
	(RSI)*	CSP-Services (2 x LI-COR LI-200)
	(pyranometer)*	Kipp&Zonen CMP10
	(anemometer)*	Thies Clima Sensor US
OLJET	ASI	Mobotix Q25
	(RSI)*	CSP-Services (2 x LI-COR LI-200)
	(pyranometer)*	LI-COR LI-200R
	(pyranometer)*	LI-COR LI-190R
	(thermo-hygrometer)*	Campbell Scientific 215
OLMAR	ASI	Mobotix Q25
OLQ71	(ASI)*	Mobotix Q71
OLTIR	ASI	Mobotix Q25
OLWIN	sun tracker*	2 x EKO MS-80
	pyrheliometer*	EKO ML-01
	(pyranometer)*	sunto captpro
	(visibility/weather sensor)*	Campbell Scientific CS125
	(thermo-hygrometer)*	Campbell Scientific CS215
	(rain gauge)*	Thies Clima 5.4032.35.008
PVAMM	ASI	Mobotix Q25

3.2 Experimental setup for soiling analysis

For the QC-analysis of the Eye2Sky network, an experimental setup has been installed on the rooftop of the WindLab building W33 on the campus of Carl-von-Ossietzky University of Oldenburg in Wechloy next to the reference station OLWIN (see Figure 10). Station OLWIN is equipped with a solar tracker following the exact position of the Sun in the sky and additional meteorological sensors. Due to its higher accuracy versus the rotating shadowband irradiometers (RSIs), it acts as a reference for the irradiance measurements in this thesis. The experimental setup used in this thesis includes the operational meteorological station OLUOL and additional installed ASIs. These ASIs differ in terms of their cleaning methods and equipment. ASI OLCLE (clean), OLUOL, and OLQ71 have been cleaned manually almost every week. In contrast, ASI OLDIR (dirty) was not cleaned at all during this analysis. In addition, ASI OLMED is equipped with an automatic cleaning system. Some ASIs are also equipped with a ventilation-heating-system (VHS) to protect the lenses from freezing and dust. The differences between model Mobitix Q25 and Mobotix Q26B-6D have initially been considered negligible for this experiment. ASI OLQ71 is equipped with a Mobotix Q71. This model has some different functionalities, which were not relevant for this work. For this reason, it has been excluded from the analysis, but it is mentioned for the sake of completeness. In Table 4, all ASIs of the experimental setup are listed. This setup has been chosen to assess the importance of cleaning methods, cleaning intervals, and cleaning equipment.

Table 4: Experimental setup on building W33 of all-sky imagers (ASIs), cleaning method, cleaning interval and status of ventilation-heating-system (VHS).

ASI	Model	Cleaning method	Cleaning intervals	VHS
OLUOL	Mobotix Q25	manually cleaned	weekly	True
OLCLE	Mobotix Q26B-6D	manually cleaned	weekly	False
OLMED	Mobotix Q26B-6D	automatically cleaned	daily	True
OLDIR	Mobotix Q25	not cleaned	-	True
(OLQ71)	Mobotix Q71	manually cleaned	weekly	False

Within the Eye2Sky network, ceilometer cloud height measurements are only available for some locations because ceilometers are costly. None of the stations in the experimental setup on top of building W33 is equipped with a ceilometer. Therefore, the stations OLGBA and CDLRA on the roof of the DLR-building (about 400 m away from the experimental setup) were used to validate the CBH estimation of the network (see Figure 11). Station OLGBA is maintained regularly and therefore is considered clean for this work. The exact cleaning intervals of all the stations in the study setup during the main analysis periods can be found in the excerpt of the network logbook in Appendix A Figure 49.

Figure 10: Experimental setup of this study on rooftop of building W33, stations equipped with all-sky imagers (ASIs) (OLCLE, OLDIR, OLMED, OLQ71, OLUOL), and meteorological reference station (OLWIN).

3.3 Cloud masking impact assessment

One of the first steps in the processing chain of WobaS is the creation of cloud masks. This is done using the semantic segmentation algorithm of Fabel [12] as described in subsection 2.1. The segmentation results for each station are given in the form of two-dimensional arrays of the same size as the input images. The value inside of an array corresponds to the class of the same pixel in the original image. To make the results of all stations comparable, it is necessary to first equalise any differences in the external orientation of the cameras. Every camera was calibrated before to determine its external orientation. This calibration data can be used to rotate all the arrays so that the results of two stations are aligned. Then, all resulting arrays are cropped to remove unnecessary parts of the boundary mask. These preprocessing steps are done to make direct comparisons of results from different stations possible.

3.3.1 Continuous soiling

For the analysis of the cloud masking process, there is no direct reference data within Eye2Sky. The cloud mask results can therefore not be compared with any direct ground truth. For the analysis of the impact of continuous soiling on the semantic segmentation, the segmentation results of the manually cleaned station OLCLE have been compared with the uncleaned station OLDIR and the automatically cleaned station OLMED. It is assumed that the segmentation results of the cleaned ASIs are closer to reality than the results of soiled cameras, because the data for the

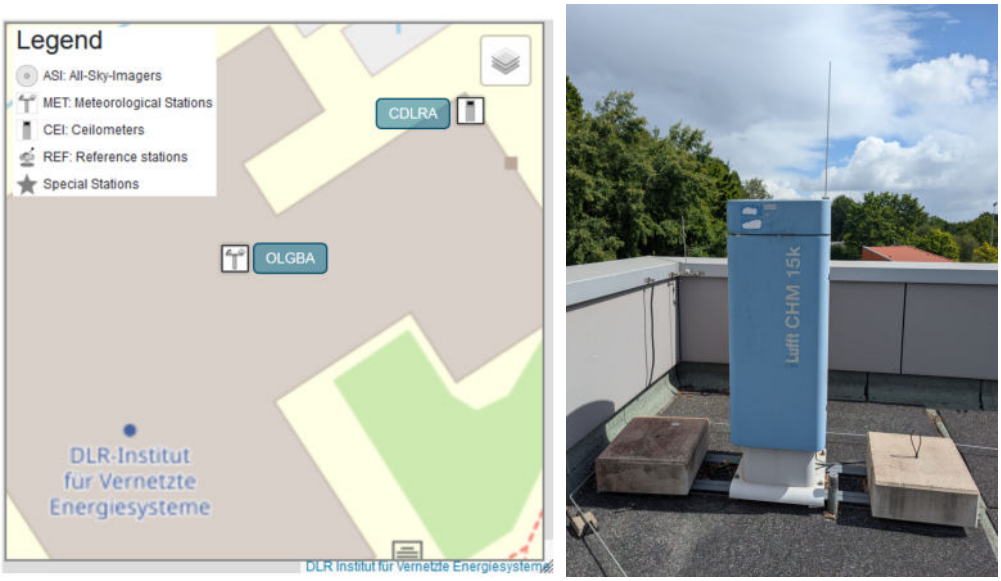

(a) Overview of building A, background map from ©OpenStreetMap, edited **(b)** Eye2Sky ceilometer station CDLRA

Figure 11: Building A of German Aerospace Center (DLR) - Institute of Networked Energy Systems (VE).

fine-tuning process of the semantic segmentation model was manually checked and selected. For this reason, the segmentation results of the manually cleaned station OLCLE have been used as a reference for this work. Image examples of all three stations are given in Figure 12.

(a) Example image of regularly cleaned Eye2Sky station OLCLE. **(b)** Example image of uncleaned Eye2Sky station OLDIR. **(c)** Example image of automatically cleaned Eye2Sky station OLMED.

Figure 12: All-sky imager image examples of cleaning analysis, June 26 2024 11:00 UTC.

All stations are located on the same rooftop of building W33 at Campus Wechloy and therefore have been exposed to exactly the same weather conditions. Therefore, a comparison of the results of the different stations should reveal the influence of continuous soiling on semantic segmentation. This analysis should also reveal any differences between both cleaning methods. The month of June 2024 was chosen as the analysis period for this work. The cloud masking is calculated on every image of all cameras and timestamps separately, so the amount of data and the cloud-type

representation inside that period are considered sufficient for this analysis. After the preprocessing steps mentioned above, the segmentation results can be compared by building a confusion matrix between the different results. These confusion matrices are used to visualise the accuracy of a classification task. Every pixel of the segmentation result of one station is compared with the same pixel of the segmentation result of the other station. The diagonal of this matrix represents all pixels that are classified as the same cloud type by both stations. All other values correspond to a different classification of the two stations. The semantic segmentation algorithm of Fabel [12] only distinguishes five different classes: clear-sky, high-layer clouds, mid-layer clouds, low-layer clouds and invalid. In addition to these five classes, a new class has been introduced for this work. This class is called 'masked' and visualises the invalid pixels which are, in fact, inside the image border mask of the image and correctly classified as invalid by the model. This differentiation can reveal any potential deviation between the invalid pixels classified by the module and the pixels which are actually part of the mask and are set invalid by a boundary condition. The total attenuation index error E_{AI} can be calculated by weighting the segmentation results for both stations with the corresponding AI. This error serves as a simple metric for the actual impact of misclassifications on the irradiance forecast.

$$E_{AI} = \frac{\sum_{c=0}^{n_c} u_{pix,c} \cdot AI_c - \sum_{c=0}^{n_c} u_{pix_{ref},c} \cdot AI_c}{n_{pix,valid} \cdot N} \tag{2}$$

The index c corresponds to the valid segmentation class, n_c is the number of valid classes, $n_{pix,valid}$ the number of valid pixels per image and N the number of images. $u_{pix,c}$ corresponds to the number of pixels classified as class c by the analysed station, and AI_c represents the attenuation index of class c. The suffix $_{ref}$ marks the same for the chosen reference station.

3.3.2 Localised soiling and interfering objects

For the analysis of the impact of localised soiling and interfering objects, cameras from the entire subnetwork, described in subsection 3.1, were considered. Due to the fact that the segmentation is done on single images without temporal dependencies in-between the timestamps, both error types have been considered comparable and have been summarised in this analysis. Apart from the experimental setup on building W33, there are no redundant ASIs at the same locations, so the evaluation of the segmentation between both phenomena has been done only qualitatively or by comparing timestamps before or after an event. For the analysis of interfering objects, examples from the entire pool of stations within the subnetwork were considered. For the analysis of localised soiling, station OLFLE was selected. This station was soiled unforeseen in April 2024 and cleaned in June 2024, so it was soiled locally longer than a month and therefore is well suited for this analysis. Then, all results are qualitatively discussed in section 4. Examples of localised soiling and interfering objects from Eye2Sky are given in Figure 13.

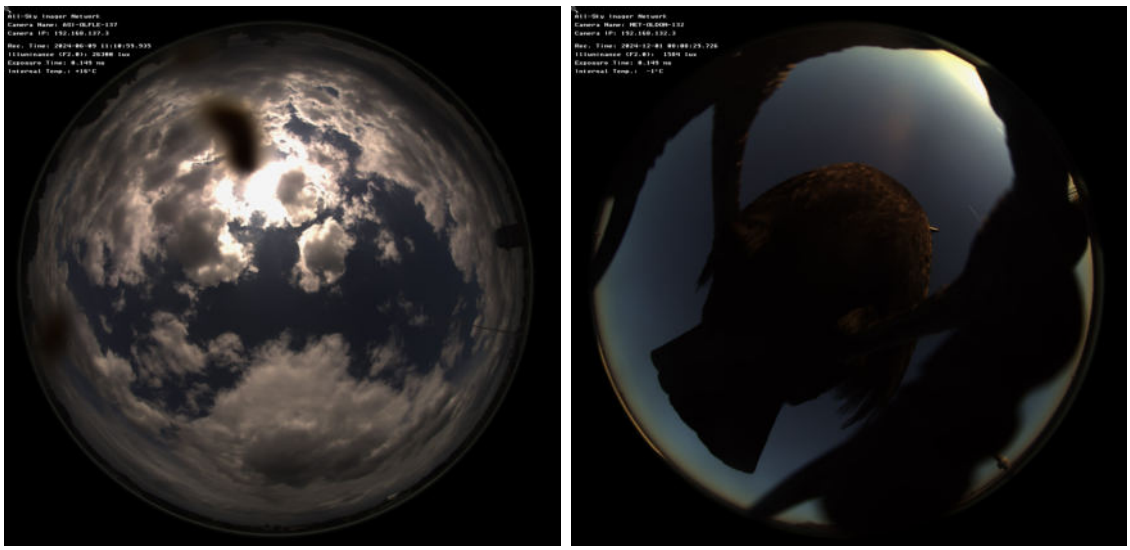

(a) Localised soiling on Eye2Sky station OLFLE, June 9 2024 11:11 UTC.

(b) Interfering object (bird) on Eye2Sky station OLDON, December 1 2024 08:08:30 UTC.

Figure 13: All-sky imager image examples of localised soiling and interfering objects.

3.4 Cloud base height impact assessment

Although the semantic segmentation classes are named after the various cloud-layers, they are imprecise and do not necessarily correspond to the real heights of the clouds. This becomes clear when comparing the segmentation results with cloud height measurements. In Figure 14, the results of station OLGBA, and the ceilometer measurements of station CDLRA have been compared for 6 June 2024.

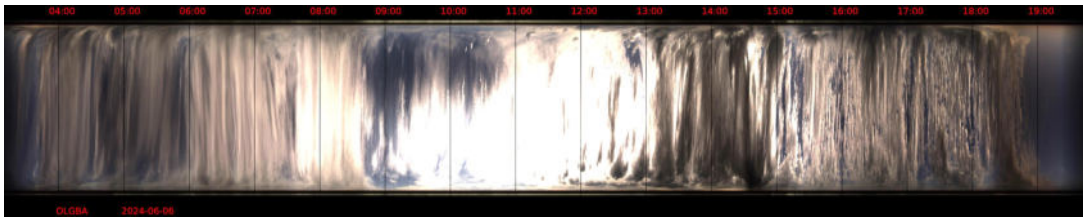

(a) Keogram of Eye2Sky station OLGBA.

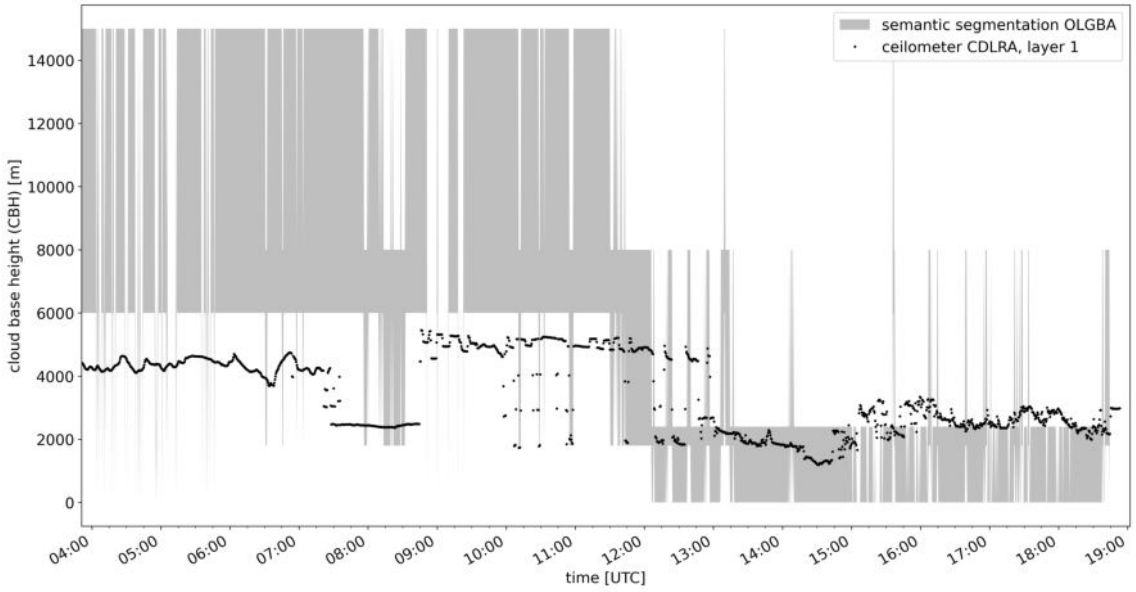

(b) Comparison of segmentation results of centre point of Eye2Sky station OLGBA with ceilometer measurements of station CDLRA.

Figure 14: Validation of segmentation results as indicator for cloud heights for 6th of June 2024.

Figure 14a shows the keogram of station OLGBA on this date. To create a keogram, the centre line from bottom to top of every raw image is taken and merged along the recording time on the x-axis. These keograms help to get a quick overview of the weather conditions during the corresponding day. The segmentation results have been converted into a time series of CBH ranges according to Table 2 by taking the central point of the two-dimensional segmentation array. This point corresponds directly to the clouds above station OLGBA. These ranges were then compared with the true ceilometer measurements of station CDLRA. The ceilometer of station CDLRA can measure the cloud heights of up to 4 cloud layers, but only the measurements of the first cloud layer have been considered ground truth for this

work, because it is expected that in multi-cloud-layer situation, the first cloud layer is the most significant when using ground-based ASIs. Ceilometer measurements are available in the form of NetCDF-files with a temporal resolution of 15 s. They have been smoothed by building the rolling mean with a window size of 3 timestamps and interpolated with nearest-neighbour interpolation to fit the timestamps of the image capturing.

Figure 14b reveals that the segmentation results differ from the measured cloud heights. Especially for high-layer clouds, the deviations are greater than for low-layer clouds. According to the work of Nouri et al. [20], the transmittance of mid- and high-layer clouds can vary greatly. This variation can also lead to different optical properties and therefore to a higher variation in the segmentation results. For these reasons, the segmentation results cannot serve as cloud height estimates for the network.

For the CBH estimation, WobaS uses the stereoscopic approach described in section 2. According to Scheper [25], small errors of the CBH can have a strong impact on the final irradiance forecast results. This thesis investigates whether these errors can be caused by soiling of the lenses. To achieve this goal, the CBH QC-analysis is divided into two parts. First, only the results of single ASI pairs within the network have been analysed. Afterwards, the ceilometer measurements were compared with the global results of the entire subnetwork by replacing the cameras of the experimental setup on the software side and starting forecast runs for every configuration. To analyse the impact of soiling, pairs were built between station OLGBA and the ASI stations of the experimental setup (see Table 4). OLGBA was chosen because it has an overlapping FOV with the ASI of the experimental setup and is regularly maintained. Its distance from the experimental setup is about 400 m. All results were evaluated for the location of station OLGBA because it is the closest to the ceilometer CDLRA. Due to a failure of the ceilometer, only days in between 1 June and 24 June 2024 were analysed. Following the investigation of the ASI pairs, the output of the global subnetwork was analysed. Both results were compared with the cloud height measurements of the ceilometer. Excluded were all situations where values were missing in the prediction or in the measurements. Clear sky situations have not been included in the analysis because no valid CBH value can be assigned during these periods. To quantify the error, different error metrics were introduced and compared. These are described below.

n is the number of data points for the given time period, CBH corresponds to the predicted cloud base height, and $C\hat{B}H$ is the height of the first cloud-layer measured by the ceilometer. i corresponds to the index of the given data point

for each time stamp. The mean absolute error (MAE) is a simple metric for the performance of the model, which is not sensitive to outliers (see Equation 3).

$$MAE_{CBH} = \frac{1}{n}\sum_{i=1}^{n}|CBH_i - C\hat{B}H_i| \tag{3}$$

To investigate whether lens soiling leads to model bias, the mean bias error (MBE) was introduced as an error metric for the analysis (see Equation 4).

$$MBE_{CBH} = \frac{1}{n}\sum_{i=1}^{n} CBH_i - C\hat{B}H_i \tag{4}$$

The root mean square error (RMSE) has also been introduced as an error metric (see Equation 5). It is more sensitive to high scattering and outliers than the MAE.

$$RMSE_{CBH} = \sqrt{\frac{1}{n}\sum_{i=1}^{n}(CBH_i - C\hat{B}H_i)^2} \tag{5}$$

According to Blum [2], for the measurement of cloud heights, higher deviations can be expected for higher clouds. The same applies for the predicted cloud heights. For this reason, the relative root mean square error (rRMSE) has been chosen as an error metric to relativise large deviations for large altitudes (see Equation 6). $\bar{C\hat{B}H}$ corresponds to the mean value of the observation.

$$rRMSE_{CBH} = \frac{\sqrt{\frac{1}{n}\sum_{i=1}^{n}(CBH_i - C\hat{B}H_i)^2}}{\bar{C\hat{B}H}} \tag{6}$$

As described in section 2, different camera distances are suited for different CBHs. Consequently, the error analysis has been done separately for each cloud layer by filtering the data according to the cloud height definitions in Table 2.

During this work it was noticed that the camera models Mobotix Q25 and Mobotix Q26B-6D do have slight differences in their exposure times. The target exposure time for all stations is 160 µs. However, for the Mobotix Q25 this results in an exposure time of 149 µs, for the Mobotix Q26B-6D in an exposure time of 163 µs. To investigate exposure time variations, the Mobotix Q26B-6D stations OLCLE and OLMED have been set to an exposure time of 147 µs during May 2025 to mimic the behaviour of the rest of the network. The CBH results were compared with the results of June 2024 to better understand whether deviations in exposure times can influence the CBH estimation.

3.5 Irradiance forecast impact assessment

The results of the irradiance forecast of WobaS are given in the form of multidimensional arrays with the dimensions t (time), lat (latitude), lon (longitude) and lt (lead time). The forecast is only calculated for the GHI and the BNI. The impact of errors on the final results of WobaS was analysed by building different subnetwork configurations. In the computation runs, the stations of the experimental setup were replaced on the software side. The rest of the network remained the same. By replacing only the cameras on top of building W33, it is expected that the error of continuous soiling may be made visible. This analysis is divided into two parts. Firstly, the results are compared in the spatial domain using the network configuration with station OLCLE as a reference. Secondly, the results are analysed in the temporal domain by selecting the location of station OLWIN from the forecast maps and using the irradiance observations of OLWIN as reference.

For the analysis of the spatial domain, the resulting irradiance maps were compared using difference maps. These maps are created by subtracting the gridded irradiance data from the analysed network configuration with the reference network for a given lead time. This reveals any spatial deviations of the different results per moment in time. In addition, the error can be quantified by introducing error metrics. The spatial MAE (Equation 7), the spatial MBE (Equation 8) and the spatial RMSE (Equation 9) were calculated for the gridded data. The index $p = (\text{lat, lon})$ represents one position on the map. The constant n_p represents the number of valid gridded data points. The term $IRRAD$ is a placeholder for one of the irradiance components (BNI, DHI or GHI). The suffix $_{ref}$ indicates the same component for the reference network configuration with station OLCLE.

$$MAE_{IRRAD}(t, lt) = \frac{1}{n_p} \sum_{p=1}^{n_p} |IRRAD_p(\text{t,lt}) - IRRAD_{ref,p}(\text{t,lt})| \tag{7}$$

$$MBE_{IRRAD}(\text{t,lt}) = \frac{1}{n_p} \sum_{p=1}^{n_p} IRRAD_p(\text{t,lt}) - IRRAD_{ref,p}(\text{t,lt}) \tag{8}$$

$$RMSE_{IRRAD}(t, lt) = \sqrt{\frac{1}{n_p} \sum_{p=1}^{n_p} (IRRAD_p(\text{t,lt}) - IRRAD_{ref,p}(\text{t,lt}))^2} \tag{9}$$

For the analysis of the temporal domain, the location of the experimental setup is chosen because the meteorological reference station OLWIN is located on the same roof and can be used as reference. For this location the above-mentioned error metrics were calculated for the time series depending on the lead time but with the measurements from station OLWIN as reference ($IRRAD_{obs}$). The index ts represents the given time stamp, the constant n_t represents the number of data points in the time series. This leads to the following equations for the temporal

MAE (Equation 10), the temporal MBE (Equation 11) and the temporal RMSE (Equation 12).

$$MAE_{IRRAD}(\mathrm{lt}) = \frac{1}{n_t} \sum_{ts=1}^{n_t} |IRRAD_{ts}(\mathrm{lt}) - IRRAD_{obs,ts}(\mathrm{t+lt})| \tag{10}$$

$$MBE_{IRRAD}(\mathrm{lt}) = \frac{1}{n_t} \sum_{ts=1}^{n_t} IRRAD_{ts}(\mathrm{lt}) - IRRAD_{obs,ts}(\mathrm{t+lt}) \tag{11}$$

$$RMSE_{IRRAD}(\mathrm{lt}) = \sqrt{\frac{1}{n_t} \sum_{ts=1}^{n_t} (IRRAD_{ts}(\mathrm{lt}) - IRRAD_{obs,ts}(\mathrm{t+lt}))^2} \tag{12}$$

4 Results

In the following section, the results of the QC analysis of WobaS are presented and discussed.

4.1 Cloud masking analysis

The impact analysis of the three main error types continuous soiling, localised soiling, and interfering objects has been split into two parts. In the first part, the impact of continuous soiling is analysed and discussed. In the second one, the same is done for impact of localised soiling and interfering object.

4.1.1 Continuous soiling

Figure 15 below shows the confusion matrix between the segmentation of the cleaned station OLCLE and the uncleaned station OLDIR of June 2024, where OLCLE is the reference station in this diagram.

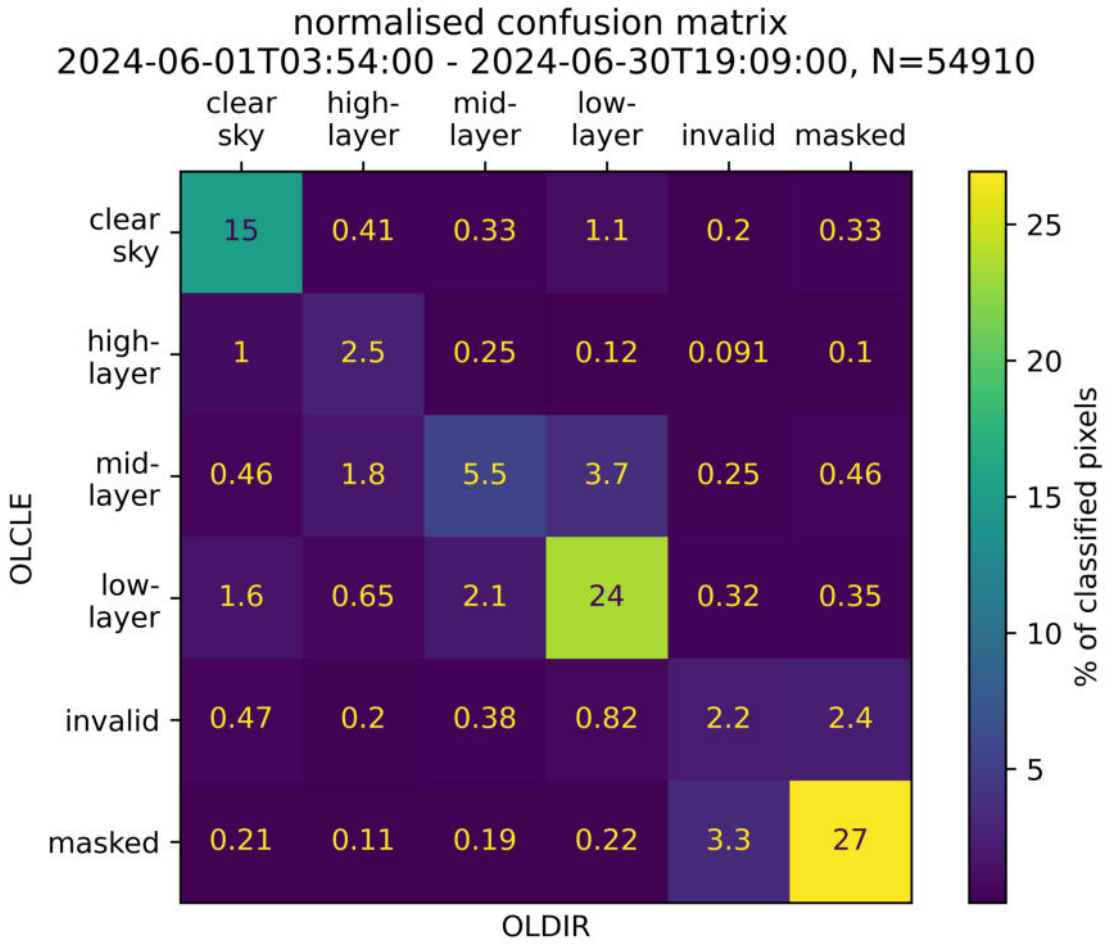

Figure 15: Confusion matrix between segmentation results of cleaned station OLCLE and uncleaned station OLDIR for June 2024, normalised by the total amount of images N and pixels per image.

When the pixels in both images are classified as the same, they appear on the

diagonal of the confusion matrix. Every off-diagonal value corresponds to a different classification between the stations. In addition to the valid classes (clear-sky, high-layer, mid-layer, and low-layer), a distinction is also made between the classes 'masked' (any pixel of the image part of the border mask) and 'invalid' (any pixel which is additionally classified as invalid by the model without boundary condition). One can see that confusion between both stations mainly occurs between neighbouring cloud layers, especially for mid-layer clouds. This matches the general model behaviour of the segmentation algorithm described in Fabel et al. [14]. Despite these differences, the calculated total attenuation index error E_{AI} for the entire period is only $-0.021\,88$. (see Equation 2). This means that the total impact of continuous soiling on cloud transmittance is relatively small. In addition, one can also see symmetrical deviations between the segmentation of low-layer clouds and clear-sky, which may be caused by interferences on both stations caused by e.g. rain droplets. However, it can be observed that not all differences are spread symmetrically between the left and right side of the confusion matrix. For some classes, there is a slight trend towards a specific misclassification for uncleaned ASI OLDIR, e.g. between the classes clear-sky and high-layer clouds or between neighbouring cloud layers. It becomes clearer when looking at the confusion matrices of the corresponding weather conditions. For this reason, two days have been chosen for a closer analysis. The first was 26 June 2024, a day with mostly clear sky conditions and some high-level clouds (Figure 16), and the second one was 6 June 2024, a day with variable weather conditions and different cloud levels (Figure 19). The keograms for both days can be found in Figure 44 in Appendix A.

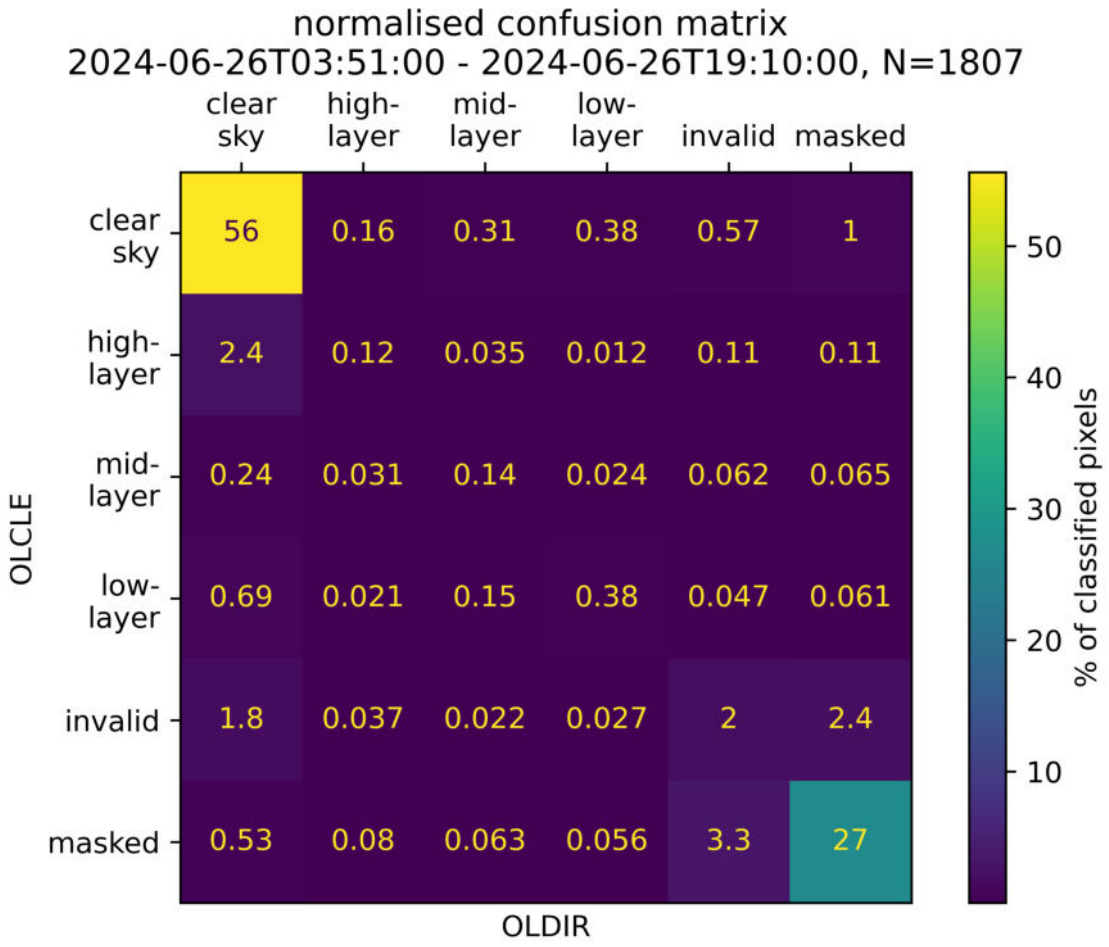

Figure 16: Confusion matrix for segmentation results of cleaned station OLCLE and uncleaned station OLDIR for single clear-sky day with high-layer clouds for 26 June 2024, normalised by the total amount of images N and pixels per image.

Figure 16 shows the confusion matrix on 26 June 2024, a day with mainly clear-sky conditions with some high-layer clouds. According to the work of Fabel et al. [14], the distinction between non-neighbouring cloud layers of the model is reliable. Also, clear-sky is classified with high accuracy. However, the article shows that large numbers of high-level clouds can be misclassified as clear-sky. This behaviour can also be observed in the Eye2Sky network. In Figure 16 it can be seen that the model has problems distinguishing between clear sky and high-layer clouds for the uncleaned camera OLDIR. Pixels classified by station OLCLE as high-layer clouds (and to some extent invalid pixels) are classified as clear-sky by station OLDIR.

In Figure 17 one can find raw image examples of station OLCLE and station OLDIR for the day mentioned above. The comparison between Figure 17a and Figure 17b reveals that continuous soiling leads to a blurring-effect of the image. The high-level clouds around the sun appear with less contrast. These blurred images have some optical similarity to images of clear sky conditions with high atmospheric turbidity (see Figure 17c).

(a) Raw image of cleaned Eye2Sky station OLCLE with high-layer clouds, 26th of June 2024.

(b) Raw image of uncleaned Eye2Sky station OLDIR with high-layer clouds, 26th of June 2024.

(c) Example image from Almería, Spain, of clear sky with high turbidity, taken from [12].

Figure 17: Comparison of raw images of cleaned station OLCLE, uncleaned station OLDIR and ASI image from Almería, Spain.

According to López and Batlles [16] and Power and Goyal [23], the turbidity in southern Spain is on average higher than the turbidity in northern Germany, so it is expected that images of high-turbidity clear sky conditions are over-represented in the training data when transferring the model directly to northern Germany. As stated by Fabel [12], the model has difficulty distinguishing between high-level clouds and clear-sky on days with high turbidity. Figure 18 shows the segmentation results for station OLCLE, OLDIR and OLMED at 11:00 UTC of the same day. It can be seen that the same kind of confusion also appears for high-layer clouds on a continuously soiled lens. High-layer clouds around the Sun are misclassified as clear-sky by station OLDIR whereas the cleaned stations OLCLE and OLMED classify them correctly. However, for the cleaned cameras OLCLE and OLMED these thin high-layer clouds can only be detected by the ASI when they appear close to the Sun in the image. It is expected that they are also present in the rest of the image. That means that the improvement of the classification of high-level clouds by cleaning the cameras is small. Also, these thin high-layer clouds do not have a great impact on the cloud's transmittance, their AI is 0.2 and therefore only slightly higher than the attenuation index of clear sky conditions, which is 0. The total attenuation index error E_{AI} for the whole day is only $-0.013\,39$. This means that these misclassifications have only a minor impact on the irradiance results of the Eye2Sky network for this day.

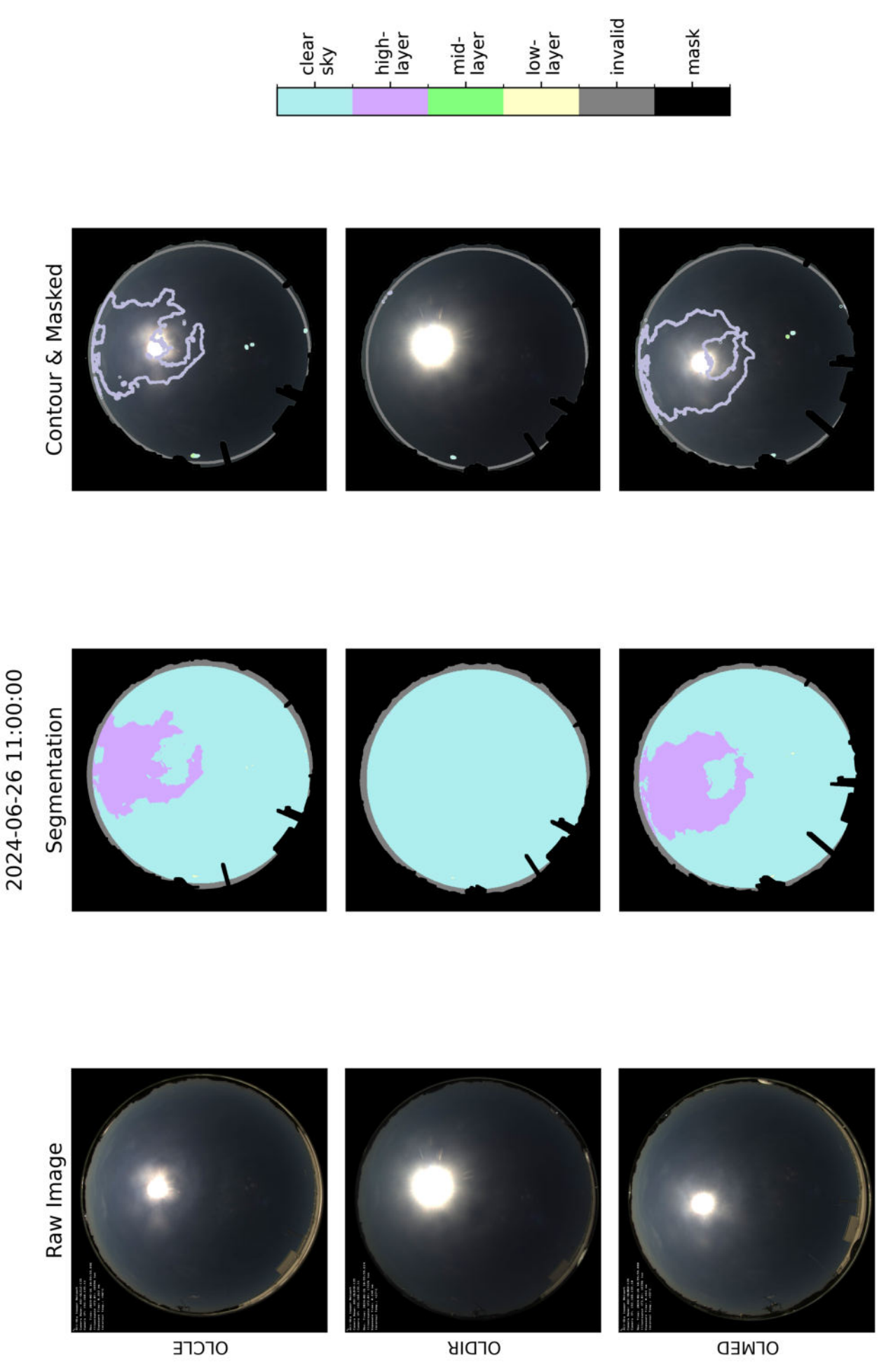

Figure 18: Segmentation results of manually cleaned station OLCLE, uncleaned station OLDIR and automatically cleaned station OLMED, 26th of June 2024. It can be seen that station OLDIR does not detect the high-layer clouds, especially in the area around the Sun.

Figure 19 shows the confusion matrix of 6 June 2024, a day with variable weather conditions. This day was chosen because all three cloud types are present in the segmentation results of this day. In this figure one can see that the model has difficulties in correctly classifying mid-layer conditions for images of OLDIR. A large proportion of pixels classified as mid-layer clouds by station OLCLE are classified as high-layer or low-layer clouds by station OLDIR.

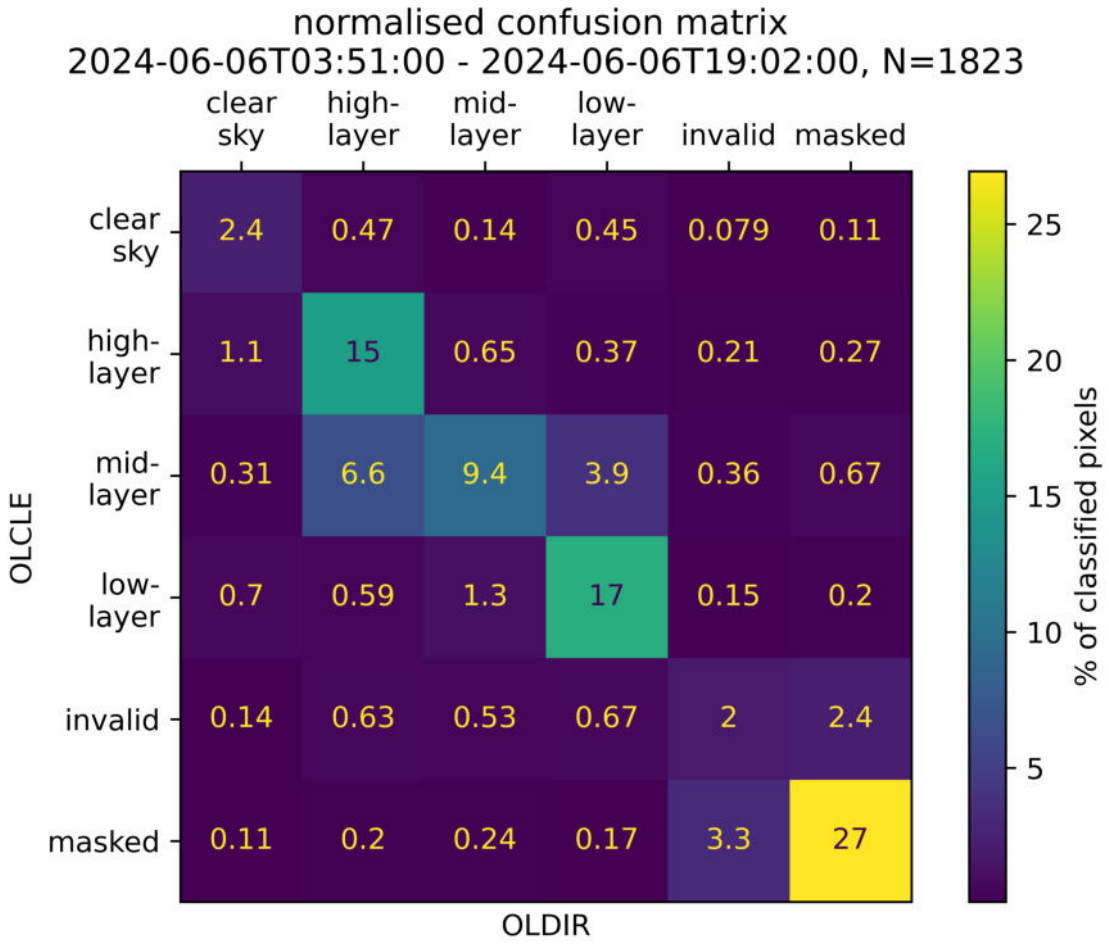

Figure 19: Confusion matrix for segmentation results of cleaned station OLCLE and uncleaned station OLDIR for single day with variable weather conditions, 6 June 2024, normalised by the total amount of images N and pixels per image.

The segmentation results of the stations OLCLE, OLDIR, OLMED and OLUOL for the same day at 12:00 UTC are shown in Figure 20. It can be observed that the same kind of misclassification of station OLDIR appears in the results of manually cleaned station OLUOL as well. That means that these differences in the results do not necessarily correspond to continuous soiling. Contrary to the initial expectation that the models of the used Mobotix cameras capture similar images, it was noticed that the Mobotix Q25 and Mobotix Q26B-6D camera models have differences when setting the exposure times. The set target exposure time is 160 µs for all stations during daylight. However, the resulting value set by the camera hardware

for the Mobotix Q25 is 149 µs, and for the Mobotix Q26B-6D it is 163 µs. Both stations OLDIR and OLUOL are equipped with a Mobotix Q25 and therefore shoot slightly darker images. This can lead to differences during segmentation. Due to the fact that no ground truth data is available, it cannot be said with certainty which segmentation results are better. Nevertheless, a sensitivity of the semantic segmentation model to the exposure time can be observed.

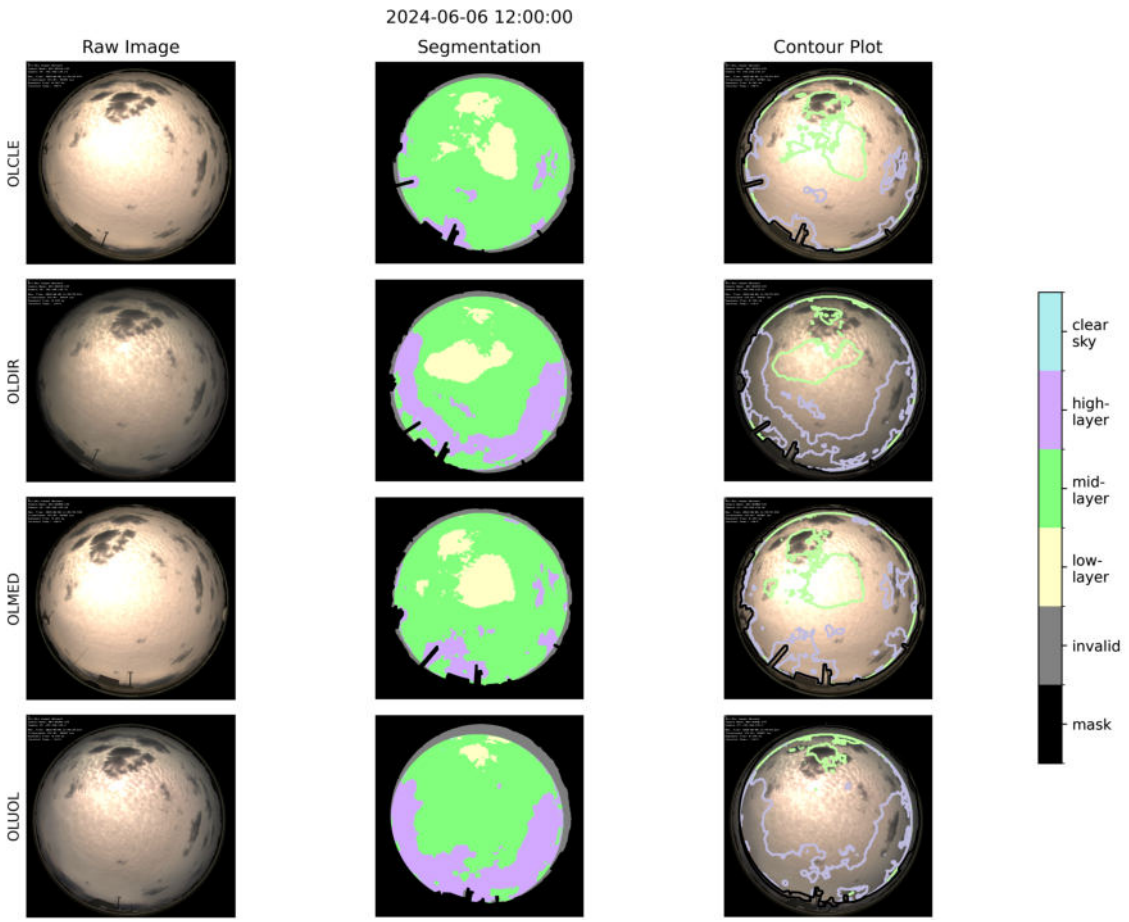

Figure 20: Segmentation results of manually cleaned stations OLCLE and OLUOL, automatic cleaned station OLMED and uncleaned station OLDIR, 6 June 2024 12:00 UTC.

In contrast to high-layer clouds, which typically consist of ice crystals, low-layer and mid-layer clouds normally consist of water droplets. These physical similarities can also lead to optical similarities. The similarities between the optical properties make the distinguishing also a complex task for humans. The data set used to train the segmentation algorithm was created manually. As a result, misclassification is expected to already be included in the training data to some extent. Figure 21a shows the results of the accuracy analysis from Fabel et al. [14] for the model compared to the validation data. Figure 21b shows the confusion matrix of June 2024 but calculated per class. The classes ‘invalid’ and ‘masked’ have been summarised. In contrast to the confusion matrices shown before, both matrices here

show the accuracy per class separately. In this case, all columns add up to 100% (may include rounding errors). The prediction is on the left, the reference on the bottom. Also, the order of the classes has been changed to make the matrices comparable. Because the different cloud classes were not equally present in June 2024, deviations to the model accuracy are expected to some extent. However, by comparing the general accuracy of the model with the confusion matrix in Figure 21b, it becomes clear that the impact of continuous soiling on the model is about the same magnitude as the general model error. Due to the fact that no real ground truth data is available for the Eye2Sky network, no significant impact of continuous soiling on the general accuracy of the segmentation algorithm could be made visible.

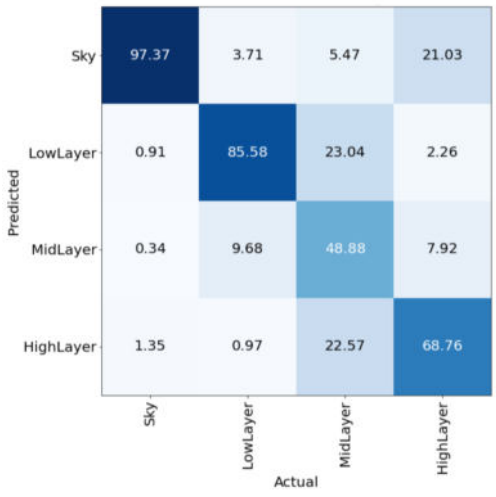

(a) Model accuracy matrix

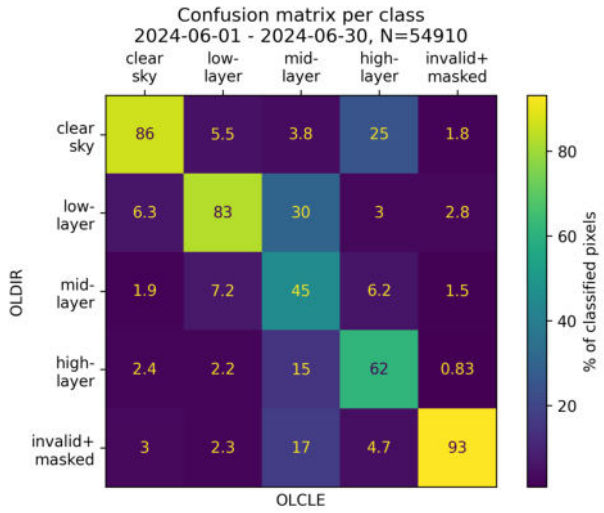

(b) Confusion matrix for station OLCLE and OLDIR per class

Figure 21: Model accuracy of segmentation algorithm in percentages per class separately taken from Fabel et al. [14] (a), confusion matrix for June 2024 per class separately (b), (prediction on the left, reference on the bottom).

4.1.2 Localised soiling and interfering objects

In this section, the influence of localised soiling and interfering objects on the cloud masking process of WobaS is analysed. The semantic segmentation algorithm is performed on each ASI image individually without taking into account previous timestamps. For this reason, both phenomena were summarised in this analysis.

Figure 22 shows a sequence of images and their segmentation results of the Eye2Sky station OLDON during an event with an interfering object. A bird was blocking parts of the lens.

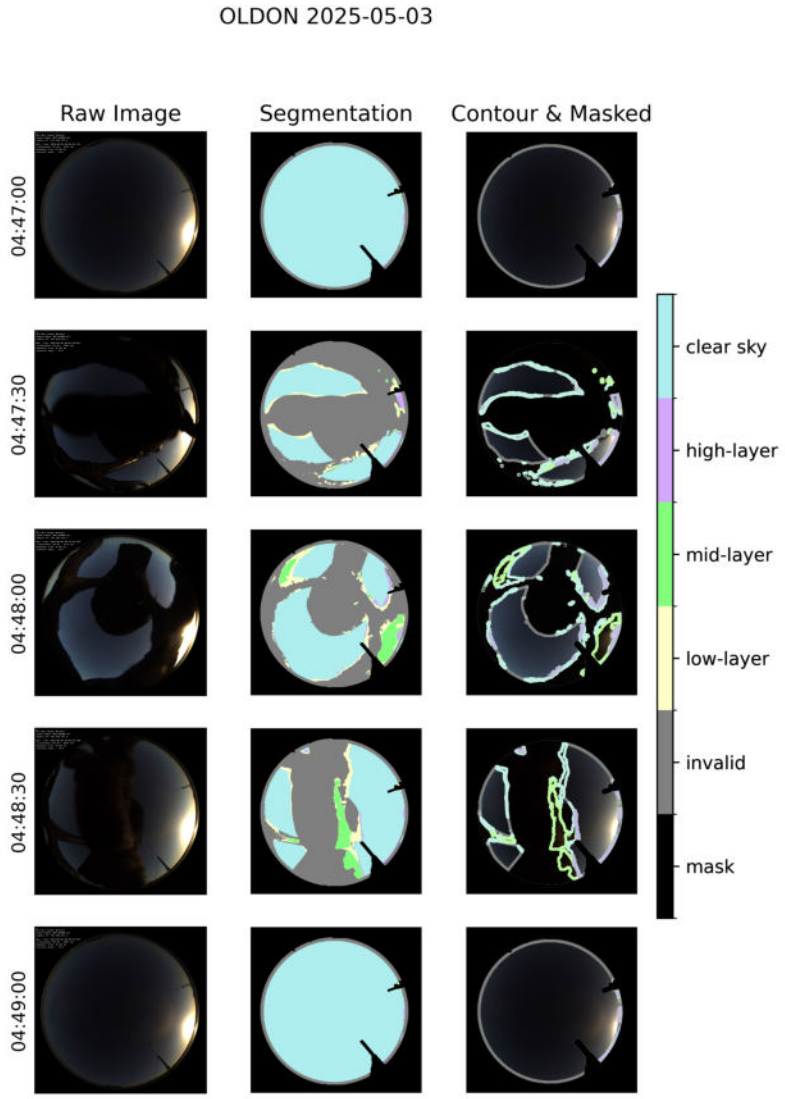

Figure 22: Segmentation results during interfering event (bird) of Eye2Sky station OLDON, 3 May 2024.

When looking at the resulting segmentation, it can be observed that most of the dark parts of the interfering object are correctly classified as invalid by the segmentation model. However, brighter parts can be classified as different cloud-layers. The timestamps before and after the event reveal that there are no clouds present.

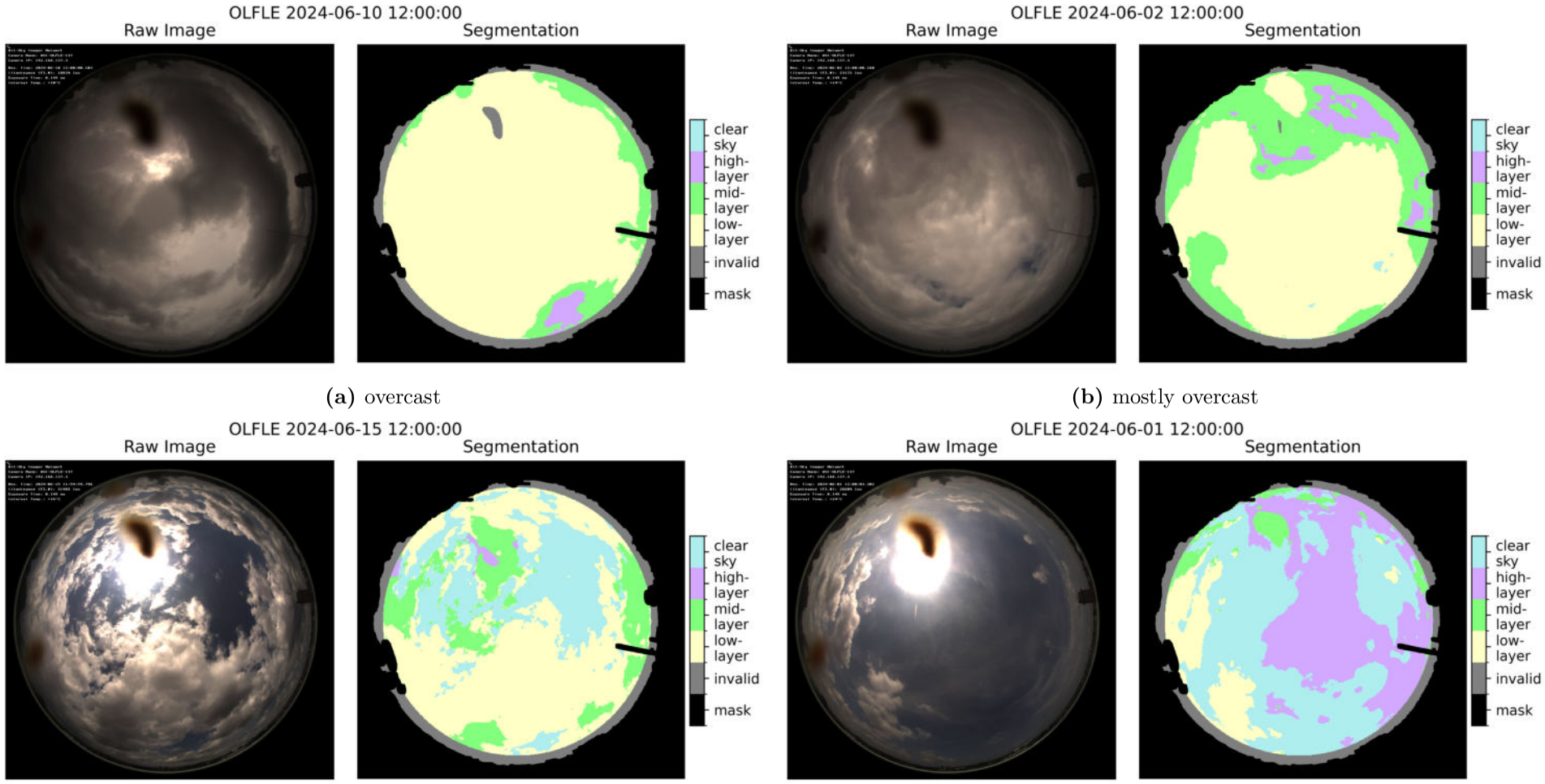

(a) overcast

(b) mostly overcast

(c) mixed conditions

(d) mostly clear sky and high-layer clouds

Figure 23: Results of semantic segmentation algorithm for localised soiled station OLFLE, examples from June 2024.

The above-mentioned model behaviour can also be observed for localised soiling. The station OLFLE was locally soiled at the beginning of June 2024. Looking at different segmentations during this period, the impact of localised soiling can be made visible. Figure 23 shows the segmentation results of station OLFLE for four days with different weather conditions. In Figure 23a and Figure 23b situations with low BNI were chosen. One can observe that the segmentation algorithm correctly classifies dark pixels of the soiled location as invalid to some extent. However, Figure 23c and Figure 23d reveal that for brighter images, these pixels are also classified as valid cloud layers.

The behaviour of the model of classifying objects as invalid is unintentional. Objects of the surrounding, e.g. buildings, antennas, etc., are masked out with true black boundary masks before the training process. This means that the model has learned to interpret dark objects as part of the boundary mask and therefore classifies them as invalid. This behaviour can be beneficial for the merging of the segmentation results for interfering objects. However, in the Eye2Sky network, there are situations where this behaviour can lead to misclassification of valid clouds. For very dark clouds, such as those that occur during thunderstorms, cloud fronts may also be classified as invalid. An example is given in Figure 24. The correct detection of these rapid weather changes and the corresponding drop in irradiance is crucial for ASI forecasting because they also lead to a rapid decrease in PV power production that cannot be reliably predicted with other forecasting methods.

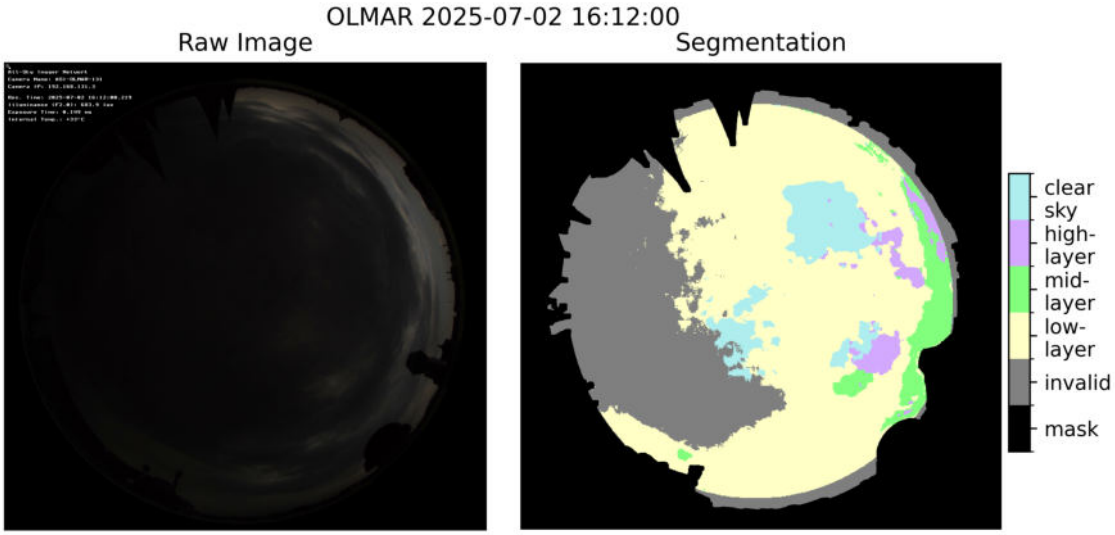

Figure 24: Segmentation results of Eye2Sky station OLMAR with upcoming thunder storm front, 2 July 2025.

4.2 CBH estimation analysis

In the following section, the impact of continuous soiling on the CBH estimation algorithm of WobaS is analysed. This includes the analysis of the CBH estimation results of the individual ASI pairs and the global results of the subnetwork configurations. The subnetwork configurations were built by taking the operational Eye2Sky subnetwork and adding one ASI each of the experimental setup (OLCLE, OLDIR, OLMED & OLUOL). In addition, analyses of the influence of deviations in exposure times on the CBH estimation are shown and discussed.

For the analysis of the CBH estimation of WobaS, the results were compared with the ceilometer observations of station CDLRA. Based on these ceilometer measurements, the MAE, the MBE, the RMSE, and the rRMSE were calculated. For the stereoscopic CBH estimation algorithm, not all ASI pairs are equally suited. Due to their different view angles, short-distant cameras are better for the estimation of low clouds, whereas far-distant cameras are better for the estimation of high clouds. In order not to distort the error metrics, the errors were therefore also calculated for each cloud layer separately. For this, the cloud layer definition of the semantic segmentation algorithm was used (see Table 2). In general, the error of short-distant pairs is expected to be lower for low-layer clouds and vice versa. In addition, the network is expected to deliver more robust results than the individual pairs, so the total error of the subnetworks should be lower.

Figure 25 shows different error metrics of the CBH estimation of WobaS for the time between 1 June and 24 June 2024 for every camera in the subnetwork paired with ASI OLGBA and for the global subnetwork results of all subnetwork configurations. Due to a failure of the ceilometer CDLRA, the last six days of that month could not be taken into account for the analysis. Figure 25a shows the MAE, Figure 25b the MBE, Figure 25c the RMSE and Figure 25d the rRMSE of the CBH estimation for this period.

Looking at the different error metrics for the ASI pairs (marked with x), one can see that there are no significant differences between the stations in the experimental setup. It was expected that the errors for the pairs with the cleaned stations OLCLE, OLMED and OLUOL are smaller than for the uncleaned station OLDIR. However, this cannot be confirmed by the error metrics. The pair with station OLCLE shows slightly better results for high-clouds in the MAE, the RMSE and the MBE. However, the same could not be seen for the other cleaned stations. By comparing the station pairs with the map in Figure 9 one can see that the main factor influencing the error metrics are the distances between the ASIs. Like expected, the error of far apart cameras is greater for low-layer clouds and the error of close cameras is

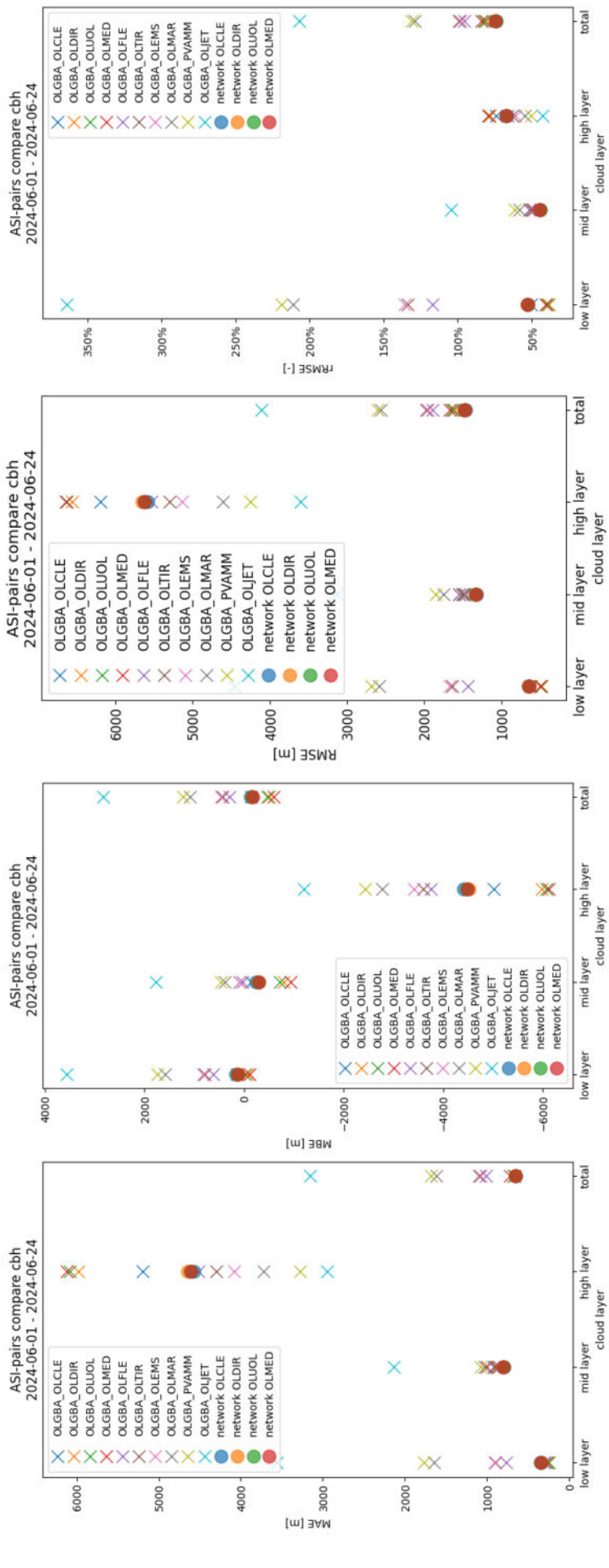

(a) MAE (b) MBE (c) RMSE (d) rRMSE

Figure 25: Mean absolute error (MAE), mean bias error (MBE), root mean square error (RMSE), and relative root mean square error (rRMSE) of cloud base height estimation of WobaS in relation to the ceilometer measurements between 1 and 24 June of 2024 for the location of station OLGBA. (x) marks the results of the individual ASI pairs, (●) marks the results of the global subnetwork with different selected ASIs in the experimental setup.

greater for high-layer clouds. Station OLJET is the furthest station from station OLGBA and has the lowest error for high-layer clouds in all metrics. The stations of the experimental setup OLCLE, OLMED, OLDIR and OLUOL are the closest to station OLGBA and perform better for low-layer clouds.

Looking at the CBH errors of the entire subnetwork configurations (marked with •), one can see that the algorithm performs better for low-layer clouds than for high-layer clouds. The reason for this could be that when defining the subnetwork topology, very distant cameras were omitted. However, comparing the network error metrics, one can see that they are almost the same for all configurations. This means that small deviations of single ASIs, e.g. caused by soiling, do not have a large influence on the global CBH estimation of WobaS. Due to redundancy of ASIs within the network, the CBH results are robust to influences of single cameras.

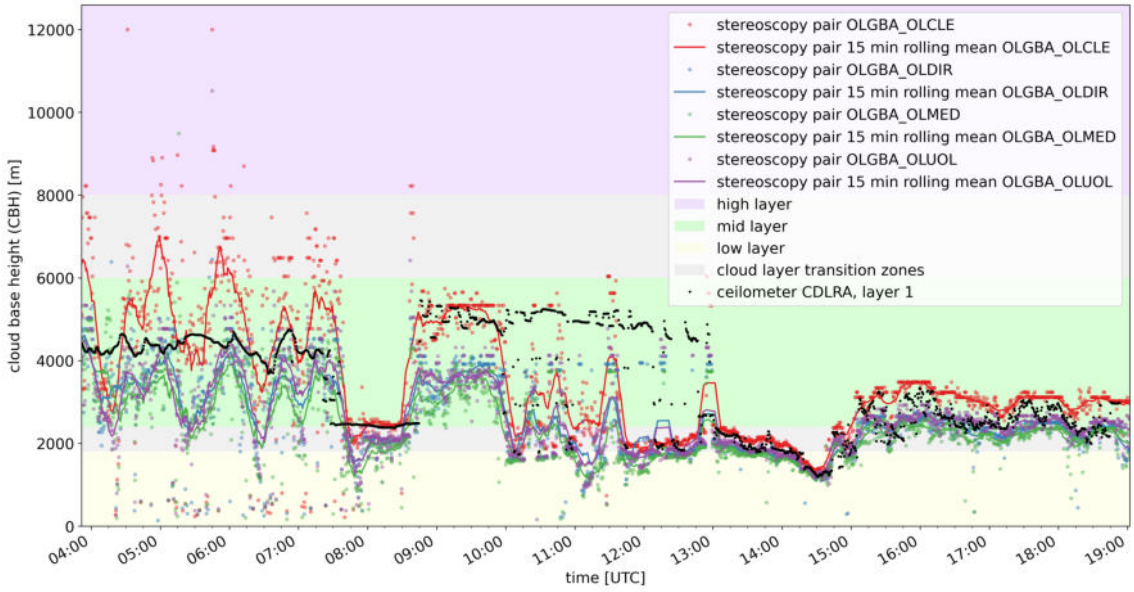

Figure 26: Results of the cloud base height for stations of experimental setup and station OLGBA for all timestamps and with 15 min rolling mean compared to ceilometer cloud height measurements of station CDLRA, evaluated for the location of OLGBA, 6 June 2024.

Figure 26 shows the results of the CBH estimation of WobaS for the camera pairs with OLGBA and the stations of the experimental setup described in subsection 3.2 next to the measurements of the ceilometer CDLRA for 6 June 2024, a day with mostly mid- and low-layer clouds. When looking at the results, it can be observed that there is a high scattering between single timestamps of all stations of the experimental setup. This scattering is mainly observed for larger cloud heights and leads to deviations inside the 15 min rolling means of all pairs. Nevertheless, the results are accurate for low-layer clouds. In general, OLCLE tends to overestimate, whereas station OLDIR tends to underestimate the CBH for this day. However, also the cleaned stations OLMED and OLUOL show similar results as the uncleaned

station OLDIR. Therefore, these deviations cannot be attributed to the cleaning state of the lenses. All the ASIs of the experimental setup have short distances to the station OLGBA, and as such are only well suited for the CBH estimation of low clouds. Therefore, these higher deviations are expected for high-layer and mid-layer clouds and do not necessarily correspond to the cleaning state of the camera.

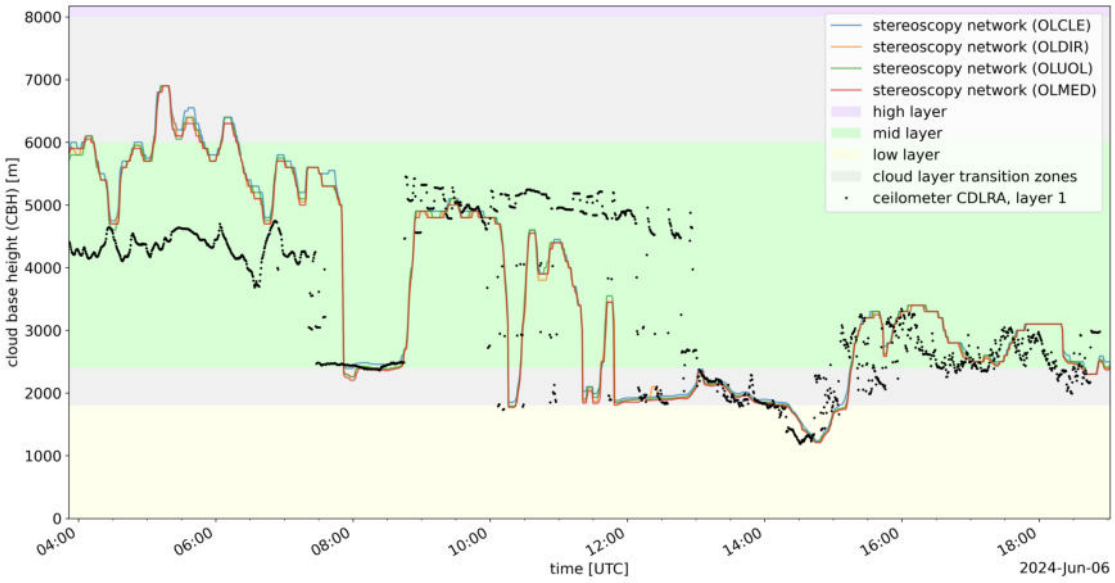

Figure 27: Comparison of global cloud base height results of WobaS for different network configurations and ceilometer measurements of station CDLRA, 6 June 2024.

In WobaS the CBH results of all selected ASI pairs are merged into one global CBH by applying a likelihood function according to the different distances between the camera as described in Blum [2]. This results in one CBH value for the entire network. Figure 27 shows the results of the global CBH for all network configurations for the day mentioned above. In contrast to the results of the individual ASI pairs, one can observe that for all configurations, the curve progression does not show high scattering between the timestamps. This means that the network makes the results less volatile. It can also be seen that the differences between the subnetwork configurations are small. Due to the high redundancy of cameras within the network, the influence of errors of individual ASI pairs on the network decision is limited. The general error of the CBH estimation of the network is greater than any influence of the different cleaning states of the cameras. For these reasons, no significant impact of continuous soiling of ASI lenses on the global network CBH results could be observed.

To investigate the influence of exposure time deviations, the Mobotix Q26B-6D cameras OLCLE and OLMED have been set to an exposure time of 147 µs during May 2025 (before it was 163 µs). This exposure time is closer to the real exposure time of the Mobotix Q25 cameras with 149 µs and therefore more comparable. Due to a failure of station OLUOL, only stations OLCLE, OLMED, and OLDIR have been used for the pairing with station OLGBA. OLGBA was out of service on May 20, 23 and 28 2025 so these days have not been considered for the comparison of the ASI pairs. ASI OLJET was dismantled in October 2024 and was therefore no longer part of the network in May 2025. Figure 28 shows the CBH error metrics of the individual ASI pairs and the global network on 1-24 June 2024 (exposure time of OLCLE and OLMED = 163 µs) and on 1-31 May 2025 (exposure time of OLCLE and OLMED = 147 µs).

It was expected that adapting the exposure times of the stations equipped with a Mobotix Q26B-6D would improve the performance of these stations. However, this cannot be observed in the error metrics. For the results of the individual ASI pairs (marked with x), almost all errors have worsened. Only the magnitude of the MBE of station OLCLE stayed almost the same, but the sign has changed, so OLCLE tends to overestimate the CBH with lower exposure time. The reason for general deterioration in the error metrics may be the absence of the far-distant camera OLJET or different weather conditions in June 2024 and May 2025. However, one can see that the MAE (Figure 28a), the RMSE (Figure 28c) and the rRMSE (Figure 28d) increase more for the stations OLCLE and OLMED than for station OLDIR. Therefore, contrary to the expectations, a deterioration can even be recognised due to the changed exposure times. For the results of the network configurations (marked with •), a deterioration of the error metrics can be observed for all subnetwork configurations. However, almost no differences can be observed between station OLDIR and the stations OLCLE and OLMED. It can be concluded that deviations in exposure times can have an impact on the CBH estimation of individual ASI pairs. Nevertheless, due to redundancy of ASIs within the network, the global CBH estimation of WobaS is resilient to exposure time deviations of single ASIs in the network.

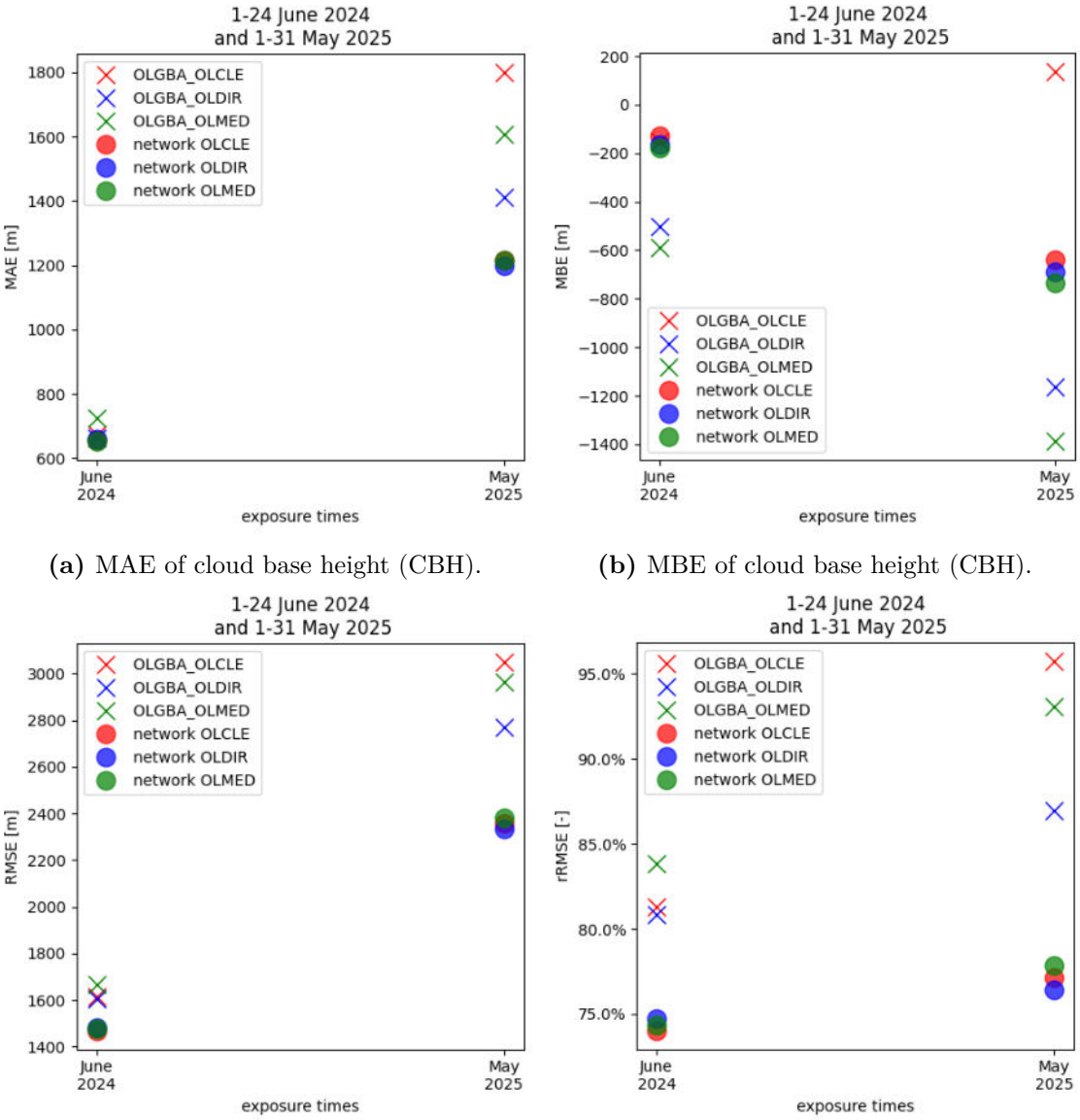

(a) MAE of cloud base height (CBH).

(b) MBE of cloud base height (CBH).

(c) RMSE of cloud base height (CBH).

(d) rRMSE of cloud base height (CBH).

Figure 28: Error analysis of cloud base height (CBH) estimations of WobaS on 1-24 June 2024 and on 1-31 May 2025 of stations OLCLE, OLMED and OLDIR; OLCLE and OLMED with changed exposure times (June 2024: 163 µs, May 2025: 147 µs), exposure time of OLDIR const.=149 µs.

4.3 Irradiance forecast analysis

The final results of WobaS are the irradiance forecast maps of the different irradiance components BNI and GHI. These forecast maps do have the spatial dimension (lat, lon), the temporal dimension of the forecast starting point (t) and the lead time dimension (lt). For the investigation of the impact of continuous soiling on the final forecast results, the maps have been analysed first in the spatial domain, and second in the temporal domain. For the investigation in the spatial domain, the forecast maps of uncleaned stations OLDIR have been compared with the forecasting maps of the cleaned reference station OLCLE, by subtracting the results and building difference maps. When using the uncleaned station OLCLE as references, the spatial MAE, MBE and the RMSE are calculated. For the investigation in the temporal domain, the forecast results for the location of the reference station OLWIN were extracted from the maps and compared with the time series observations of OLWIN. For the temporal analysis, it is expected that the error metrics of the cleaned stations OLCLE, OLMED and OLUOL are smaller than for the uncleaned station OLDIR. For the analysis of the impact of interfering objects, different examples of interferences were collected from the entire subnetwork. The forecast maps during these interferences were then compared with the results before and after the interference. In addition, the impact of these interferences is evaluated in the temporal domain by comparing the forecast results for the location OLWIN with the observations of OLWIN. The impact of localised soiling is analysed by comparing the irradiance forecast before and after the cleaning of the locally soiled station OLFLE on 20 June 2024.

Figure 29 shows the GHI maps for 15 June 2024 for both the subnetwork configuration with station OLCLE and with station OLDIR for the forecast point of t = 12:00 UTC and the lead times lt = 0 min, 5 min and 15 min. This example is chosen because during this time the cloud field showed a high spatial variability, which cannot be reliably predicted with other forecasting methods. Looking at the difference maps, one can observe that the network configuration with station OLCLE and the configuration with station OLDIR differ from each other. The error is highest at the points on the map with high gradients in the irradiance prediction. These points correspond to the borders of the clouds. One can see that these differences are symmetrical. Some edges do correspond to an overestimation, others to an underestimation of the results of station OLDIR. This behaviour can be described as a double penalty and leads to a relatively high RMSE, because the errors on the opposite edges are counted twice in the calculation of the overall error of the forecast. With increasing lead times, the differences between the two forecasts are becoming more and more pronounced. However, the low spatial MBE reveals that there is almost no bias in the results. Also, the spatial MAE shows that the dif-

ference between both forecasts is small when the outliers are not heavily weighted. The same behaviour can be observed when looking at the same maps for the BNI (see Appendix A Figure 46).

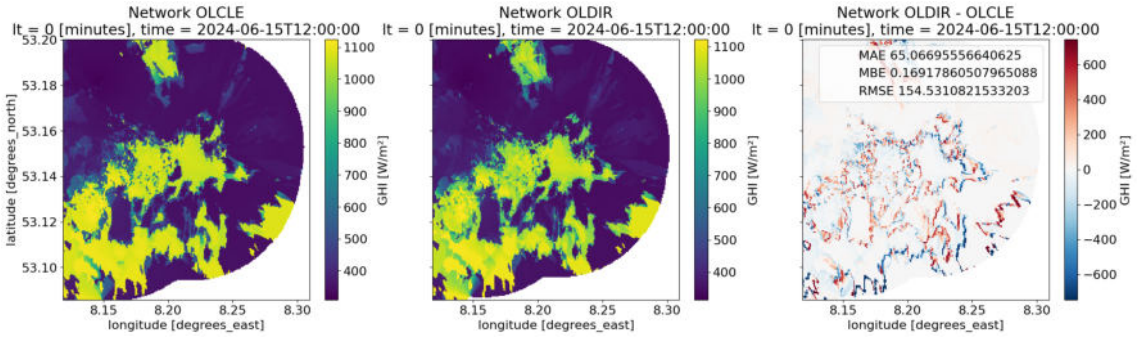

(a) Lead time 0 min

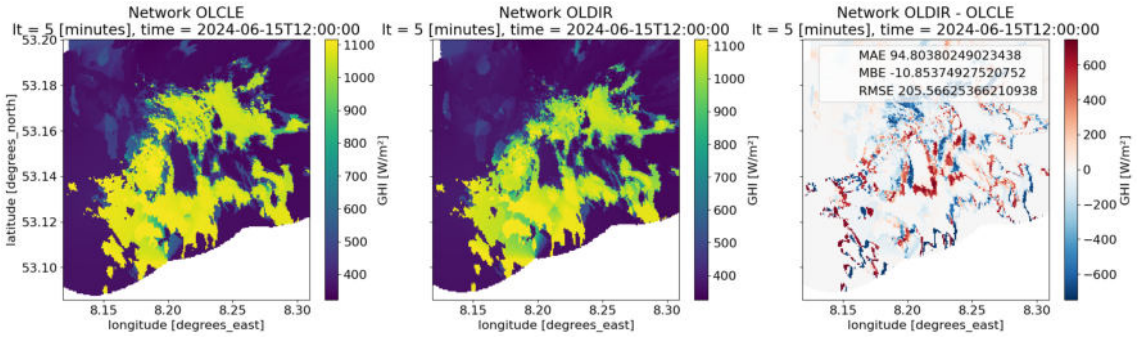

(b) Lead time 5 min

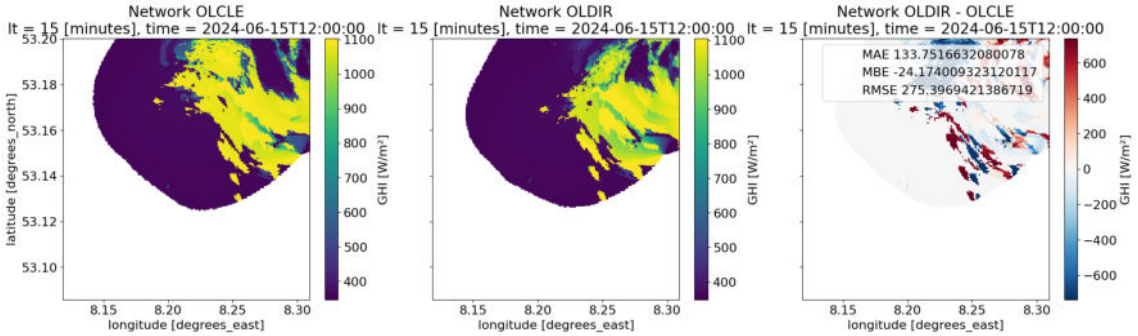

(c) Lead time 15 min

Figure 29: Global horizontal irradiance (GHI) results of full subnet configurations with reference camera OLCLE, camera OLDIR and difference maps of both results for lead times lt = 0 min (a), 5 min (b) and 15 min (c), calculated spatial mean absolute error (MAE), mean bias error (MBE) and root mean square error (RMSE), 15 June 2024.

These errors are projection errors, which occur during the merging process. They can be caused by little variation of the estimated CBH or by small errors in the camera calibration. Due to the absence of a ground truth for the maps, it is difficult to tell whether these variations are caused by soiling of the camera lenses.

Figure 30 shows the GHI results of WobaS for the location of station OLWIN and the reference observations for 26 June 2024, a day with mostly clear sky conditions and high-layer clouds. One can observe that the network results show no

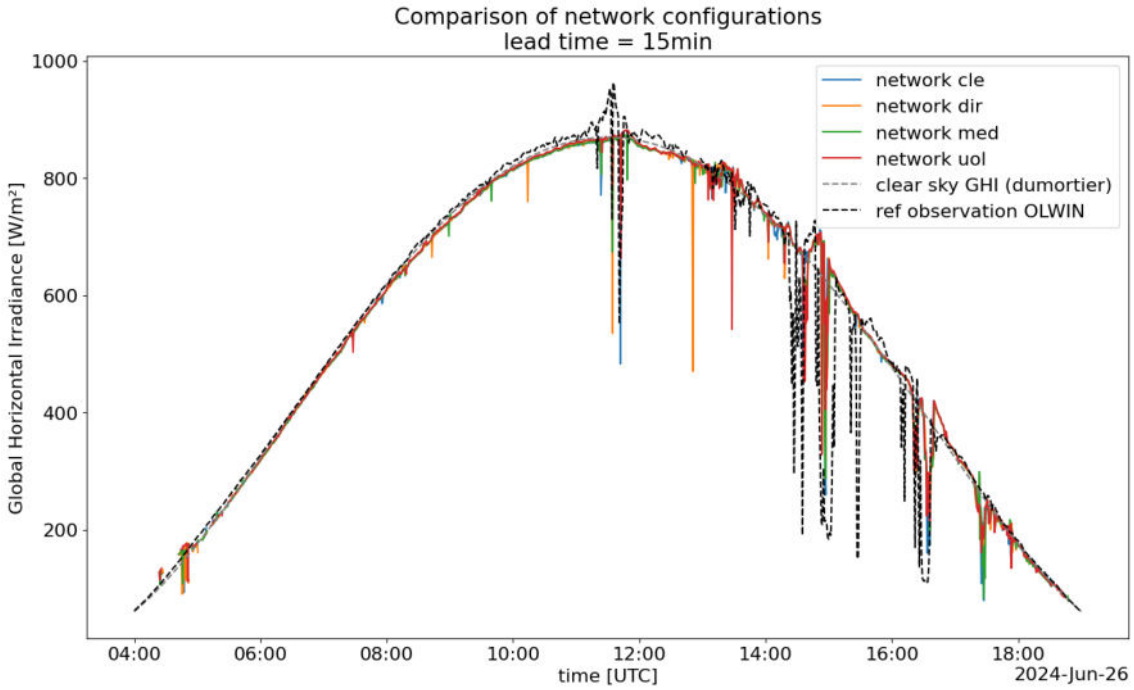

Figure 30: Global horizontal irradiance (GHI) irradiance forecast for location of station OLWIN compared to irradiance observations of station OLWIN, clear sky curve according to model of Dumortier [9], 26 June 2024

major deviations for this day. Only slight differences of the predicted irradiance between the different configurations can be observed. In Figure 31 the temporal error metrics for this day are calculated and plotted over the lead time together with the temporal coverage. Depending on the cloud speed and the CBH, the maximum forecast horizon may be shorter than the specified forecast horizon of 30 min. The temporal coverage is the highest for slow moving clouds, for high-layer clouds, and for clear sky conditions. However, the last two situations have little impact on the irradiance. This means that for low temporal coverage, the error metrics are less meaningful because these events are over-represented. For this reason, the error metrics are only expected to be meaningful for a temporal coverage of more than 25 %. It can be seen that the differences between the network configurations are small. The temporal MAE shows almost no deviations between the different network configurations. Looking at the RMSE one can observe that in some cases, the error of the network with the cleaned station OLCLE is even higher than the error of the uncleaned station OLDIR. One can also see that long lead times correspond to high errors. This matches the expectation for forecast tasks. Greater deviations from the observations are to be expected the further one looks in the future. Similar observations can be made for the results of the BNI (see Appendix A Figure 47).

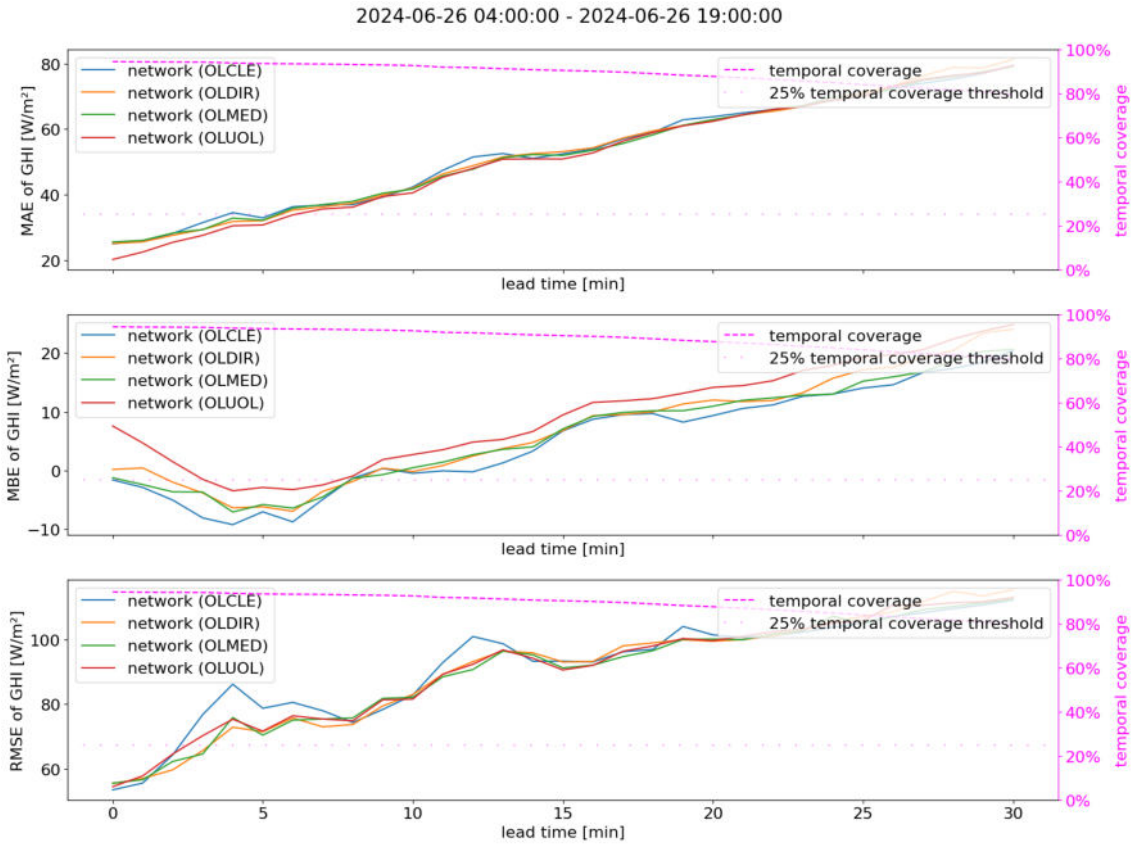

Figure 31: Mean absolute error (MAE), mean bias error (MBE) and root mean square error (RMSE) for global horizontal irradiance (GHI) for different network configurations with temporal coverage, 26 June 2024.

The same trend can be seen by looking at the GHI results of 6 June 2024, a day with variable weather situations, in Figure 32 (results for BNI can be found in Figure 48 in Appendix A). This day was chosen because there were variable cloud conditions. Also for this day, only slight differences of the predicted irradiance between the different configurations can be observed. There is also no clear tendency of the soiled ASI recognisable.

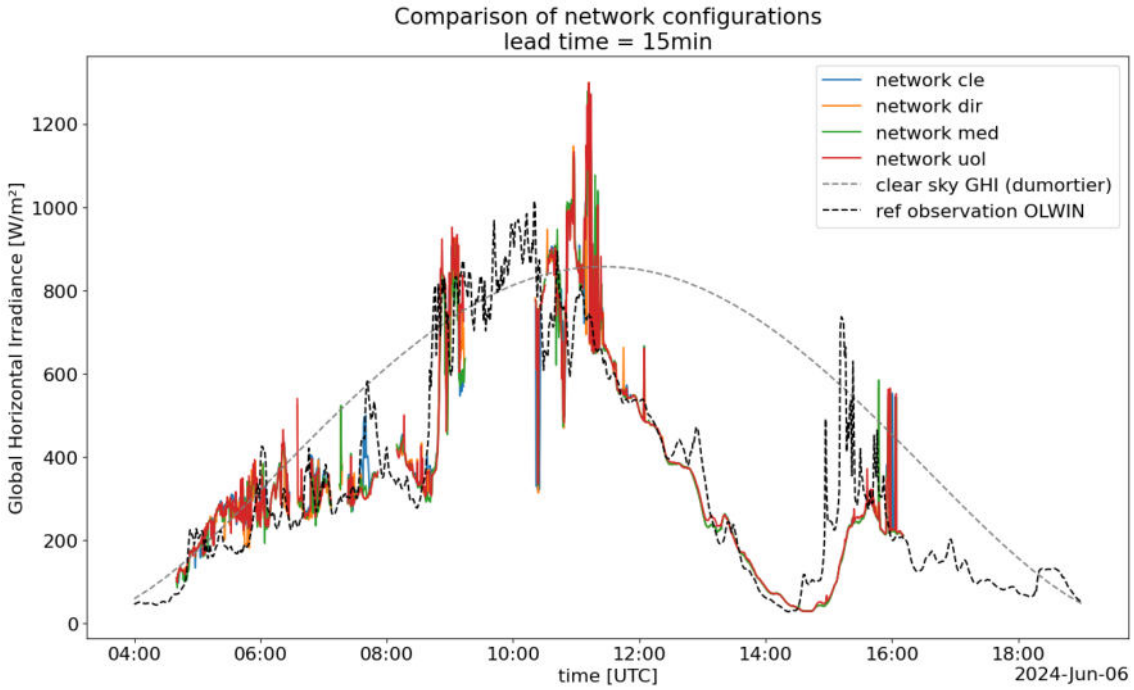

Figure 32: Global horizontal irradiance (GHI) irradiance forecast for location of station OLWIN compared to irradiance observations of station OLWIN, clear sky curve according to model of Dumortier [9], 6 June 2024

Looking at the error metrics in Figure 33, one can see that all error metrics are more pronounced than for the clear sky day. However, no big deviations between the different network configurations can be observed. The MAE and the RMSE follow a similar pattern as the previous analysed day. Contrary to the expectations, one can see that the MBE of station OLCLE is even higher than the MBE of station OLDIR for most of the lead times. For the MBE one can also observe a relative improvement for lead times in between 15 to 20 min. This could be caused by a drop in the temporal coverage and does not necessarily correspond to a better model behaviour.

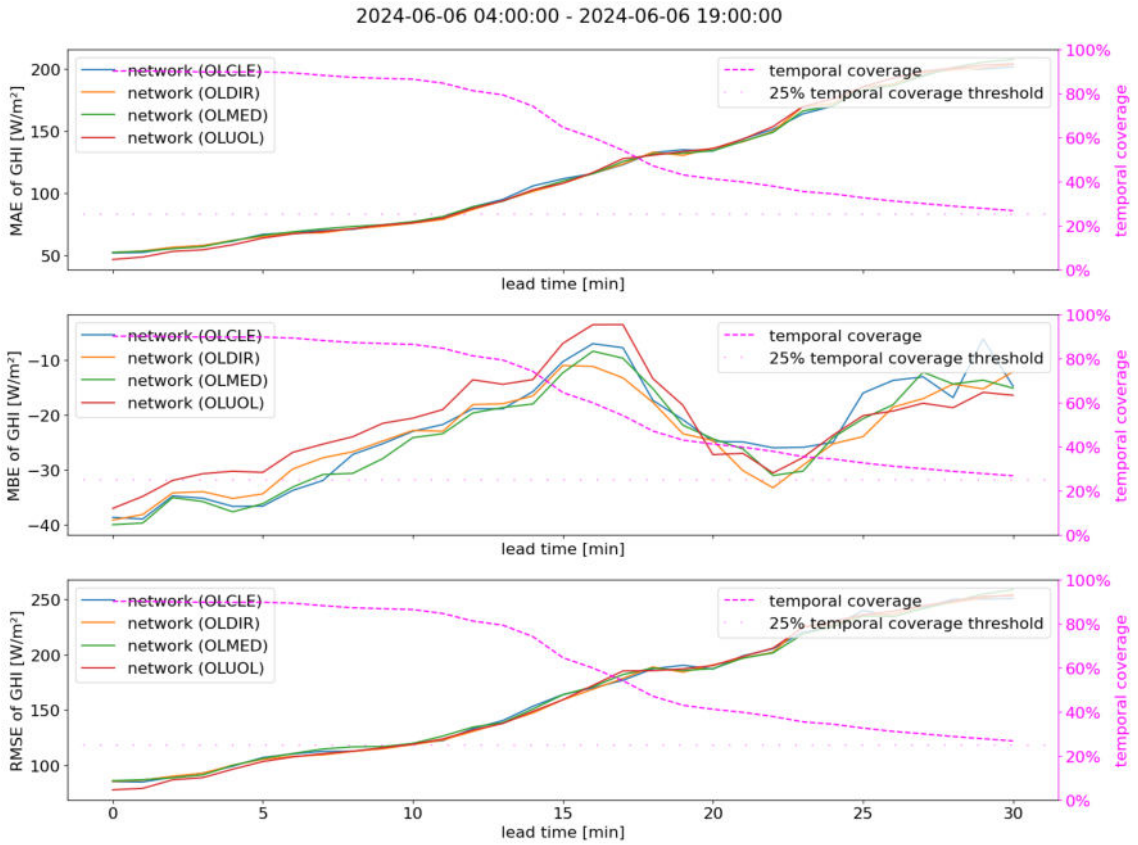

Figure 33: Mean absolute error (MAE), mean bias error (MBE) and root mean square error (RMSE) for global horizontal irradiance (GHI) for different network configurations with temporal coverage, 6 June 2024.

Despite the differences between the results of the different network configurations, no clear influence of continuous soiling could be observed. Due to the high redundancy of ASIs within the network. The errors of single cameras do not have a large impact on the final predictions and the forecasts.

For the analysis of the impact of interfering objects on the irradiance forecast maps, the forecast maps were analysed in the spatial domain by comparing the results of the lead times (lt) = 0 min and 15 min for the forecast times before and after the main interference. The effect of interferences is expected to be made visible in this way. In Figure 34 one can see the BNI forecast results on 14 June 2025 during an interference of a bird at station OLGBA. The bird was blocking parts of the lens.

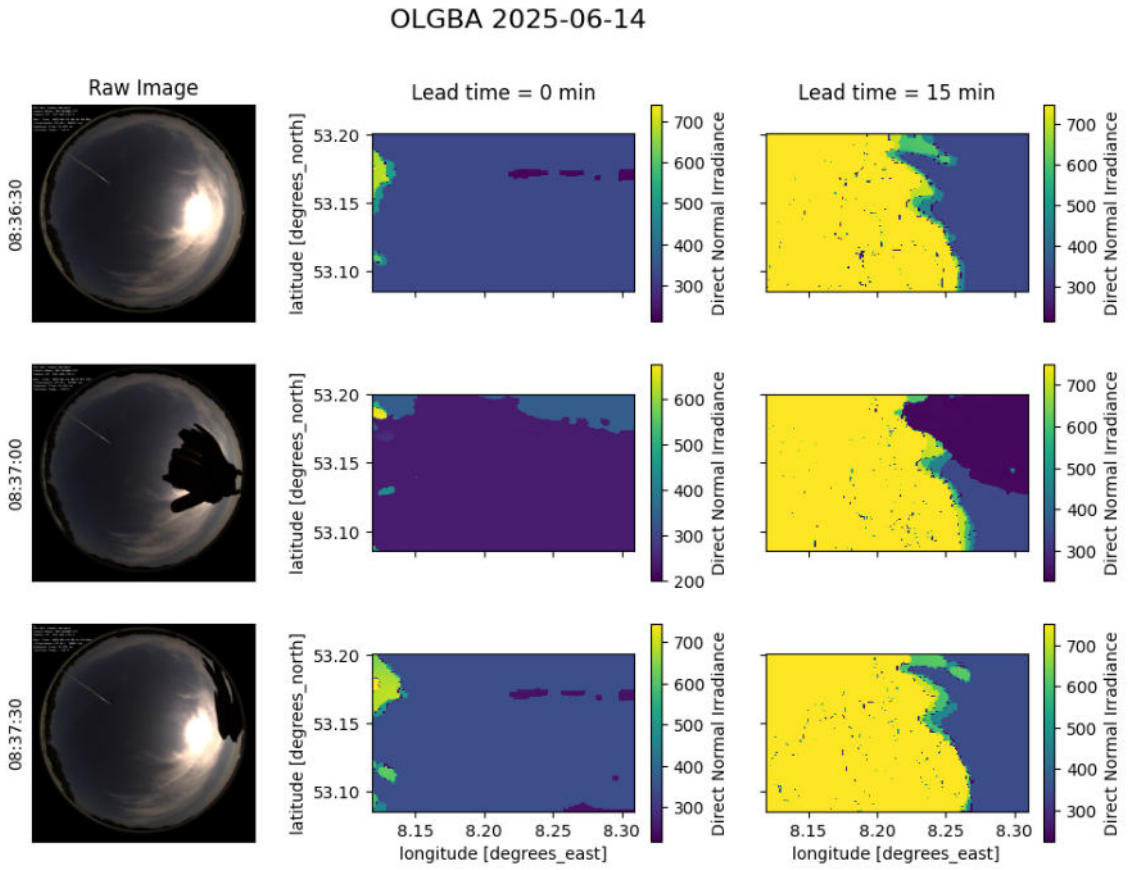

Figure 34: Beam (direct) normal irradiance (BNI) forecast results during bird interference for lead times 0 min and 15 min, 14 June 2025.

By comparing the results during the main interference at 08:37 UTC with the forecast results before and after the main interferences, one can see that a significant drop in BNI is predicted for almost the entire spatial domain. However, both the forecasts before and after the interference do not predict this drop of BNI. By looking at the results for lead time lt = 15 min, it can be seen that this drop not only affects the prediction of lt = 0 min but is moved in the direction of the general cloud motion and, therefore, also affects the forecast for longer lead times. This can also be seen by evaluating the forecast results at the location of the reference station OLWIN.

Figure 35 shows the prediction of the BNI at the location of station OLWIN in comparison to the predictions of lead time lt = 0 min and the observations of station OLWIN for the three forecast points shown above.

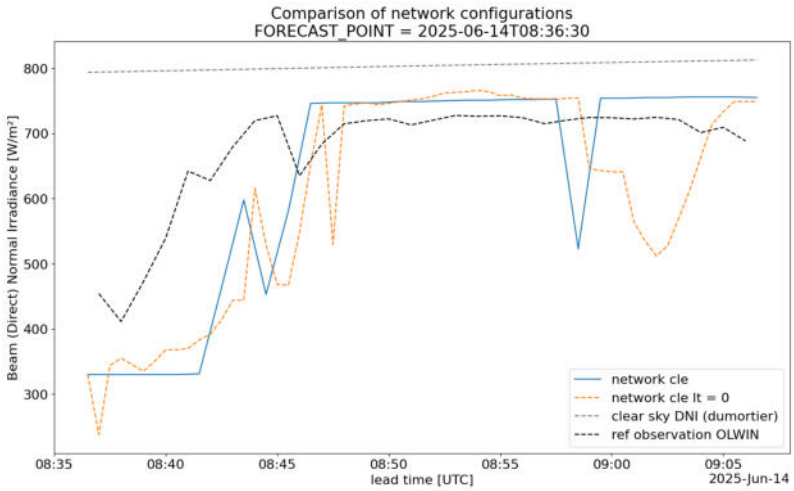

(a) Before main interference

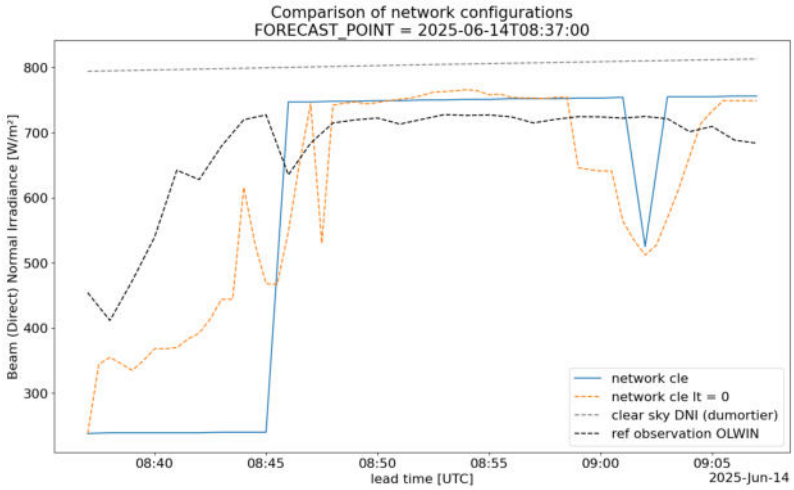

(b) During main interference

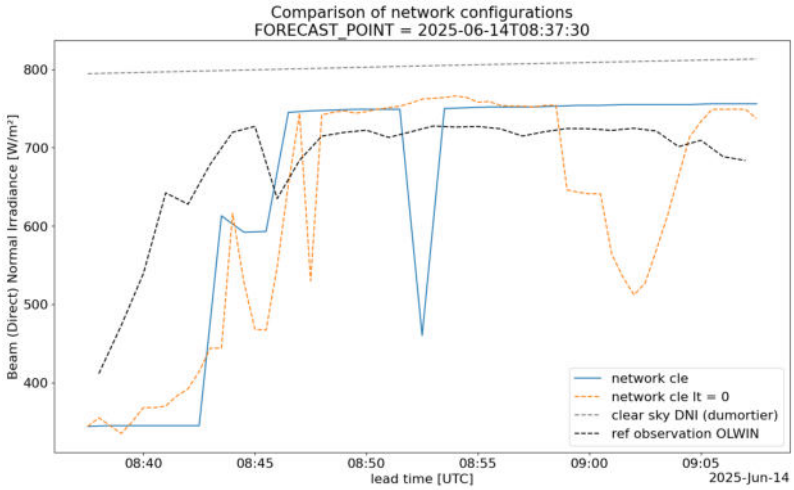

(c) After main interference

Figure 35: BNI forecast results for station OWLIN over lead time, for forecasts points before, during and after main interference by bird compared with BNI observations of reference station OLWIN and the predictions for lt = 0 min, clear sky curve according to model of Dumortier [9], 14 June 2024 08:37 - 9:07 UTC.

In Figure 35a and Figure 35c, one can see that the increase of the BNI during the first minutes of the forecast, like shown in the observations of OLWIN, is also predicted at the timestamps before and after the main interference with only a delay of about 5 min. However, in Figure 35 one can see that the increase of the BNI is only predicted after 8 min with a sudden surge in the BNI. This leads to the conclusion that interferences on single ASIs can also have an impact on the forecast results for other locations inside the spatial forecast domain, also for short lead times. Although the total difference in the BNI for this example is relatively small, such behaviour during large-scale ramp events could be critical, because in these situations a precise forecast of the exact time of occurrence is important.

Another example of interference caused by a bird can be seen in Figure 36. In this case the interference lasted longer than only one time stamp, so the bird was captured multiple times. When looking at the raw image of the time stamp 04:47 UTC, before the interference, no clouds can be observed. However, the predictions made for this time stamp show areas with small BNI on the map. The reason for this could be the small elevation angle of the Sun. These forecast errors may be caused by wrong boundary masks of single ASIs in the network. Objects of the surroundings, like the antennas seen in the image of station OLDON, may incorrectly be classified as clouds. This could lead to the appearance of such artefacts. Looking at the timestamps 04:47:30 UTC and 04:48:00 UTC, during the interference, one can observe a decrease in irradiance for a large area inside the spatial forecast domain caused by the interference. This effect cannot be observed during the timestamps 04:48:30 UTC and 04:49:00 UTC. By looking at the different forecasts results for lead time $\mathrm{lt} = 15$ min (on the right of the image), not only can be seen that the bird interference causes an attenuation of the predicted BNI for longer lead times, also the cloud motion is affected by the interference event. The movements of the bird may lead to incorrect predictions of the CMVs and therefore to a wrong estimation of the motion of the cloud field for longer lead times.

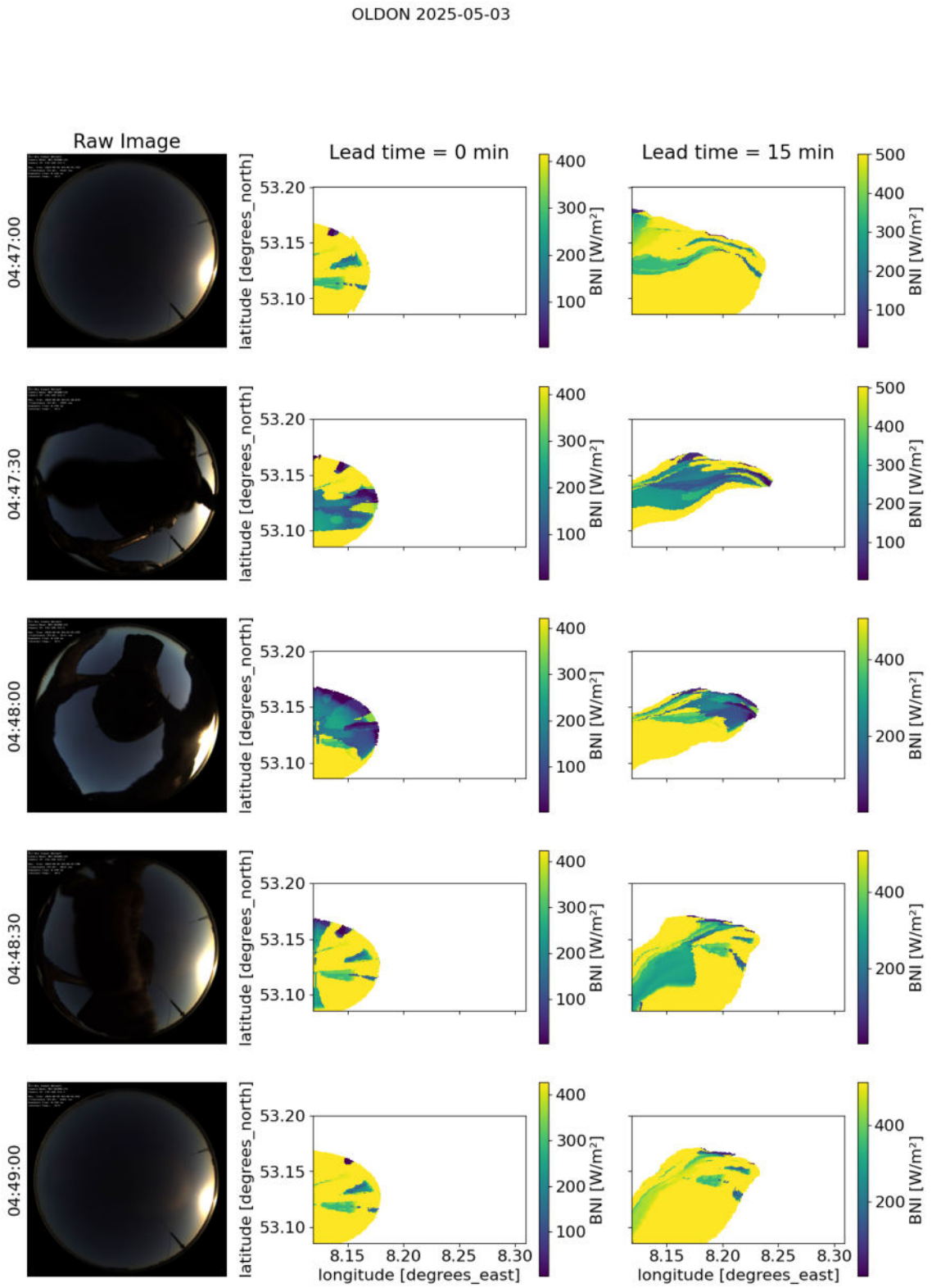

Figure 36: Impact of bird interference at station OLDON on cloud motion results, 3 May 2025.

For the investigation of the impact of localised soiling on the irradiance forecasts of WobaS, the results of the locally soiled station OLFLE were compared before and after the cleaning of the station. Figure 37 shows the BNI results of station OLFLE on 20 June 2024 before and after the cleaning event. When looking at the raw images of station OLFLE at the timestamps 06:33:00 UTC and 06:40:00 UTC, one can see that small dirt stains covered the top and the left side of the lens. Looking at the predictions for lead time lt = 0 min one can see that these dirt stains do lead to very small artefacts in the centre of the irradiance forecast maps (dark spots on the map). These artefacts cannot be observed in the forecast of time stamp 06:47 UTC, after the cleaning event. However, the spatial extent of these artefacts is very small and they only have a minor influence on the forecasts maps for lead time lt = 15 min for the time stamps before the cleaning events. From this it can be concluded that small localised soiling has little impact on the irradiance forecast of WobaS.

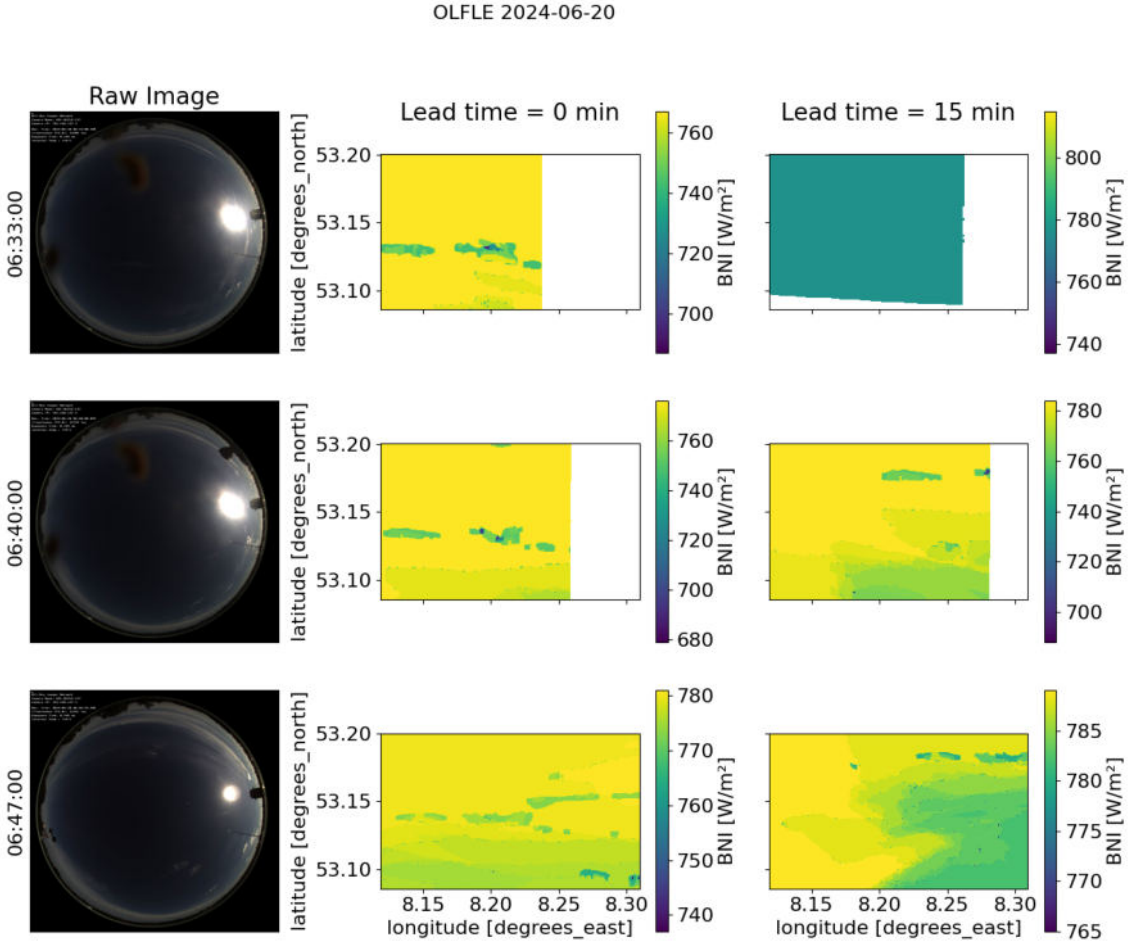

Figure 37: Impact of localised soiling on beam (direct) normal irradiance (BNI) forecast of WobaS, results of locally soiled station OLFLE before and after cleaning event, 20 June 2024.

5 Further developments of Eye2Sky

Based on the findings of this thesis, different quality control methods have been developed. These methods address two main aspects of quality control. The first objective is to detect and label bad input data and results. The second objective is to derive automatic recommendations for maintenance actions based on the current state of the systems within the network. For real-time operation of an ASI-network, maintenance costs could be a limiting factor, so the goal should always be to minimise these efforts. In the following, these methods are described in more detail.

5.1 Soiling monitoring

As shown in subsection 1.2, lens soiling can have several forms. This makes it difficult to classify any type of soiling in terms of its severity. For this reason, a monitoring method has been developed to better quantify and compare the status of lenses of the ASIs in the Eye2Sky network. This monitoring can help improve the planning of maintenance visits. The method is based on the idea that the state of the lenses is highly dependent on the last maintenance/cleaning time of the camera. The greater the differences in the image data of a camera compared to the image data of the reference camera, the greater the soiling of that camera. In this thesis, the regularly cleaned station ASI OLCLE is used as a reference for a clean camera (see logbook in Appendix A Figure 49).

Images from the same timestamp cannot be directly compared because the current cloud field is observed from different view angles and the weather situation may vary between camera locations, especially for far distant cameras. To filter out all non-persistent phenomena and short-term fluctuations inside the images caused by the current weather, all images of one station are averaged by calculating the mean value of each pixel for a given time period. Red-green-blue additive colour model (RGB) daily mean-images are a side product of the image masking procedure of surrounding obstacles. To save processing time, these daily mean-images are used to average also larger time scales. The mean-images can be built for any time period, but for this work one-week rolling intervals are chosen. By calculating the mean-images, non-static events like cloud motion are averaged out, but persistent phenomena like lens degradation or persistent soiling are strongly reflected in the mean-images. To reduce complexity, the channel information of the RGB mean-images is translated into one-channel greyscale images. These greyscale-images are created using the OpenCV-convention (see [22]). By creating histograms of the pixel values of images, it can be observed that different cameras appear to have offsets in their pixel value distributions (see Figure 38a). This could be e.g. due to small environmental differences in the brightness of the surrounding or to slight

deviations in the sensitivity of the camera chips or in exposure times as described in subsection 3.4. In order to keep the images comparable, images are preprocessed by z-standardising the whole image array. (see Figure 38b).

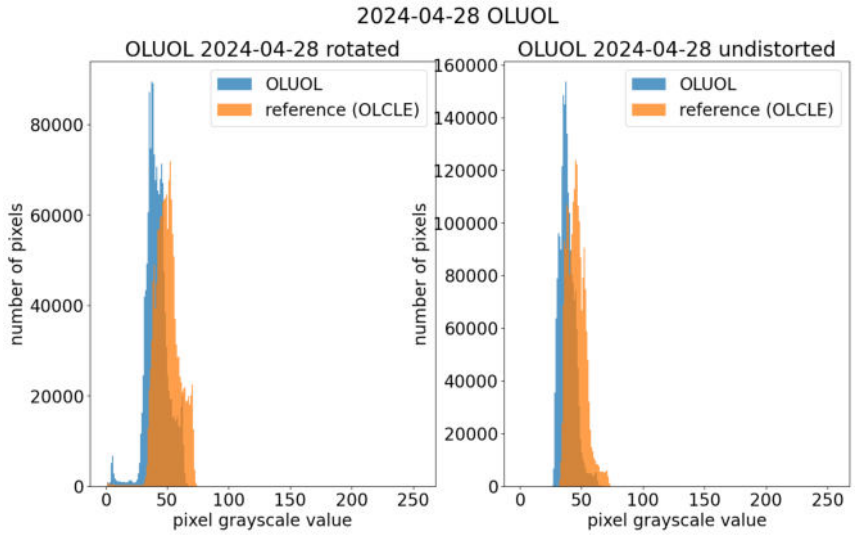

(a) no standardisation

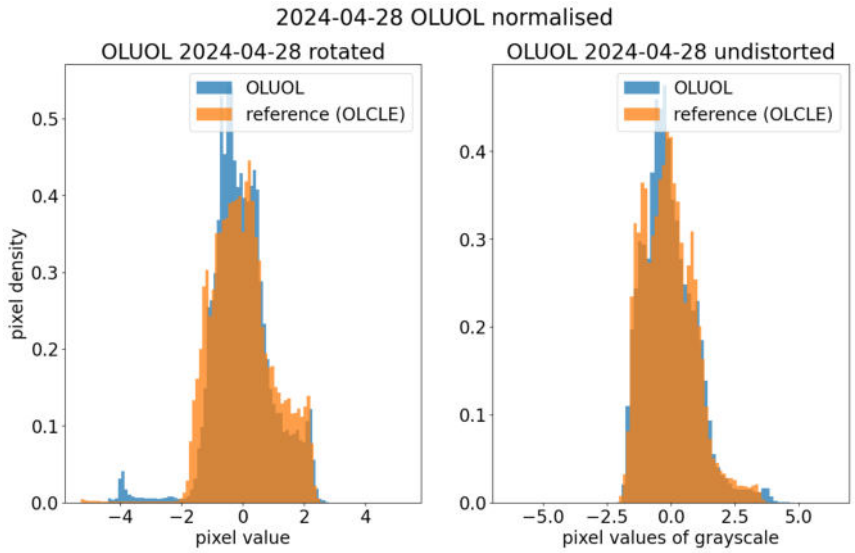

(b) z-standardised

Figure 38: Distribution of one-byte pixel values of greyscale daily mean images of all-sky imager (ASI) OLUOL compared to ASI OLCLE for distorted and undistorted images, 28 April 2024.

After standardisation, the image arrays are subtracted to create a difference-image. Figure 39 shows an evaluation plot with the differences image of the localised station OLFLE for the rolling mean of the previous seven days before 9 June 2024.

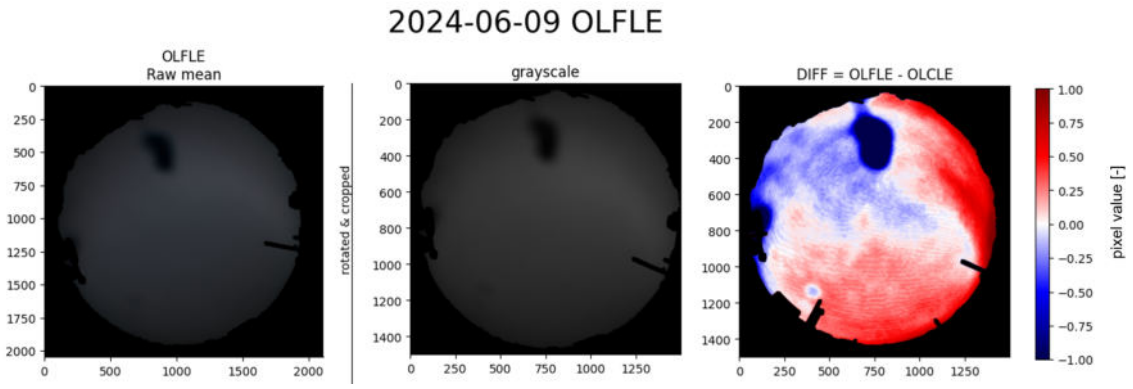

Figure 39: Evaluation plot of soiling monitoring method for locally soiled station OLFLE, averaging of previous 7 days, FLTR: raw mean-image of station OLFLE, greyscale-image (rotated), difference-image of standardised greyscale images (OLCLE as reference), and comparisons to difference image from previous day, 9 June 2024.

Differences in the amount of valid pixel per image due to different masks of surrounding obstacles are assumed to be negligible, because the amount of pixels within the border mask is comparable for all stations. To finally obtain a single soiling value SV for each ASI, the RMSE is calculated for the resulting difference-image. This value can be visualised over time to receive monitoring of the current state of the lenses for all long-term soiling and degradation (see Figure 40). This whole process can be summarised by Equation 13:

$$SV_{RMSE} = \sqrt{\frac{1}{n_{pix}} \sum_{i=1}^{n_{pix}} \left(\frac{v_i - \mu}{\sigma} - \frac{v_{\mathrm{ref},i} - \mu_{\mathrm{ref}}}{\sigma_{\mathrm{ref}}}\right)^2} \tag{13}$$

n_{pix} = const. equals the number of pixels in one image, v_i equals the one-byte value of pixel i in the averaged greyscale image $\in [0 - 255]$ (integer) or $[0 - 1]$ (float), μ equals the mean value of all v_i in one image and σ equals the standard deviation of all v_i in one image. The suffix $_{\mathrm{ref}}$ indicates the aforementioned parameters for the reference image.

This method can be used to map all long term changes, independently of the type of contamination (locally or continuous), because it only takes into account the overall differences between the clean and the dirty image. However, short-term events like birds or insects cannot be detected because they get averaged out. Both the distorted and undistorted images can be used as input, which leads to an indirect weighting of the pixels depending on their position due to the transformation. This method is expected to work only if the locations of the ASIs are close to each other, so that both systems are exposed to comparable weather conditions during the averaging intervals. For far distant ASIs the environmental conditions can differ greatly, so the comparison is expected to work the best for short distances. Looking at the soiling monitoring plot of the first half of 2024 in Figure 40 one can observe

that station PAPEN ($\approx 55\,\text{km}$ away) shows more differences to station OLCLE than other uncleaned stations in Oldenburg. Nevertheless, when looking at the nearby cameras inside the domain of Oldenburg city, the results are plausible. One can also see that, for regularly cleaned stations OLGBA and OLUOL as well as for the daily automatically cleaned station OLMED the values stay low. Also, the localised soiling event of station OLFLE in May 2024 and the following cleaning session in June 2024 have been detected correctly. However, by comparing the cleaned station OLUOL with station OLCLE it can be seen that both stations seem to have a small offset. This could be caused by the small deviations in the exposure times of both stations described in subsection 3.4. Despite the standardisation of the images, these differences may still have a small influence on the results. It can also be observed that the differences between the cleaned and uncleaned cameras are bigger in the summer months than in the winter months. From these results it can be concluded that this method requires a minimum brightness of the images in order to function reliably.

In Eye2Sky this method will be used to monitor the overall soiling state of the entire network. By introducing a threshold, an automatic warning system can be implemented. If the differences between cameras are getting big, a recommendation to clean the station will automatically be given. Moreover, it can be used to evaluate the amount of maintenance and schedule upcoming maintenance visits. The main advantage of this simple statistic approach is that it does not require any model training and can be directly implemented into any given network. Another advantage is that it can detect a variety of impacting factors, as it only focusses on the overall differences to the reference. One huge disadvantage is that such a reference is always required. However, this reference does not necessarily need to be one fixed station. It could also be determined dynamically by choosing a station based on the last cleaning times. Another disadvantage is that this method cannot classify the causes of the image differences and it only works for persistent phenomena. Short-term events, like interfering objects, cannot be detected. In addition, due to the long averaging periods, the method is insensitive to sudden soiling events, as these can only be detected after a few days.

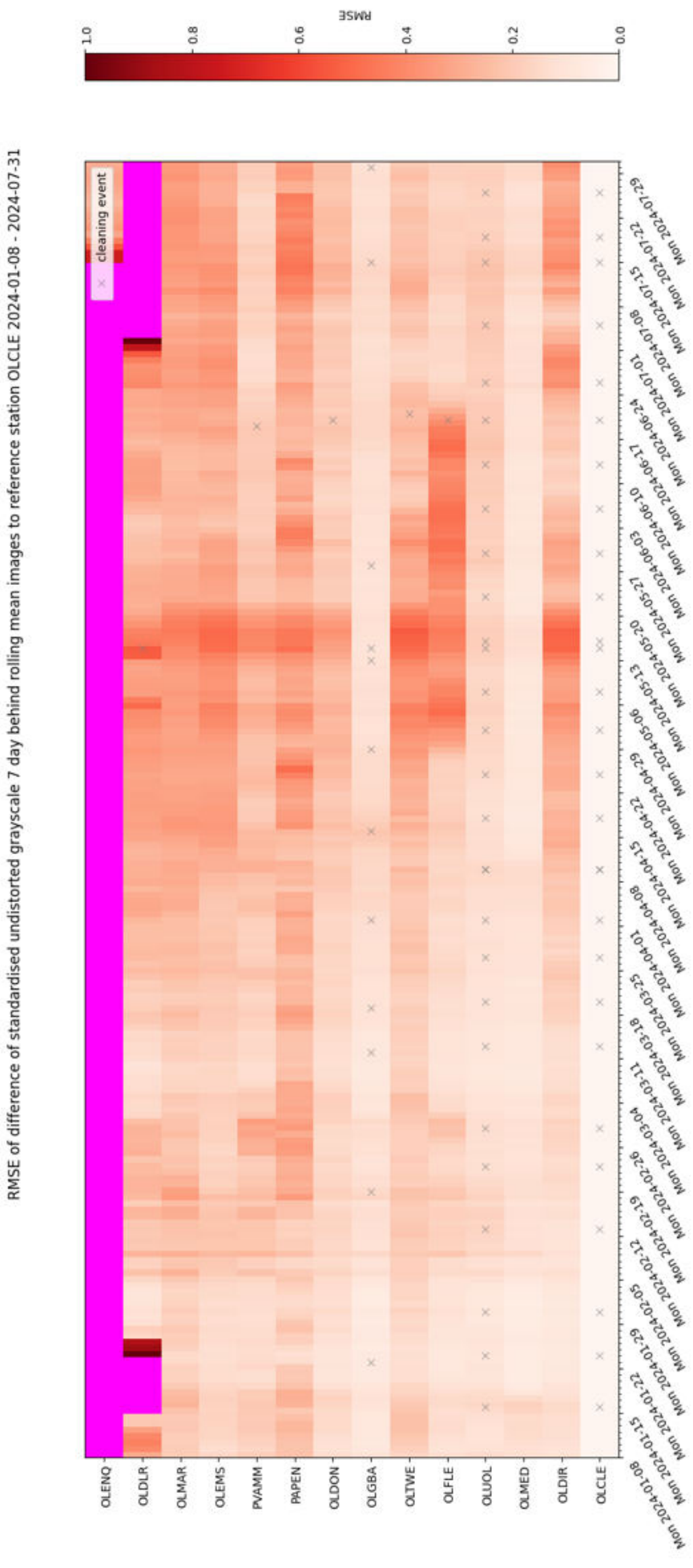

Figure 40: Soiling monitoring for selection of Eye2Sky stations for the first half of 2024, x-axis corresponds to the given date, y-axis corresponds to the station name, the colour dimension corresponds to the soiling value [pixel value] (root mean square error (RMSE) of standardised mean-images pixel values of given station in comparison to station OLCLE) and cleaning events from logbook.

5.2 Automatic detection of interfering objects (BirdDB)

Even though the effect of interfering objects in an ASI network remains small due to the redundancy of camera, for smaller ASI networks or single ASI systems, interfering objects pose a big challenge in ASI forecasting as they do not correspond to any malfunction of the system itself but just a problem of the image content. They are external factors which can hardly be predicted or prevented. However, recognition of these events can help to improve forecast quality by filtering effected images or flagging forecast results with warnings. This could be achieved with image recognition algorithms or threshold based filters. For training of e.g. supervised ML models or for validation of other QC algorithms, a database of real live examples is useful. The cameras used in Eye2Sky are commercial surveillance cameras of the company MOBOTIX AG and have an in-built image analysis sensor, the so-called 'MxActivitySensor', which can be used to detect motion inside the live image of the cameras [17]. In the context of surveillance, this sensor is used for the reduction of false alarms by detecting only the motion of relevant subjects in the live image without taking into account irrelevant continuous movements like shadows or trees.

For this thesis, the 'MxActivitySensor' has been repurposed and tested for the real-time detection of interfering objects in the context of ASI-image capturing. To accomplish this objective, the cameras of the network have been reconfigured to automatically build up an image database of interfering objects called BirdDB. If a motion is detected, the sensor can trigger an automatic image upload via file transfer protocol (FTP) in-between the regular image capturing interval of 30 s. The exact timestamps of the events are logged as well. The advantage of using this in-built method of the cameras is that no further image processing is needed. This can be helpful for speeding up QC in very short-term live nowcasting. However, the sensor does not provide any information about the type of interference, but image recognition algorithm could be trained on the output data to get a classification. In Figure 41, some examples of the output of BirdDB are given.

BirdDB cannot only be used to detect interfering objects, it can also be used to shoo away potential troublemakers. Every ASI in the network is equipped with an integrated speaker. If a motion event is triggered by the camera, the affected station automatically starts an audio alarm. In addition to this acoustic feedback, the stations equipped with an automatic cleaning system have been coupled with BirdDB. If an event is triggered, the stations can be set to start spraying water on the lenses. This can also shoo away the disturber.

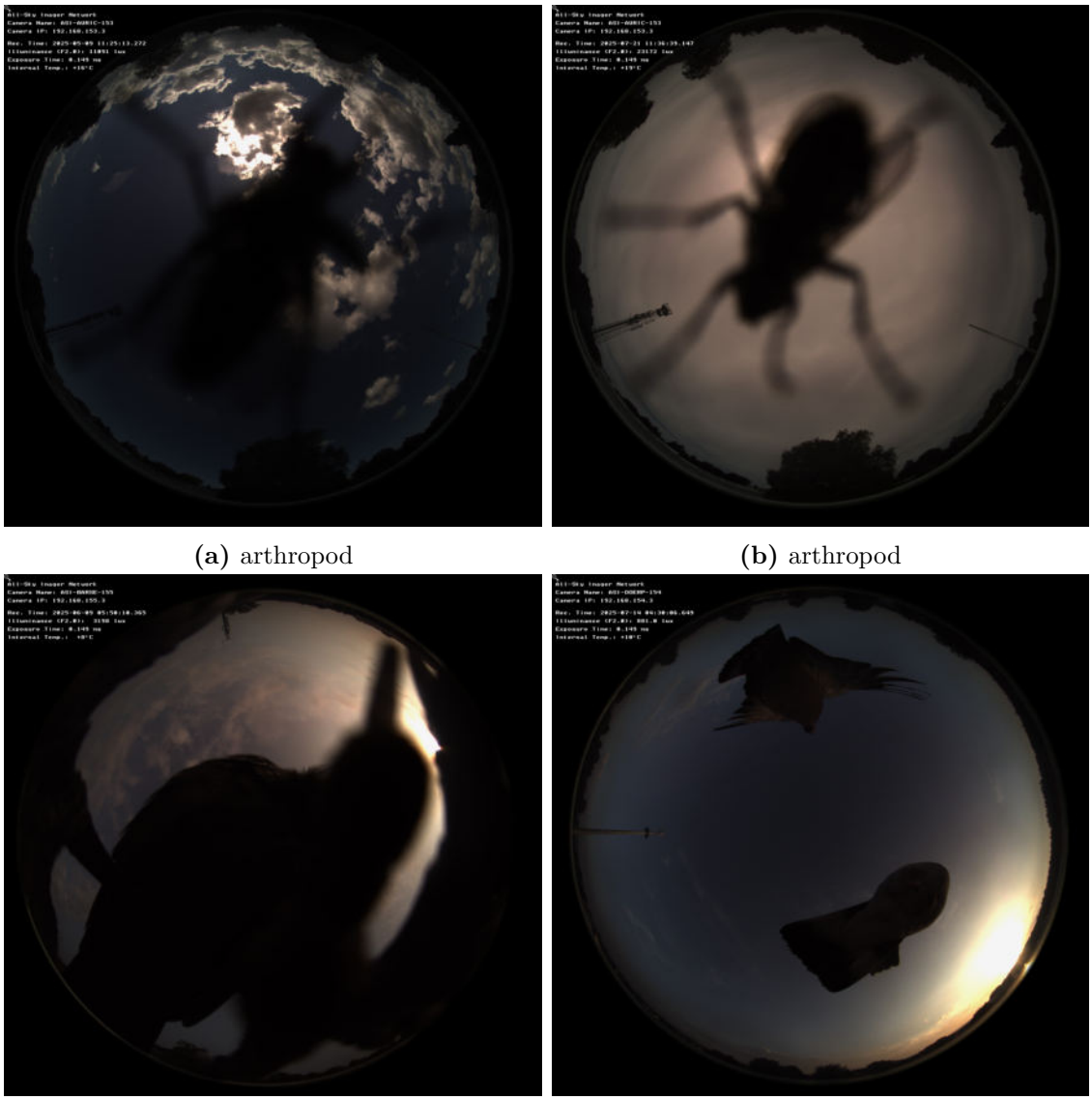

(a) arthropod **(b)** arthropod

(c) bird **(d)** birds

Figure 41: Examples of BirdDB database

To test the potential of BirdDB, a series of drone test flights was carried out at building A of DLR - VE. The aim of these tests was to see whether this simple native motion detection can be used to also detect acts of sabotage or surveillance by drones and it only served as a proof of concept. These tests showed that the motion detection sensor is also capable of detecting drone activities. Operators of ASI networks at locations of critical energy infrastructure could therefore also use the installed ASIs to monitor such activities. Figure 42 shows an example of a drone detection.

Figure 42: Drone detected by the motion detection sensor of the Mobotix all-sky imager (ASI) above building A of German Aerospace Center - Institute of Networked Energy Systems.

Another advantage of BirdDB is that the log of the detected events can be used to visualise the amount of interferences and the exact times at which they occur. This information can be used to create a real-time monitoring. Figure 43 shows an example monitoring of interferences for the current year 2025. In the period shown, 10 301 interference events have been detected by BirdDB. In the same period, a total of 16 545 484 images were captured by all cameras within the network. Interferences can also occur in between the regular image capturing intervals of the network (every 30 s), but even if one assumes that all interferences occurred during

image capturing, still only 0.06 % of all images would be affected. Monitoring these interferences can help determine the exact times of the days when interferences occur most frequently. The histogram in Figure 43 shows the number of events detected per time of day. One can see that most events are detected around noon. This is also the time where human interference, i.e. caused by maintenance, is expected to be the highest. However, a smaller peak in the distribution can also be observed during dawn, which may correlate with higher bird activity in the morning hours. Longer periods of observation are required to make reliable statements, but on the basis of such analyses, measures can be taken to minimise the amount of interference events within the network.

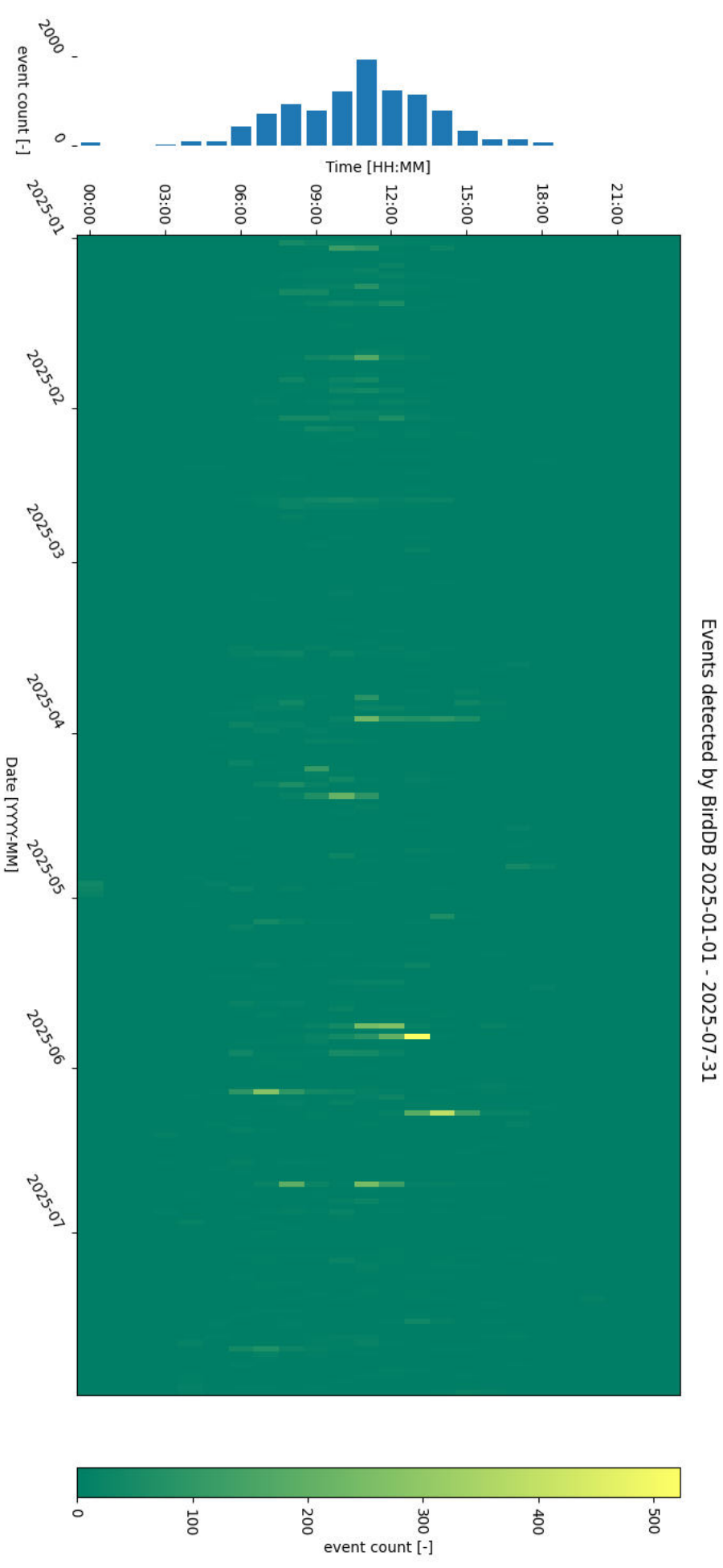

Figure 43: Amount of detected interferences of BirdDB form January till July 2025 (binned hourly), and histogram of detected events per time of day.

6 Conclusion & Outlook

In this thesis, the impact of image errors on the interim and final results of the irradiance forecast algorithm WobaS was analysed. The main focus was on the modules of cloud mask creation, CBH estimation, and the resulting irradiance forecasts. Based on these findings, different methods for the detection of image errors were developed.

For the cloud mask creation, the semantic segmentation algorithm of Fabel et al. [14] was used. Continuous soiling only has a minor impact on the segmentation results of the algorithm. Only under special weather conditions an influence of continuous soiling was observed. Soiling leads to a blurring effect which can lead to a misclassification of high-layer clouds as clear sky. In the image, atmospheric conditions with high turbidity can have optical properties similar to continuous soiling of the lens with high-layer clouds. This misclassification can be explained by differences between the location of the Eye2Sky network and Almería, Spain, where the training data for the model was recorded. Both locations differ considerably in their average aerosol concentrations, which can lead to different turbidities in the atmosphere. In the north-west of Germany, clear-sky conditions with high turbidity are rare. By transferring the model directly to Eye2Sky, for clear-sky conditions, the training data is not fully representative. However, this misclassification has no large impact on the irradiance results. The error analysis of the semantic segmentation module has also shown that the results of station OLMED, equipped with the automatic cleaning system, were comparable to those of the manually cleaned station OLCLE. This means that an automatic cleaning system can be used to reduce the maintenance effort of ASI networks.

Differences in the segmentation results for mid-layer and low-layer clouds were observed but could not be linked to the cleaning state of the lenses. However, it was found that the segmentation algorithm is sensitive to interference events and localised soiling. Both errors can lead to misclassification of the different cloud types. Although, the model is able to detect dirty or blocked parts of the image as invalid for some situations, in many cases this filter does not work. The model was never trained to reliably detect these errors. This model behaviour is not intentional and can also backfire in the form of misclassification of valid cloud situations like dark thunderstorm clouds as shown in subsection 3.3.

To avoid the classification of dark clouds as invalid, a filter could be introduced to the model that forces a valid cloud segmentation inside the border mask, but this would also affect the beneficial classification of interfering objects as invalid, therefore, it is not clear whether such a filter would improve the overall model performance. In addition, a pre-trained ML image detection algorithm could be

implemented in the processing chain of WobaS to filter the image input data. Another approach to improve the model is to introduce more examples of the critical situations mentioned above in the algorithm training data. This could be achieved by collecting examples for clear-sky and dark thunderstorm clouds from Eye2Sky and manually creating the cloud masks. These masks can serve as ground truths for the machine learning process and can be used to train a new model or fine-tune the existing model for the location of Oldenburg.

The analysis of the CBH estimations has shown that the cloud height results of single ASI pairs can differ greatly between cameras at the same location, as well as between timestamps of the same cameras. However, the error of the CBH estimation is mainly influenced by the distances between the cameras due to the different view angles on the clouds. These effects largely overshadow the effect of the analysed image errors. The high scattering in the results could not be clearly attributed to either soiling or deviations in exposure times. The assumption that the calibration errors of all cameras are negligible could be wrong. Slight deviations in camera orientations do have an impact on the CBH estimation and could lead to the observed behaviour. Consequently, more research is needed on the impact of camera calibration errors. However, when taking into account the full subnetwork configurations, only little deviations could be observed. This means that the impact of single cameras on the full network CBH estimation is small. Due to the redundancy of the ASIs, only slight deviations of the network CBH could be observed. Also, the error of the global network CBH was small for all cloud layers. From this it can be concluded that the CBH estimation profits from the multi-camera approach.

The final forecast results of the different network configurations revealed that the impact of continuous soiling on the forecast results is small. Spatial errors in the irradiance map forecasts did not affect the total amount of predicted irradiance. Only at the borders of cloud shadows, differences between forecasts could be observed. This effect could not be clearly attributed to soiling because it also appeared in between cleaned cameras. The spatial bias error was small, so the model mostly had problems in detecting the exact edges of the cloud shadows. This type of error could be caused by the shadow projection and the merging process in WobaS. Slight differences of the calibration of the camera and the estimated CBH could have an impact on the shadow mapping process. Also, the cameras of the experimental setup are not located at the exact same position ($\approx 2\,\mathrm{m} - 3\,\mathrm{m}$ difference). The distances between these cameras have been assumed to be negligible, but it could be possible that even small deviations of the position of the camera have an impact on the forecast results. Further investigation is needed to analyse the effect of these small calibration errors on the final network results.

In contrast to continuous soiling, an impact of interfering objects on the irradiance forecasts could be observed. Especially for areas inside the map with a low redundancy of ASIs, interfering objects could lead to drops in the forecasted BNI and the resulting GHI. However, for areas with high camera density, a significant influence of interfering objects on the results could not be observed. This leads to the conclusion that a dense ASI network is more resilient to short-term interferences than smaller network configurations or single ASI systems.

In section 5, different methods for the detection and the prevention of errors have been presented. The implemented soiling monitoring has shown, that it is possible to reliably detect continuous and localised soiling in an ASI network without introducing sophisticated ML algorithms. The advantage of the shown method is that it can give insights of the steady increasing of soiling inside the network. By introducing thresholds for the maximum soiling value, an automatic soiling alert can be implemented, which can help to realise a demand-oriented planning of maintenance tours for the network. The calculated value of the soiling state could also be used for the QC of historical data. The published Eye2Sky dataset of Schmidt et al. [29] can be improved by delivering cleaning state informations and the soiling metric. However, the method always needs a clean reference ASI and is therefore primarily useful in large ASI networks with irregular maintenance intervals.

In this thesis, a method for the automatic detection of interfering objects has been presented, called BirdDB. This method uses integrated motion-detection sensors of the installed ASIs. It does not require any model training and can be directly implemented with existing cameras. For the real-time operation of an ASI network, the information of the exact time of interference could be used to discard possibly affected images before calculating the forecast results. This could improve the performance of the model. This data also allows further investigation of how often, when, and under which circumstances these interfering events occur. It can also serve as a quality flag for future image data publications. In addition, the coupling of the detection with the automatic cleaning system helps not only to detect, but also to prevent interference events. The real-time detection of interferences can also be used to shoo away disturbers by playing alarms on the integrated speakers of the installed ASIs. BirdDB does not give any information about the exact type of interference and does not work for historical data. The additional recorded images in between the regular time stamps can serve as a database for real-live examples of interfering objects. This database can be used in the future to train a new image detection algorithm or to fine-tune existing ones, which can also distinguish between the type of interference and could also be used for historical data. A publication of such a database could also be useful for the ASI community to develop QC methods.

This thesis has shown that image errors only have a limited impact on the forecast results of ASI networks. Due to the high redundancy within ASI networks, the results are resilient to image errors from single cameras. Consequently, for a newly built ASI network, it is recommended to include redundant cameras because more cameras can improve the stability of the forecasts. Further research is needed for the evaluation of the impact of image errors on two-ASI systems and for single ASI end-to-end ML models. The impact of image errors is high for all interims results before the merging processes of the network, like shown for cloud mask creation and CBH estimation of individual ASI pairs. Therefore, the influence of soiling or other interferences on systems with fewer ASIs is expected to be greater due to the missing redundancy. For a correct CBH estimation with a stereoscopic approach, operators should also integrate far-distant ASI pairs within the network topology, in order to have precise CBH results also for high cloud layers. Although moderate continuous soiling does not have a large impact on the forecast, it is recommended to implement automatic tools for soiling detection. These tools can be used for demand-oriented maintenance planning without introducing fixed maintenance events for cleaning. In this work, it has also been shown that interfering objects can have a large impact on single-camera results. Operators should take action to minimise these impacts by detecting interferences in real time and omitting the affected images for the forecasts runs. This could be achieved by adding additional sensors of the ASIs, or by implementing classification models into the image preprocessing. In addition, automatic measures for interference prevention should be taken.

References

[1] Niklas Blum, Paul Matteschk, Yann Fabel, Bijan Nouri, Roberto Román, Luis F. Zarzalejo, Juan Carlos Antuña-Sánchez and Stefan Wilbert. 'Geometric calibration of all-sky cameras using sun and moon positions: A comprehensive analysis'. In: *Solar Energy* 295 (July 2025), p. 113476. ISSN: 0038092X. DOI: 10.1016/j.solener.2025.113476. URL: https://linkinghub.elsevier.com/retrieve/pii/S0038092X25002397 (visited on 28/07/2025).

[2] Niklas Benedikt Blum. 'Nowcasting of solar irradiance and photovoltaic production using a network of all-sky imagers'. PhD thesis. Aachen: Rheinisch-Westfälischen Technischen Hochschule Aachen, 12th Dec. 2022. URL: https://doi.org/10.18154/RWTH-2023-04771 (visited on 27/08/2024).

[3] G. Bradski. 'The OpenCV Library'. In: *Dr. Dobb's Journal of Software Tools* (2000). URL: https://opencv.org/.

[4] Bundesregierung. *Klimaschutzbericht 2024*. Unterrichtung durch die Bundesregierung Drucksache 20/12760. Berlin, 30th Aug. 2024. URL: https://dserver.bundestag.de/btd/20/127/2012760.pdf.

[5] German Bundestag. *Bundes-Klimaschutzgesetz (KSG)*. 2019. URL: https://www.gesetze-im-internet.de/ksg/index.html (visited on 08/06/2025).

[6] CDU, CSU and SPD. *Verantwortung für Deutschland - Koalitionsvertrag zwischen CDU, CSU und SPD*. München: CSU-Landesleitung, May 2025. URL: https://www.csu.de/common/csu/Koalitionsvertrag_2025_Verantwortung_fuer_Deutschland.pdf.

[7] Stephen A Cohn. 'A New Edition of the International Cloud Atlas'. In: 66 (2017).

[8] European Commission. *Communication from the Commission to the European Parliament, the European Council, the Council, the European Economic and Social Committee and the Committee Of The Regions - The European Green Deal*. 2019. URL: https://eur-lex.europa.eu/legal-content/EN/TXT/?uri=COM%3A2019%3A640%3AFIN (visited on 08/06/2025).

[9] D Dumortier. *Modelling global and diffuse horizontal ir- radiances under cloudless skies with different turbidities. Day- light II, JOU2-CT92-0144, Final Report Vol. 2*. 1995.

[10] DWD. *ICON-D2 - DWD-Geoportal*. dwd-geoporta.de. 2025. URL: https://dwd-geoportal.de/products/G_E6D/ (visited on 21/07/2025).

[11] eoPortal. *MTG (Meteosat Third Generation) - eoPortal*. 2025. URL: https://www.eoportal.org/satellite-missions/meteosat-third-generation (visited on 21/07/2025).

[12] Yann Fabel. *Cloud Segmentation and Classification from All-Sky Images Using Deep Learning*. Master thesis. Munich: Technical University of Munich, 14th July 2020. URL: https://elib.dlr.de/136767/.

[13] Yann Fabel, Niklas Blum, Bijan Nouri, Sergio Gonualez Rodriguez, Stefan Wilbert, Thomas Schmidt, Ole Johannsen, Luis F. Zarzalejo, Julia Kowalski and Robert Pitz-Paal. 'Beyond Observation: A Comprehensive Study of the All-Sky Image and Solar Irradiance Dataset SolarVision Almería'. 15th June 2025. (Visited on 21/07/2025).

[14] Yann Fabel, Bijan Nouri, Stefan Wilbert, Niklas Blum, Rudolph Triebel, Marcel Hasenbalg, Pascal Kuhn, Luis F. Zarzalejo and Robert Pitz-Paal. 'Applying self-supervised learning for semantic cloud segmentation of all-sky images'. In: *Atmospheric Measurement Techniques* 15.3 (14th Feb. 2022), pp. 797–809. ISSN: 1867-8548. DOI: 10.5194/amt-15-797-2022. URL: https://amt.copernicus.org/articles/15/797/2022/ (visited on 09/12/2024).

[15] P. Kuhn, B. Nouri, S. Wilbert, N. Hanrieder, C. Prahl, L. Ramirez, L. Zarzalejo, T. Schmidt, T. Schmidt, Z. Yasser, D. Heinemann, P. Tzoumanikas, A. Kazantzidis, J. Kleissl, P. Blanc and R. Pitz-Paal. 'Determination of the optimal camera distance for cloud height measurements with two all-sky imagers'. In: *Solar Energy* 179 (Feb. 2019), pp. 74–88. ISSN: 0038092X. DOI: 10.1016/j.solener.2018.12.038. URL: https://linkinghub.elsevier.com/retrieve/pii/S0038092X18312131 (visited on 04/02/2025).

[16] G. López and F. J. Batlles. 'Estimate of the atmospheric turbidity from three broad-band solar radiation algorithms. A comparative study'. In: *Annales Geophysicae* 22.8 (7th Sept. 2004). Publisher: Copernicus GmbH, pp. 2657–2668. ISSN: 1432-0576. DOI: 10.5194/angeo-22-2657-2004. URL: https://angeo.copernicus.org/articles/22/2657/2004/ (visited on 13/07/2025).

[17] MOBOTIX. *Q25M-Kamerahandbuch*. 60.195_DE_V4_03/2015. DE, Mar. 2015. URL: https://www.mobotix.com/sites/default/files/2017-10/Mx_ML_Q25M_de_20150325_0.pdf.

[18] United Nations. *Conference of the Parties*. FCCC/CP/2015/L.9/Rev.1. Paris: United Nations, 2015. URL: https://unfccc.int/resource/docs/2015/cop21/eng/l09r01.pdf.

[19] B. Nouri, P. Kuhn, S. Wilbert, N. Hanrieder, C. Prahl, L. Zarzalejo, A. Kazantzidis, P. Blanc and R. Pitz-Paal. 'Cloud height and tracking accuracy of three all sky imager systems for individual clouds'. In: *Solar Energy* 177 (Jan. 2019), pp. 213–228. ISSN: 0038092X. DOI: 10.1016/j.solener.2018.10.079. URL: https://linkinghub.elsevier.com/retrieve/pii/S0038092X18310570 (visited on 04/02/2025).

[20] B. Nouri, S. Wilbert, L. Segura, P. Kuhn, N. Hanrieder, A. Kazantzidis, T. Schmidt, L. Zarzalejo, P. Blanc and R. Pitz-Paal. 'Determination of cloud transmittance for all sky imager based solar nowcasting'. In: *Solar Energy* 181 (Mar. 2019), pp. 251–263. ISSN: 0038092X. DOI: 10.1016/j.solener.2019.02.004. URL: https://linkinghub.elsevier.com/retrieve/pii/S0038092X19301306 (visited on 09/12/2024).

[21] Bijan Nouri, Pascal Kuhn, Stefan Wilbert, Christoph Prahl, Robert Pitz-Paal, Philippe Blanc, Thomas Schmidt, Zeyad Yasser, Lourdes Ramirez Santigosa and Detlev Heineman. 'Nowcasting of DNI maps for the solar field based on voxel carving and individual 3D cloud objects from all sky images'. In: SolarPACES 2017: International Conference on Concentrating Solar Power and Chemical Energy Systems. Santiago, Chile, 2018, p. 190011. DOI: 10.1063/1.5067196. URL: https://pubs.aip.org/aip/acp/article/1023716 (visited on 28/07/2025).

[22] OpenCV. *OpenCV: Color conversions*. 26th Aug. 2024. URL: https://docs.opencv.org/3.4/de/d25/imgproc_color_conversions.html#color_convert_rgb_gray (visited on 27/08/2024).

[23] Helen C. Power and Apurva Goyal. 'Comparison of aerosol and climate variability over Germany and South Africa'. In: *International Journal of Climatology* 23.8 (30th June 2003). Publisher: Wiley, pp. 921–941. ISSN: 0899-8418, 1097-0088. DOI: 10.1002/joc.918. URL: https://rmets.onlinelibrary.wiley.com/doi/10.1002/joc.918 (visited on 13/07/2025).

[24] Olaf Ronneberger, Philipp Fischer and Thomas Brox. 'U-Net: Convolutional Networks for Biomedical Image Segmentation'. In: *Medical Image Computing and Computer-Assisted Intervention – MICCAI 2015*. Ed. by Nassir Navab, Joachim Hornegger, William M. Wells and Alejandro F. Frangi. Vol. 9351. Series Title: Lecture Notes in Computer Science. Cham: Springer International Publishing, 2015, pp. 234–241. ISBN: 978-3-319-24574-4. DOI: 10.1007/978-3-319-24574-4_28. URL: http://link.springer.com/10.1007/978-3-319-24574-4_28 (visited on 12/12/2024).

[25] André Scheper. *On the design of Eye2Sky camera network subsets for the optimal nowcast of PV production*. Master thesis. Oldenburg: Carl von Ossietzky Universität Oldenburg, 2024. URL: https://elib.dlr.de/211689/.

[26] Franziska Schmid, Yong Wang and Abdoulaye Harou. *Nowcasting Guidelines – A Summary*. World Meteorological Organization. 27th Nov. 2019. URL: https://wmo.int/media/magazine-article/nowcasting-guidelines-summary (visited on 17/05/2025).

[27] T. Schmidt, J. Stührenberg, N. Blum, J. Lezaca, A. Hammer and T. Vogt. 'A network of all sky imagers (ASI) enabling accurate and high-resolution very short-term forecasts of solar irradiance'. In: *21st Wind & Solar Integration Workshop (WIW 2022)*. 21st Wind & Solar Integration Workshop (WIW 2022). Hybrid Conference, The Hague, Netherlands: Institution of Engineering and Technology, 2022, pp. 372–378. ISBN: 978-1-83953-833-9. DOI: 10.1049/icp.2022.2778. URL: https://digital-library.theiet.org/content/conferences/10.1049/icp.2022.2778 (visited on 27/08/2024).

[28] Thomas Schmidt, Jonas Stührenberg, Niklas Blum, Jorge Lezaca, Annette Hammer, Stefan Wilbert, Bijan Nouri, Marion Schroedter-Homscheidt, Detlev Heinemann and Thomas Vogt. 'Eye2Sky – a network of all-sky imager and meteorological measurement stations for high resolution nowcasting of solar irradiance'. In: *Meteorologische Zeitschrift* (18th June 2025), p. 106743. ISSN: 0941-2948. DOI: 10.1127/metz/2025/1245. URL: https://www.schweizerbart.de/papers/metz/detail/prepub/106743/Eye2Sky__a_network_of_all_sky_imager_and_meteorolo?af=crossref (visited on 24/06/2025).

[29] Thomas Schmidt, Jonas Stührenberg, Niklas Blum, Jorge Lezaca, Annette Hammer, Stefan Wilbert, Bijan Nouri, Marion Schroedter-Homscheidt, Detlev Heinemann and Thomas Vogt. *Eye2Sky dataset - All-sky images and meteorological measurements*. Version 1.0. 24th July 2024. DOI: 10.5281/ZENODO.12804613. URL: https://zenodo.org/doi/10.5281/zenodo.12804613 (visited on 03/02/2025).

[30] Thomas Schmidt, Jonas Stührenberg, Niklas Blum, Jorge Enrique Lezaca Galeano, Annette Hammer, Marion Schroedter-Homscheidt and Thomas Vogt. 'Comparison of short-term (hour-ahead) solar irradiance forecasts from all-sky imagers and satellite images'. International Conference of Energy Meteorology ICEM. Padua, Italy, June 2023. URL: https://elib.dlr.de/197562/.

[31] Harald Schwarz and Xiaoshu Cai. 'Integration of renewable energies, flexible loads and storages into the German power grid: Actual situation in German change of power system'. In: *Frontiers in Energy* 11.2 (June 2017). Publisher: Springer Science and Business Media LLC, pp. 107–118. ISSN: 2095-1701, 2095-1698. DOI: 10.1007/s11708-017-0470-x. URL: http://link.springer.com/10.1007/s11708-017-0470-x (visited on 08/07/2025).

[32] Manajit Sengupta, Aron Habte, Stefan Wilbert, Christian Gueymard, Jan Remund, Elke Lorenz, Wilfried Van Sark and Adam Jensen. *Best Practices Handbook for the Collection and Use of Solar Resource Data for Solar Energy Applications: Fourth Edition*. NREL/TP–5D00-88300, 2448063, MainId:89075. 26th Sept. 2024, NREL/TP–5D00–88300, 2448063, MainId:89075. DOI: 10.2172/2448063. URL: https://www.osti.gov/servlets/purl/2448063/ (visited on 04/03/2025).

[33] Unidata. *Unidata | NetCDF*. 2025. URL: https://www.unidata.ucar.edu/software/netcdf/ (visited on 26/07/2025).

[34] Sandra Wassermann, Matthias Reeg and Kristina Nienhaus. 'Current challenges of Germany's energy transition project and competing strategies of challengers and incumbents: The case of direct marketing of electricity from renewable energy sources'. In: *Energy Policy* 76 (Jan. 2015). Publisher: Elsevier BV, pp. 66–75. ISSN: 0301-4215. DOI: 10.1016/j.enpol.2014.10.013. URL: https://linkinghub.elsevier.com/retrieve/pii/S0301421514005576 (visited on 08/07/2025).

A Appendix

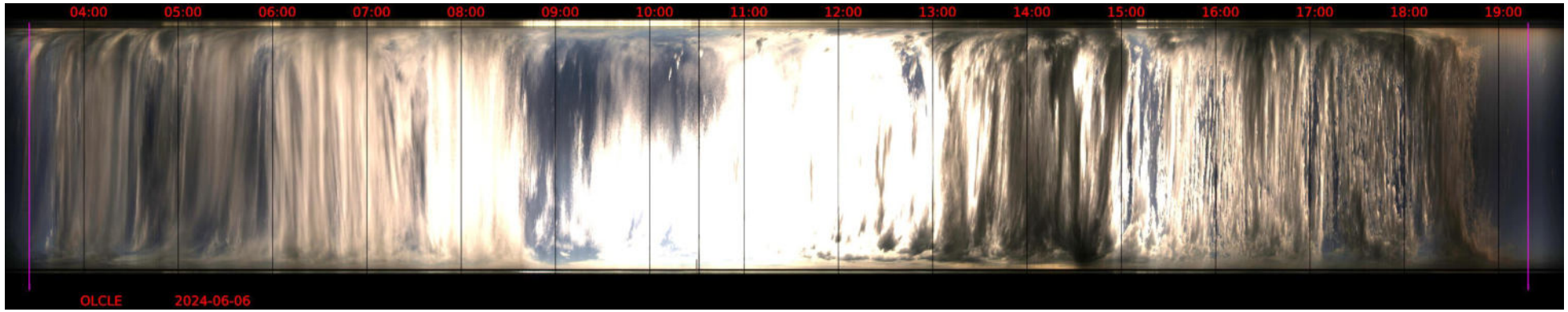

(a) Keogram of station OLCLE for the 6th of June 2024.

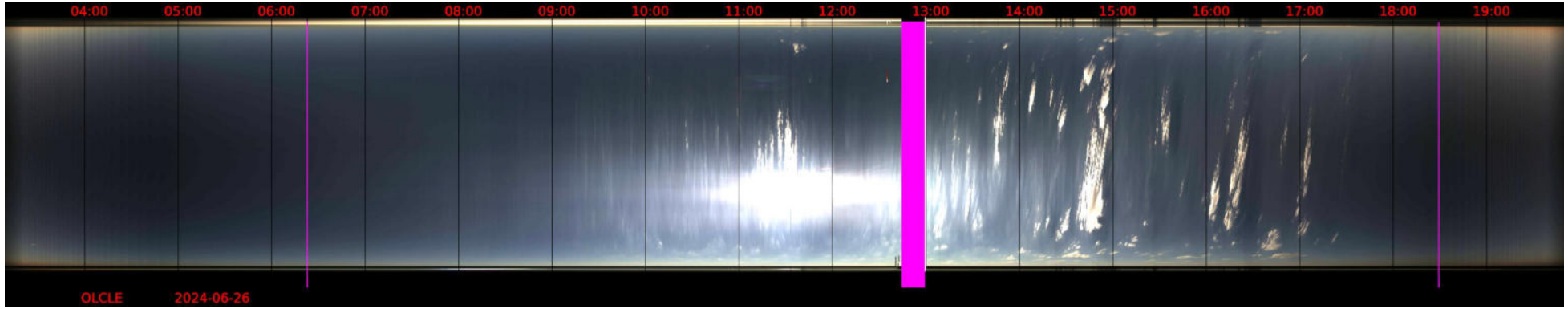

(b) Keogram of station OLCLE for the 26th of June 2024.

Figure 44: Keograms of station OLCLE for the 6th and the 26th of June 2024.

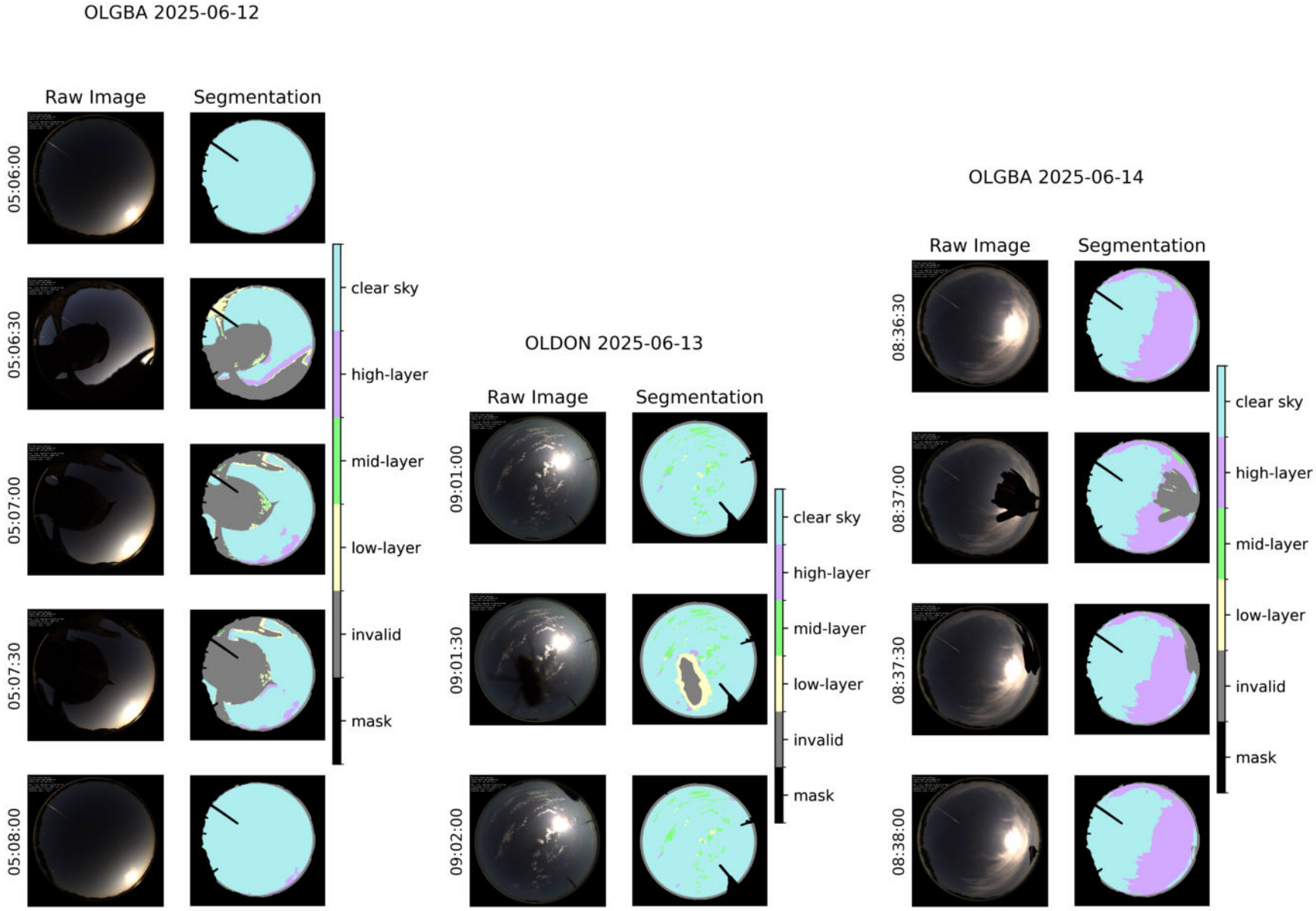

(a) bird **(b)** arthropod **(c)** bird

Figure 45: Examples for interfering objects in June 2025 and semantic segmentation results.

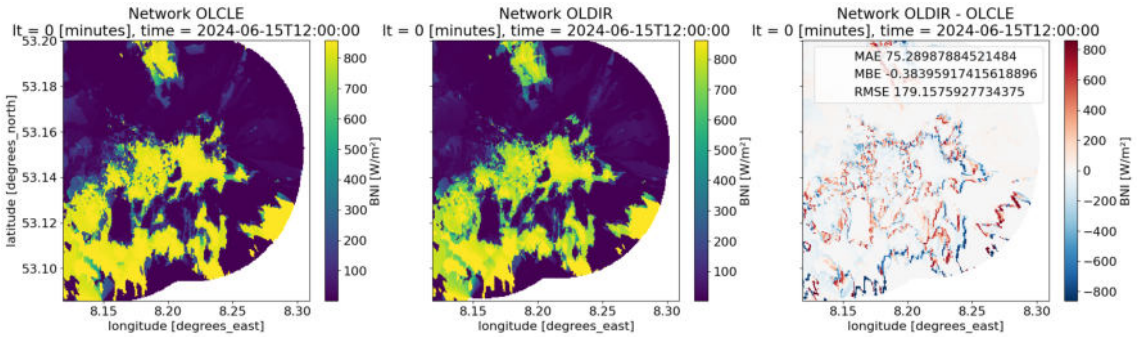

(a) Lead time 0 min

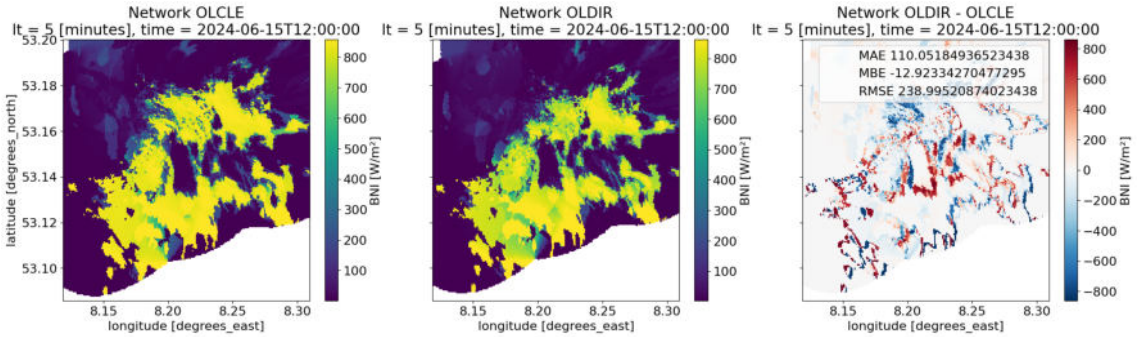

(b) Lead time 5 min

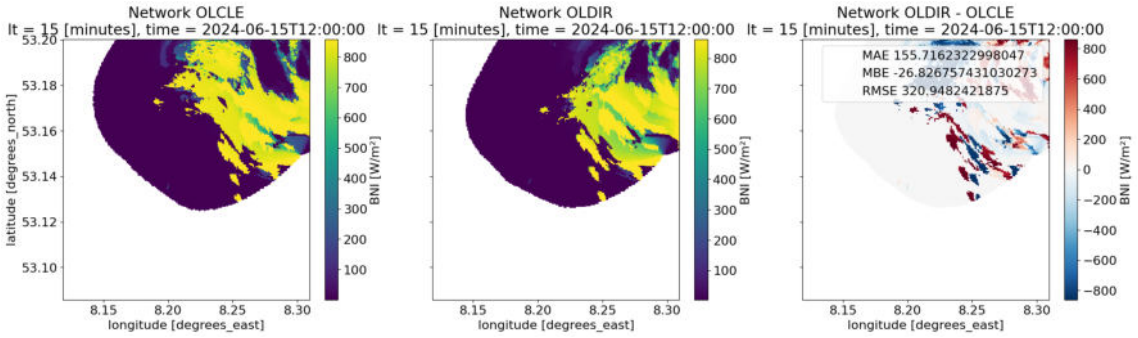

(c) Lead time 15 min

Figure 46: Beam (direct) normal irradiance (BNI) results of full subnet configurations with reference camera OLCLE, camera OLDIR, and difference maps of both results for lead times lt = 0 min (a), 5 min (b) and 15 min (c), calculated spatial mean absolute error (MAE), mean bias error (MBE) and root mean square error (RMSE), 15 June 2024.

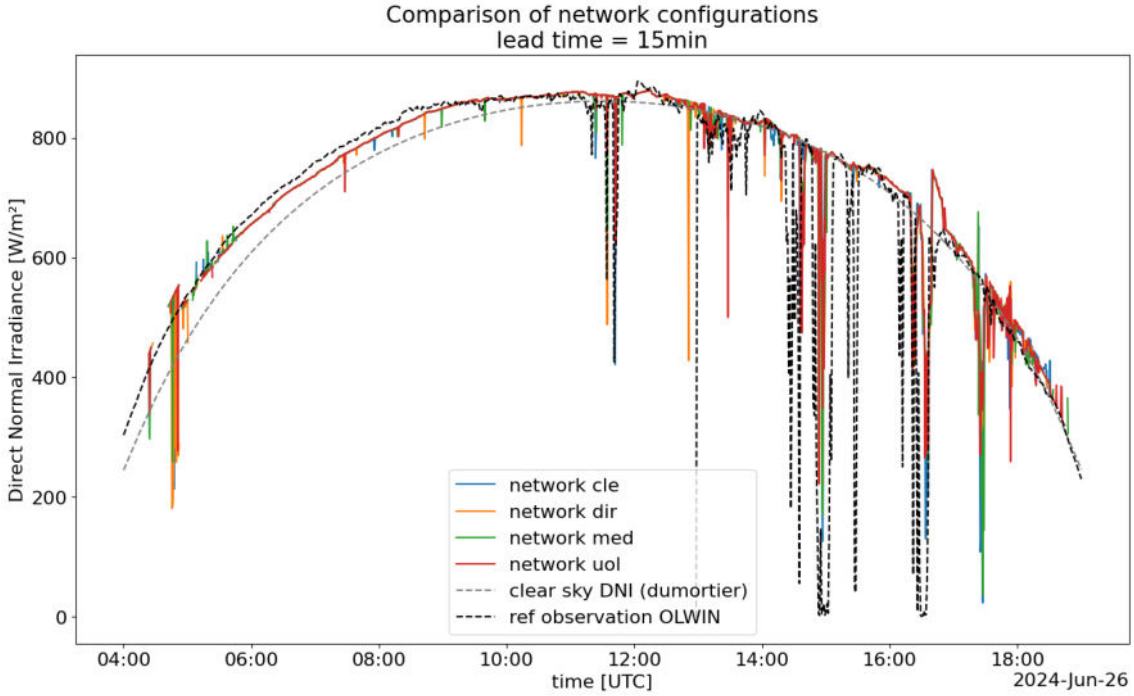

(a) Beam (direct) normal irradiance (BNI) results of WobaS for different network configuration

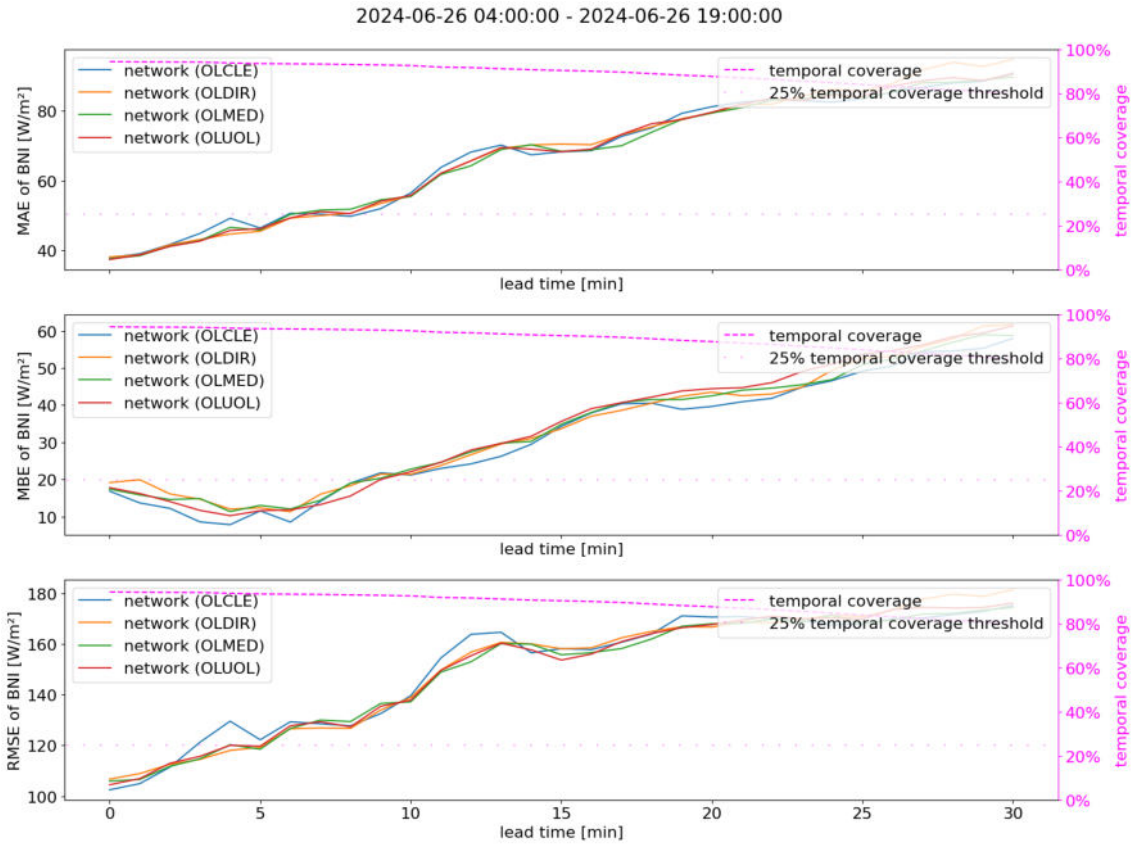

(b) Temporal mean absolute error (MAE), mean bias error (MBE) and root mean square error (RMSE)

Figure 47: Beam (direct) normal irradiance (BNI) results and error metrics for location of station OLWIN, 26 June 2024.

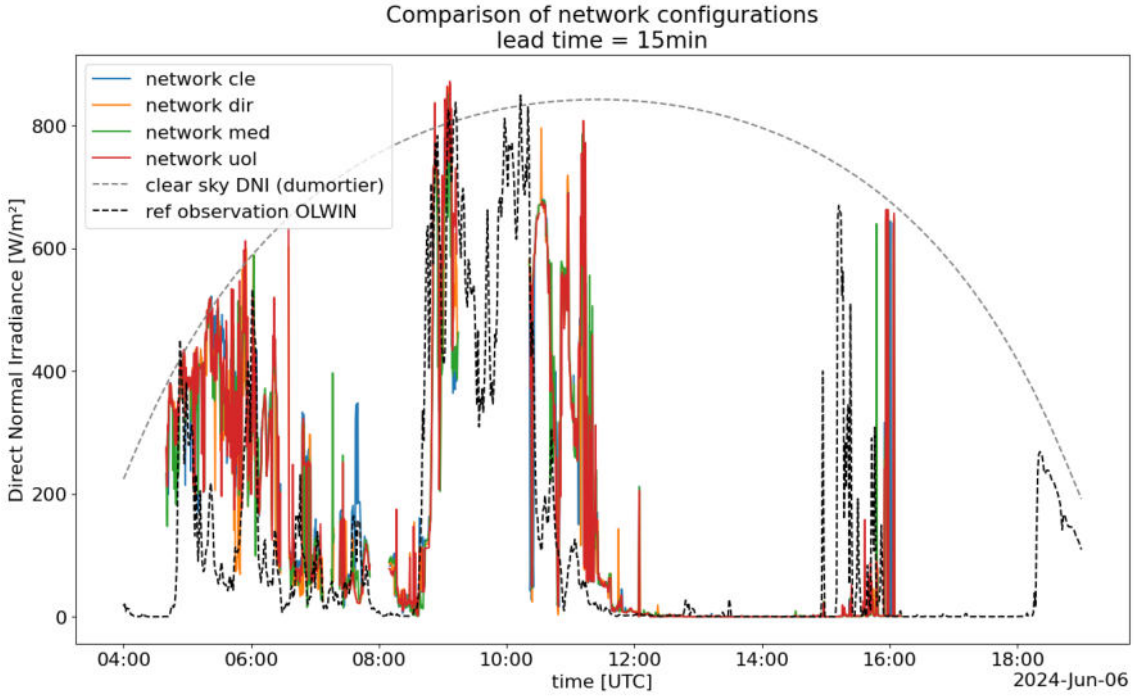

(a) Beam (direct) normal irradiance (BNI) results of WobaS for different network configuration

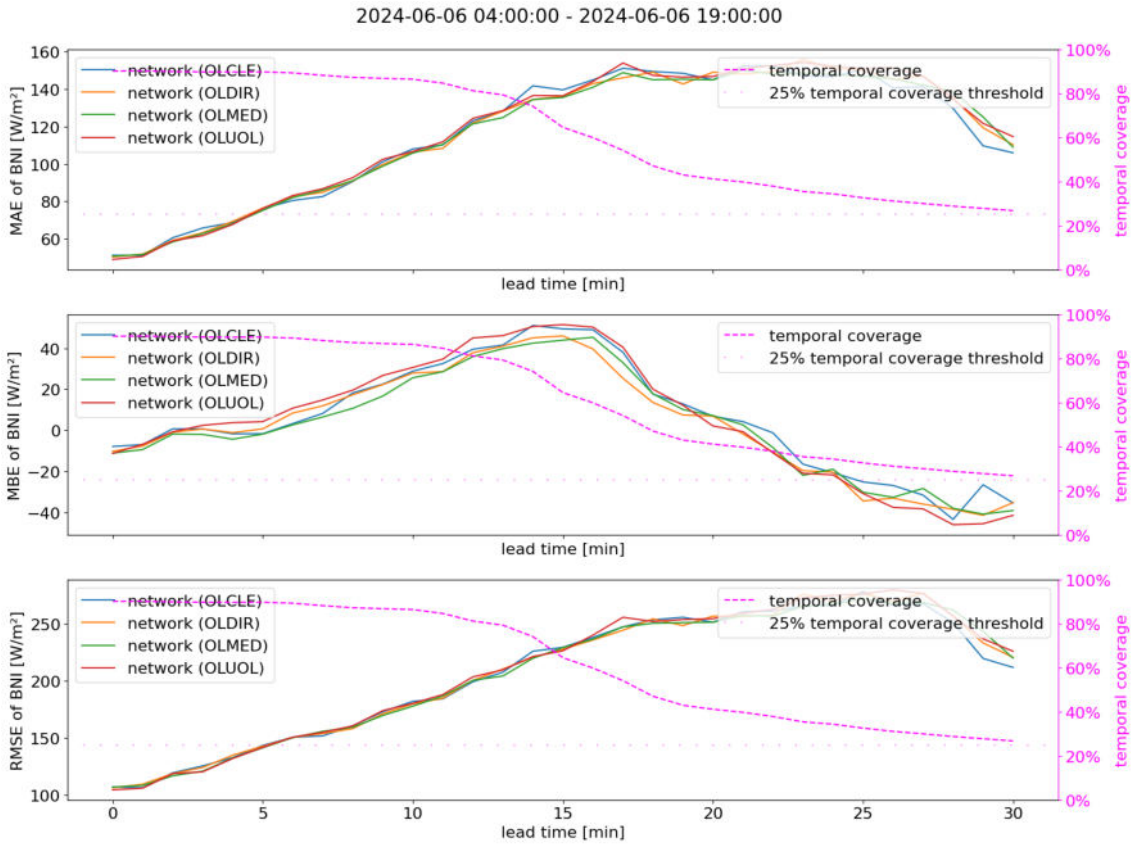

(b) Temporal mean absolute error (MAE), mean bias error (MBE) and root mean square error (RMSE)

Figure 48: Beam (direct) normal irradiance (BNI) results and error metrics for location of station OLWIN, 6 June 2024.

Date Start	Time Start	Date End	Time End	Station	Tag	Report
06.06.2024	12:23	06.06.2024	12:33	OLWIN,OLUOL,OLQ71,OLCLE	cleaning	
13.06.2024	15:13	13.06.2024	15:23	OLWIN,OLUOL,OLQ71,OLCLE	cleaning	
19.06.2024	13:45	19.06.2024	14:05	PVAMM	cleaning,maintenance	cleaning of camera and three Sensors. A lot of lichen on USA, lock of ladder to be exchanged
20.06.2024	08:40	20.06.2024	08:50	OLFLE	cleaning,Horizon	Check if anemometer in the back cannot be shortened by 15cm
20.06.2024	09:38	20.06.2024	09:48	OLDON	cleaning	
20.06.2024	11:44	20.06.2024	11:54	OLWIN,OLUOL,OLQ71,OLCLE	cleaning	
26.06.2024	13:50	26.06.2024	14:00	CDLRA	problem with network cable	
26.06.2024	15:18	26.06.2024	15:28	OLWIN,OLUOL,OLQ71,OLCLE	cleaning	short power outage of all stations
...						
05.05.2025	16:15	05.05.2025	17:15	OLCLE,OLQ71,OLUOL,OLWIN	cleaning	visit with students lasting 1 hour, disturbances possible
09.05.2025	11:54	09.05.2025	12:04	OLDON	recalibration,cleaning	exchanged with new PU MS.17.001.0013, pyr1 90730, pyr2 90731, pyr3 PY106498 pyra4: Q108073. wrote new datalogger program, took out normpressure bug, cleaning, cleaned th sensor, new fence around rooftop
09.05.2025	11:58	09.05.2025	12:08	OLDON	recalibration,photos	
12.05.2025	12:30	12.05.2025	13:00	OLGBA	cleaning	
12.05.2025	18:10	12.05.2025	17:55	OLCLE,OLQ71,OLUOL,OLWIN	cleaning	
22.05.2025	12:45	22.05.2025	12:55	OLCLE,OLQ71,OLUOL,OLWIN	cleaning	
28.05.2025	14:00	28.05.2025	14:10	OLCLE,OLQ71,OLUOL,OLWIN	cleaning	

Figure 49: Excerpts from Eye2Sky logbook for June 2024 and May 2025 for stations in subnetwork configuration of the study setup (local time).

Affidavit

I hereby certify that I have written this thesis myself and that I have not used any sources other than those specified and have not made use of any unauthorised external help. Furthermore, the work was not produced using unrecognisable generative AI. Furthermore, I assure that I have followed the general principles of scientific / academic work and publication as laid down in the guidelines of good academic practice of the University of Oldenburg. I further declare that the work has not yet been submitted in the same or a similar form to any examining authority.

Oldenburg (Oldb), 4th August 2025 .....